Regional Hotspots of Change in Northern High Latitudes Informed by Observations from Space

Jennifer Watts[1]

[1]Affiliation not available

January 11, 2024

Authors: Jennifer D. Watts[1]; Stefano Potter[1]; Brendan M. Rogers[1], Anna-Maria Virkkala[1], Greg Fiske[1], Kyle A. Arndt[1], Arden Burrell[1], Kevin Butler[2], Bob Gerlt[2], John Grayson[2], Tatiana A. Shestakova[3,4], Jinyang Du[5], Youngwook Kim[6], Frans-Jan Parmentier[7], Susan M. Natali[1]

[1] Woodwell Climate Research Center, 149 Woods Hole Road, Falmouth, MA, 02540.

[2] Environmental Systems Research Institute (Esri). 380 New York Street, Redlands, CA, 92373.

[3] Department of Agricultural and Forest Science and Engineering, University of Lleida, Av. Alcalde Rovira Roure, 191, Lleida, Spain, 25198.

[4] Joint Research Unit CTFC–AGROTECNIO–CERCA, Av. Alcalde Rovira Roure, 191, Lleida, Spain, 25198.

[5] Numerical Terradynamic Simulation Group (NTSG), ISB 415, 32 Campus Drive, Missoula, MT, 59812.

[6] Department of Biology, United Arab Emirates University, Al Ain, Abu Dhabi, UAE, 15551.

[7] Center for Biogeochemistry of the Anthropocene, Department of Geosciences, University of Oslo, N-0315, Oslo, Norway.

Abstract

The high latitudes cover ~ 20% of Earth's land surface. This region is facing many changes in thermal, moisture and vegetation properties, driven by climate warming. Here we leverage remote sensing-informed and climate reanalysis records to improve understanding of changes in key ecosystem indicators. To do so we applied non-parametric trend detections and Getis-Ord Gi* spatial hotspot assessments. We found substantial terrestrial warming trends across Siberia, portions of Greenland, Alaska, and western Canada. The same regions also showed increases in vapor pressure deficit, however changes in precipitation and soil moisture were variable. Vegetation greening and browning were widespread across both continents. Browning of the boreal zone was especially evident in autumn. Multivariate hotspot assessments indicated that Siberian ecoregions experienced the most substantial changes in thermal, moisture and vegetation status. Finally, we found that using regionally-based trends alone, without more local assessments, can yield incomplete views of high-latitude responses to climate warming.

Key Points

- This study identifies multiple changes in climatic and vegetation conditions across the high-latitude terrestrial domain.
- Environmental changes occurring across the high-latitude domain are spatially complex, leading to a need for localized (i.e., pixel-based) trend assessments in addition to those based on regional averages.

- Eurasia (especially Siberia), and portions of Alaska and Canada, were identified as primary hotspots of change based on multiple ecosystem indicators.

1 Introduction

Over the past two decades the high latitude (tundra and boreal) domain has been widely reported as the fastest warming land area on Earth (Wang et al., 2022; Rantanen et al., 2022). The observed ground temperature rise has resulted in longer surface non-frozen seasons and the loss of sub-surface permafrost (Kim et al., 2012; Biskaborn et al., 2019). The consequences of this warming for human communities, natural ecosystems, and global climate will likely be severe and widespread (Schuur & Mack, 2018; Overland et al., 2019; Miner et al., 2022). Indeed, permafrost degradation and ground collapse have already damaged towns, villages and other critical polar infrastructure (Hjort et al., 2022). Unfrozen conditions, along with changes in soil hydrology (Bring et al., 2016; Karesdotter et al., 2021; Webb et al., 2022), are also escalating the release of organic carbon from permafrost-region soils, further amplifying climate warming through the release of greenhouse gases (Schuur et al., 2015; Bruhwiler et al., 2021; Watts et al., 2021, 2023).

The changes occurring across high latitudes are complex and often show contrasting patterns over time and space. Although pan-Arctic increases in air temperature are widely documented (Rantanen et al., 2022), localized and regional cooling can also occur as has been observed over eastern Canada in the past two decades (Qian et al., 2011; Xie et al., 2021). In addition to climate warming, changes in precipitation have been reported. For example, a synthesis of climate model outputs shows projected trends of increasing arctic precipitation but decreasing winter snow cover due to warming over the twenty-first century (Bintanja & Andry 2017). However, there may be local exceptions (e.g., Wang et al., 2020). Moreover, models also estimate a drying of near-surface soils, driven by the infiltration of moisture into deeper soils as ground thaws (Andresen et al., 2020). Changes in vegetation are also complex. Some field and remote sensing studies report high-latitude greening, thought to be driven by lessening cold temperature constraints and the growth of shrubs (Berner et al., 2020; Myers-Smith et al., 2020; Chen et al., 2021; Liu et al., 2021), CO_2 fertilization and increased nutrient availability from thawing soils (Hicks Pries et al., 2022). In some cases, greening may simply indicate vegetation regrowth following disturbance (e.g., wildfire) (Wang & Friedl 2019). On the other hand, recent fire and other disturbances such as increases in temperature extremes, drought and insect outbreaks may contribute to reported observations of vegetation browning (Beck & Goetz 2011; Phoenix & Bjerke 2016; Wang & Friedl 2019; Foster et al., 2022).

Although past field studies have been instrumental in identifying the complex changes taking place across the high latitudes, many focus only on individual indicators assessed over limited temporal and spatial scales. In contrast, regional change assessments using suites of continuous longer-term geospatial records (e.g., see Duncan et al., 2020) can provide more complete insights into the state of the Earth system. Here we investigate local and regional patterns of change in thermal, moisture, and vegetation taking place within high latitude terrestrial regions, as observed in multiple records from satellites and satellite-informed reanalysis. We build (and expand) upon past assessments including the NOAA "Arctic Report Cards" (Druckenmiller et al., 2022; Thoman et al., 2023) and the IPCC Special Report on the Ocean and Cryosphere in a Changing Climate (Meredith et al., 2019) which summarize general pan-Arctic trends (e.g., air temperature, snow cover, tundra greenness) rather than local patterns. We also build upon the work of Box et al. (2019) which examined high-latitude trends in temperature, and summarized other indicators reported in the literature.

2 Methods

We included 12 data products to gain information about thermal, moisture, and vegetation states (*Supplement* (SI) Table 1). To assess change, we included non-parametric trend analyses (Mann-Kendall and Thiel-Sen) at local (pixel) and regional scales, and also a Getis-Ord Gi* spatial autocorrelation approach (i.e., hotspot analysis) to further confirm change.

The methods are summarized below. Additional information is provided in the SI.

2.1 Study Domain

Our domain spans tundra and boreal lands > 45°N, excluding those classified as ice, agriculture, and lakes. Approximately 73% of the domain (2.85 x 10^7 km^2) is underlain by permafrost, which includes continuous (most intact), discontinuous and sporadic/isolated zones (Brown et al., 2002; SI Figure 1-a). A separate assessment of change specifically for permafrost terrains is provided in the SI. Colder northern and mountainous areas are dominated by treeless tundra vegetation (30% of the region). Non-tundra lands (i.e., boreal) are mainly covered by forests, wetlands, and open shrublands (SI Figure 1-b). Study sub-regions examined in the change assessments include: North America and Eurasia; tundra and boreal; Eurasia-tundra (4.15 x 10^6km^2), Eurasia-boreal (13.2 x 10^6km^2); North America-tundra (4.7 x 10^6 km^2), North America-boreal (6.4 x 10^6 km^2). In addition to pixel-level and sub-regional assessments, we also examined changes at the ecoregion level (Dinerstein et al., 2017; SI Figure 1-c).

2.2 Geospatial Records

We focused on indicators of three key ecosystem states: thermal, moisture and vegetation. Thermal included near-surface annual (and seasonal) average air temperature (AT; °C; Muñoz-Sabater et al., 2021), permafrost maximum active layer thickness (ALT, m; Obu et al., 2021) and length of surface non-frozen season (NFS, days; Kim et al., 2021). Moisture included average precipitation (PPT, m), total snow cover (SC, km^2), average vapor pressure deficit (VPD, kPa), average near-surface soil moisture during the non-frozen season (SM, cm^3 cm^{-3}) (Muñoz-Sabater et al., 2021), and average surface water fraction (FW, %; Du & Kimball, 2021). Vegetation included averages of normalized difference vegetation index (NDVI, unitless; Guay et al., 2015) and vegetation optical depth (VOD, unitless; Moesinger et al., 2020) during the non-frozen season, and annual tree and non-tree cover fractions (TC, NTC, %; Hansen & Song, 2018).

We examined indicator trends on an annual and seasonal (spring, summer, autumn, winter) basis, except for ALT which represents an annual maximum. For NDVI and SM, an additional screening was applied to remove observations occurring outside of the annual surface NFS (*SI 2.1*). For this analysis we assessed the average state of NDVI, instead of annual summer maximum, to obtain a better sense of vegetation greening over seasonal periods. Detailed descriptions of the seasonal trend results can be found in *SI Section 3* .

See *SI Sections 1.1, 2.1, 2.2* for information about the data records and preprocessing. When possible (i.e., AT, PPT, VPD, SM) we extended the trend assessments over multiple longer-term records, from 1959–2020 (62 years) and 1980–2020 (40 years). For NDVI, VOD, TC, NTC the timeframe was 1988–2020 (33 years). For all indicators we also included a more recent time period, 1997–2020 (24 years).

Because land disturbance resulting from wildfires is common throughout the domain, we included a brief assessment of correspondence between burned areas from GFED4s (van der Werf et al., 2017; Randerson et al., 2018) and pixels that we identified as having significant trend in indicators. These results are detailed in the SI (*Section 5.2*).

2.3 Trend and Change Spot Assessments

For each indicator and identified time frame, we examined slope and trend significance for the time series according to regionally-based averages (*SI Section 1.2*), and on a per-pixel basis. We applied a non-parametric Mann-Kendall test that detects monotonic upward or downward trends (Yue et al., 2002; Watts et al., 2014). The ZYP package in R, Version 0.10-1.1 (Bronaugh & Werner, 2013) provided z-scores and p-values. Theil-Sen (median-based) estimators of slope were applied to each time series having a trend significance of $p < 0.05$. However, because of the nature of this approach, it may not detect spatial clusters of emergent change. To address this, we also applied a Getis-Ord Gi* change assessment using the Emerging Hotspot Analysis (EHA) algorithm in Esri ArcGIS Pro V.2.9 (Mitchell, 2005). The algorithm identifies statistically significant spatial clusters of high values and low values based on spatial autocorrelation. This method has been informative for other ecological applications, including assessments of landscape fragmentation for conservation management (Kowe et al., 2019) and identifying the vulnerability of urban populations to climate change (Ge et al., 2017). As a final step, we ranked identified clusters of change by applying a multivariate "change score" assessment, which summed individual hotspot scores (see *SI Section 2* and *SI Table 2*).

3 Results and Discussion

Here we focus on the full terrestrial domain. A separate summary of indicator trends and hotspots for the permafrost region is provided in the *SI* (*Section 5.1*).

3.1 Thiel-Sen Trend results

3.1.1 Thermal

Using the methods of Rantanen et al. (2022), we found that AT in the full terrestrial region warmed at a rate 70% higher than the global average, from 2011–2020 compared to a 1980–2010 baseline (anomalies of 1.12°C vs 0.66°C). Warming rates ranged from 0.38 (1959–2020) to 0.61 °C dec^{-1} (1997–2020) (Figure 1; *SI Table 3*), with 86% of Eurasian ecosystems impacted by significant annual warming during the 1997–2020 period (Figures 2 and 3) relative to only 10% in North America. The annual trends were especially influenced by substantial warming in winter, spring and autumn (see *SI Section 4; SI Figures 10–13*). The most severe annual regional warming (1997–2020) occurred over the Eurasia tundra (reaching 1.1 °C dec^{-1}) and boreal (˜0.6 °C dec^{-1}; *SI Figure 4*). Especially high local rates of warming (˜1.7 °C dec^{-1} during 1997–2020) were found over the Taymyr and boreal central Siberia. In North America, annual warming in tundra exceeded the boreal (0.49 vs. 0.26 °C dec^{-1}) from 1980–2020, however from 1997–2020 the trends were mitigated by periods of cooling (though in many places the cooling was not significant (*SI Table 3* , *SI Figures 4;* also observed elsewhere in soil temperature records; Qian et al., 2011) except for the Alaska North Slope and Canadian Mackenzie Delta where warming trends remained over both periods.

The annual NFS increased across the full domain by 2.3 days dec^{-1} (1997–2020), exceeding rates previously reported (Kim et al., 2012). Overall, ˜12% of Eurasia and 7% of North America pixels experienced a significant increase in annual NFS from 1997–2020, primarily within the tundra regions (˜4 days dec^{-1}). When examined seasonally, NFS increase was larger in autumn relative to spring (*SI 4.1.2*). In permafrost-affected areas (*SI Figure 1*) ALT increased over 61% of Eurasia, compared to 33% of North America (Figure 3), averaging 0.09 m dec^{-1}, especially within western North America and eastern Russia (local pixel-based rates up to 0.5 m dec^{-1}). Our reported ALT change rates (from the Obu et al., 2021 dataset) are less than the average pan-Arctic rate of 0.8 m dec^{-1} (2000–2018) observed at Circumpolar Active Layer Monitoring (CALM) field sites (Strand et al., 2021;*SI Section 1.1*); however, there is agreement in the direction of trend between the geospatial product and field observations.

3.1.2 Moisture

The regional trend analysis indicated a significant increase in annual PPT over the entire domain (Figure 1; *SI Table 3*), 0.33 m dec^{-1} over the period 1997–2020. However, per-pixel trends revealed the changes to be predominately local (e.g., only 7% of Eurasia and 8% North America showed significant positive trends) (Figure 2; *SI Figure 5*). These areas included eastern Siberia, southern Alaska and British Columbia, the Mackenzie Delta, and Quebec. Decreasing PPT trends at a local scale occurred within 2% of the Eurasian domain (boreal central Siberia). Local trends in seasonal PPT were observed primarily during summer and autumn, yet the spatial extent remained minimal (*SI 4.2.1*). Per-pixel trends in winter snow cover were minimal (<1% of the full domain) from 1997–2020, although the regionally-based trend analysis showed declining snow cover within the Eurasian tundra and boreal, and over the North American boreal during the extended period of 1959–2020 (*SI Table 4*). For 1997–2020, we identified pixels having local zones of seasonal trends, especially in southern boreal Siberia where a decrease in spring and autumn snow cover occurred (*SI Figure 11, 13, 17, Tables 5 & 7*). For annual VPD, we found increasing regional trends (1997–2020) for Eurasia (boreal and tundra) and North American tundra (*SI 4.2.3*). Similarly, per-pixel results showed positive trend over 42% of Eurasia and 8% of North America, while decreasing VPD was minimal. The most prominent increases in VPD occurred over Siberia, northern Alaska, and southwest Canada. Recent (1997–2020) trends in non-frozen season SM were not significant at the regional level (*SI 4.2.4*). However, local areas of SM drying were observed over central Siberia, and local wetting occurred over the Mackenzie Delta. Decreasing (per-pixel) SM was detected over 6% of the Eurasian domain and 2% of North America (relative to increases of 2% and 3%; Figure 2). Local decreases in spring SM were observed in western

Canada and southern Siberia, and local areas of wetting included the Mackenzie Delta (*SI Figure 11*). The 1997–2020 summer and autumn decreases in SM were primarily within central Siberia (*SI Figures 12 & 13*); in autumn the Mackenzie stood out as an area of SM increase. Finally, we observed significant regional increases in FW (Figure 2; *SI Figure 5, Section 4.2.5*) indicating an increase in open water and/or flooded land surfaces. Overall, 36% of pixels in Eurasia and 26% in North America showed increase in FW, including within central Canada, the Yukon-Kuskokwim Delta, central Siberia including Yakutia (which has already suffered severe flood damage, resulting from climate change; see Fujiwara, 2017). The extent of FW change is larger than reported in an earlier 2003–2011 assessment (Watts et al., 2014) and likely reflects water released from thawing permafrost (Walvoord & Kurylyk, 2016) and local increases in seasonal precipitation (Feng et al., 2021).

3.1.3 Vegetation

The annual non-frozen season NDVI results at the regional level showed decreasing trends (browning) for the Eurasian boreal zone (both 1988–2020 and 1997–2020; Figure 1; *SI Table 3*). Similarly, the seasonally-based regional results also showed declining NDVI during the autumn, over 1988–2020 and 1997–2020 periods (*SI Table 7*). However, as with the other indicators, more insight was gained through examination of the per-pixel trends, which showed strong spatial and seasonal differences in NDVI patterns. In the spring, 23% and 18% of pixels in Eurasia and North America had increasing NDVI (1997–2020;*SI Figure 16*); compared to decreasing trends (4% Eurasia; 14% North America). In summer, 18-19% of pixels in both continents had increasing NDVI (*SI Figure 17*), though North America had more pixels with NDVI decrease (14%; 9% in Eurasia). In autumn (*SI Figure 18*) ˜54% of pixels in both continents showed decreasing NDVI (<3% showed NDVI increase). Many of the spring per-pixel trends (*SI Figure 11-n*) were scattered across the domain, though clusters of increase were in boreal British Columbia, the tundra of Nunavut and northern Quebec, southern Fennoscandia, western Russia, and the Taymyr. Pixels having decreasing spring NDVI were primarily across the southern Canadian boreal. Pixels having summer NDVI increase (*SI Figure 12-j*) included Interior Alaska and North Slope, northwest Canada, western Russia, Finland and Sweden. Clusters of summer NDVI decrease included the Yukon-Kuskokwim Delta, the Seward Peninsula, Eastern Canada, and Taymyr. In autumn (*SI Figure 13-n*) areas of NDVI decrease included much of the tundra and northern boreal across Russia, Norway, Canada, and southern Alaska.

Similar to our findings, a past assessment of NDVI from the AVHRR-based GIMMS record through 2006 using non-parametric trend tests (de Jong et al., 2011) reported considerable spatial variability in greening and browning trends within the high latitude domain. More recent studies (Berner et al., 2020; Berner & Goetz, 2022) reported that many pixels (around 30%) across the tundra (years 1985–2016) and northern boreal (1985–2019) domains had greening trends, based on observed summer NDVI maximum records detected using higher (30 m) resolution Landsat imagery (versus the 1 km GIMMS). Although there are key differences between our studies (i.e., differences in sensors, spatial resolutions, temporal representation, and methodology), we did find similarities in the regional patterns of summer greening and browning. Further, Berner & Goetz (2022) reported that greening trends in the boreal were only half as common relative to browning in the Landsat summer NDVI maximum record over the 2000–2019 period relative to 1985–2019, indicating a possible shift towards less greening at the high latitudes, as was observed in this study and elsewhere (e.g., see Liu et al., 2021). In many places, wildfire may be driving the observed trends. Our supplemental assessment of co-occurrence between fire and identified NDVI trends showed that 75% of pixels with greening (and 62% of pixels with browning) were associated with GFED4s pixels where fire disturbance had occurred (*SI 5.2*). However, we were unable to identify how many of the NDVI pixels were associated with disturbance, given large differences in spatial resolutions between the products. In addition to fire disturbance, insect outbreaks (Foster et al., 2022), summer drought (Peng et al., 2011; Zona et al., 2023) and/or increases in water inundation (i.e., FW) may be driving localized browning (e.g., Helbig et al., 2016; Magnusson et al., 2023).

Our study identified local areas of VOD increase over Alaska, northwest Canada, far eastern and western Eurasia (*SI Figure 6; SI 6.3*), especially during the spring period (*SI 4.3.2*) though significant annual trends were not detected on a per-region basis (*SI Table 3*). Unlike NDVI, which is an indicator of reflectance ratios between red and infrared bands (related to changes in foliar greenness or brownness as an indicator of foliar and plant health), the 0.25° resolution Ku-derived VOD (*SI Section 1.1*) provides a different metric of plant status and is directly sensitive to changes in foliar water content. Decreasing VOD trends may indicate long-term impacts of water stress and loss of leaves, or more severe, recent loss of biomass (e.g., following water stress or severe pulse disturbances such as fire or larger scale logging; Jones et al., 2013; Liu et al., 2022). Whereas positive VOD trends can indicate multi-year increases in vegetation growth following the lessening of plant growth constraints (i.e., air and soil temperature, too much or little water) or post-disturbance recovery (Jones et al., 2013).

Similar to NDVI, we found that 74% (66%) of the VOD pixels having a significant increase (decrease) were associated with a GFED4s pixel indicating the occurrence of a fire disturbance. Across the domain we observed some regions where the trend direction in VOD matched that of NDVI (e.g., summer decrease in eastern Quebec, the Yukon Kuskokwim Delta, portions of southcentral Siberia; *SI Figures 12-j, 12-l*), though more often NDVI and VOD showed opposite direction in trends. This phenomenon has been reported elsewhere (Jones et al., 2013) and is common where there is post-disturbance greening while recovery in foliar biomass is lagging (e.g., portions of Canada and Interior Alaska impacted by wildfire). Similarly, the widespread positive trends in tree cover observed throughout the boreal zone (1997–2017; *SI Figure 6*) may also be associated with post-disturbance recovery.

3.2 Change Hotspot Assessments

Comparisons of the per-pixel based Theil-Sen and Getis-Ord Gi* results (SI 6) showed overall agreement in the locations of change activity for AT and ALT (*SI Figures 19-a, -c*). However, the Gi* assessment also indicated regional AT cooling (1997–2020) in eastern Canada, and warming across Alaska, which were not identified in the monotonic trend maps. Gi* showed areas of decreasing NFS and a larger expanse of decreasing PPT that were not apparent in the trend analysis (*SI Figure 19*). For SM, FW, NDVI and VOD, the trend and Gi* change maps generally agreed; however, the Gi* approach revealed a larger number of local clusters having indicator change (SI Figure 19). This was especially evident in the Gi* results for NDVI, where this approach identified much larger areas of annual non-frozen season NDVI browning on the order of 1.4x (boreal forests) to 4x (tundra) in Eurasia and 1.4x (boreal forest) to 3x (tundra) in North America. Gi* also detected a larger number of pixels having NDVI greening – averaging 1.65x higher in Eurasia and 1.45x in North America relative to the monotonic trend approach.

3.3. Gi*-informed Vulnerability Rankings

Our multivariate pixel- and ecoregion-based trend analysis for selected indicators (Figure 3) depicted thermal, moisture, and vegetation hotspots of change in many areas of the domain, especially within Eurasia. Corresponding increases in AT and ALT were observed over much of Siberia, northwest Canada and portions of Alaska including the North Slope. Additionally, a few areas in Siberia (central and eastern) experienced declines in annual NFS lengh in addition to increasing AT and ALT. The most substantial changes in moisture (decreasing PPT and SM, and increasing VPD) occurred in central Siberia. Although areas of decreasing NDVI were prevalent across North America and Eurasia, a few regions had larger areas of decreasing VOD.

Overall, our ecoregion-focused results found the most severe ecosystem changes (Table 1) occurring within the East Siberian taiga (a multivariate change score of 8). This was followed by ecoregions with total change scores of 7, such as Cherskii-Kolyma tundra, Taimyr tundra, Trans-Baikal mountain tundra and Trans-Baikal forests in eastern and central Siberia, and a few boreal forest regions in Canada (i.e., Northern Cordillera forests, Mid-Continental forests, Muskwa-Slave Lake forests, Northwest Territories taiga). Although extremely sparse in their spatial footprints considering the vast domain, field observations from the Siberian taiga have documented rapid changes in air temperature and precipitation, along with shortening frozen periods (Kirpotin, 2014; Czerniawska & Chlachula, 2020). Many of these areas have also experienced fire disturbances following high summer temperatures and water deficits (Talucci et al., 2022). In Canada, the boreal forests in British Columbia and southern Yukon (Cordillera forests) have experienced longer periods of summer warming and drought in recent years, increasing their susceptibility to fires (Chavardes et al., 2021). Similarly, substantial climate warming has been reported across the Northwest Territories, leading to fires, rapid permafrost thaw, changes in ground hydrology, and extreme wetting and drying events which continue to stress local ecosystems (e.g., Carpino et al., 2019).

4 Conclusions

Our study revealed widespread, long-term (40-yr and 24-yr) increases in air temperatures throughout Eurasia and western North America, with especially severe warming in Siberia, Alaska, and northwestern Canada. This arctic amplification is driven by multiple factors including loss of sea ice, (Kumar et al., 2010), changes in midlatitude circulation patterns (Rogers et al., 2022), and other factors (Pithan & Mauritsen, 2014). Across Siberia, air warming often coincided with substantial loss of frozen ground, observed through increases in permafrost active layer thickness. Substantial increases in active layer were also observed in some portions of Canada (often along the northern boreal) even through air warming trends were absent, which emphasizes the importance of other factors influencing permafrost thaw, including changes in albedo and local radiative effects, snow, hydrology and fire disturbance (Walvoord & Kurylyk, 2016; Biskaborn et al., 2019; Williams et al., 2020). In a few places (e.g., Sakha Republic and northern Kamchatka) increases in the length of annual non-frozen season (Zhang et al., 2011) further indicates severe warming.

Changes in wetness were most apparent in increasing vapor pressure deficit (indicating more aridity in the atmosphere) which, similar to air temperature, were widespread. These shifts are likely to heighten water stress in plants, especially when soil water recharge is limited, reducing growth, and increasing vulnerability of landscapes to fire (Sedano & Randerson, 2014; Helbig et al., 2020; Mirabel et al., 2023). Decreasing precipitation and soil moisture were not consistent across most of the domain, with exception of central Siberia (also see Bartsch et al., 2009) which emerged as a substantial hotspot. For vegetation, much of the domain showed browning (decreasing NDVI), largely driven by changes in late summer and autumn and likely influenced by both climate and disturbance (Kim et al., 2020), though local summer greening (increasing NDVI) was also observed. In some places (e.g., central Canada, the Lena River Delta, and the northern Sakha Republic) NDVI browning coincided with large-area decreases in foliar water content (and possibly biomass), indicated by VOD and likely influenced by changes in vapor pressure deficit and/or disturbance (Wang et al., 2023).

Continuous remote sensing records are invaluable for tracking environmental changes across vast, remove regions including the high latitudes. However, the ability to do so will ultimately depend on the continuation and expansion of in-situ observing stations (used for direct observation and the development of geospatial products) and satellite monitoring systems (Schuur & Mack, 2018; Duncan et al., 2022; Euskirchen et al., 2022). Further, to better understand how severe disturbances such as fire are driving change in this region, there is an urgent need for finer spatial scale mapping of present and historic fire events across the full Arctic-boreal zone (Potter et al., 2024).

Lastly, by assessing changes across various scales, we found that the patterns of trend and vulnerability varied greatly across time and space. This greatly emphasizes the need for future studies to focus on local (per-pixel) and neighborhood trends, instead of broad regionally-based averages which provide an incomplete representation of ecosystem change.

Acknowledgments

This project was made possible with funding from the Gordon and Betty Moore Foundation (grant no. 8414) and funding catalyzed by the Audacious Project (Permafrost Pathways). In addition, J.D.W. was supported by NASA TE 80NSSC22K1245. T.A.S. acknowledges the support received by the Beatriu de Pinòs Programme and the Ministry of Research and Universities of the Government of Catalonia (2020 BP 00126). Support for data processing was provided by the Environmental Systems Research Institute (Esri).

Data Availability

The data associated with this study are available through the Oak Ridge National Laboratory Distributed Active Archive Center for Biogeochemical Dynamics (ORNL DAAC): https://doi.org/10.3334/ORNLDAAC/2322

References

Abatzoglou, J. T., Dobrowski, S. Z., Parks, S. A., Hegewisch, K. C. (2018). TerraClimate, a high-resolution global dataset of monthly climate and climatic water balance from 1958-2015. *Scientific Data* , 5: 170191. https://doi.org/10.1038/sdata.2017.191

Andresen, C.G., Lawrence, D.M., Wilson, C.J., McGuire, A.D., Koven, C., Schaefer, K., Jafarov, E., Peng, S., Chen, X., Gouttevin, I., Burke, E., Chadburn, S., Ji, D., Chen, G., Hayes, D., Zhang, W. (2020) Soil moisture and hydrology projections of the permafrost region – a model intercomparison. *The Cryosphere* , 14: 445-459.

Bartsch, A., Balzter, H. ,George, C. (2009) The influence of regional surface soil moisture anomalies on forest fires in Siberia observed from satellites. *Environmental Research Letters* , 045021.

Beck, P.S.A., Goetz, S.J. (2011) Satellite observations of high northern latitude vegetation productivity changes between 1982-2008: ecological variability and regional differences. *Environmental Research Letters* , 6, 045501.

Berner, L.T., Massey, R., Jantz, P., Forbes, B.C., Macias-Fauria, M., Myers-Smith, I., et al. (2020) Summer warming explains widespread but not uniform greening in the Arctic tundra biome. *Nature Communications* , 11, 4621.

Berner, L.T., Goetz, S.J. (2022) Satellite observations document trends consistent with a boreal forest biome shift. *Global Change Biology* , 28: 3275-3292.

Bintanja, R., Selten, F.M. (2014) Future increases in Arctic precipitation linked to local evaporation and sea-ice retreat.*Nature* , 509: 479–482.

Bintanja, R., Andry, O. (2017) Towards a rain-dominated Arctic.*Nature Climate Change* , 7: 263-267.

Biskaborn, B.K., Smith, S.L., Noetzil, J., Matthes, H., Vieira, G., Streletskiy, D.A., Schoeneich, P., Romanovsky, V.E., Lewkowicz, A.G., Abramov, A., Allard, M., Boike, J., Cable, W.L., Christiansen, H.H., Delaloye, R., Djekmann, B., Drozdov, D., Etzelmuller, B.,, Grosse, G., Guglielmin, M., Ingeman-Nielsen, T., Isaksen, K., Ishikawa, M., Jonansson, M., et al., (2019) Permafrost is warming at a global scale.*Nature Communications* , 10: 264.

Bring, A., Fedorova, I., Dibike, Y., Hinzman, L., Mernild, S.H., Prowse, T., Semenova, O., Stuefer, S.L., Woo, M.-K. (2016) Arctic terrestrial hydrology: a synthesis of processes, regional effects, and research challenges. *JGR Biogeosciences* , 121: 621-649.

Brown, J, O Ferrians, J A Heginbottom, E Melnikov (2002) Circum-Arctic Map of Permafrost and Ground-Ice Conditions, Version 2. Boulder, Colorado USA. NSIDC: National Snow and Ice Data Center. doi: https://doi.org.

Bruhwiler, L., Parmentier, F.-J.W., Crill, P., Leonard, M., Palmer, P.I. (2021) The arctic carbon cycle and its response to changing climate.*Current Climate Change Reports* , 7: 14-34.

Box, J.E., Colgan, W.T., Christensen, T.R., Schmidt, N.M., Lund, M., Parmentier, F.-J., Brown, R., Bhatt, U.S., Euskirchen, E.S., Romanovsky, V.E. (2019) Key indicators of Arctic climate change: 1971-2017.*Environmental Research Letters* , 14, 045010.

Carpino, O.A., A.A. Berg, Q.L. Quinton, J.R. Adams (2018) Climate change and permafrost thaw-induced boreal forest loss in northwestern Canada.*Environmental Research Letters* , 13, 084018.

Chavardes, R.D., L.D. Daniels, J.E. Harvey, G.A. Greene, et al. (2021) Regional drought synchronized historical fires in dry forests of the Montane Cordillera Ecozone, Canada. *International Journal of Wildland*

Fire , 31: 67-80.

Chen, A., Lantz, T.C., Hermosilla, T., Wulder, M.A. (2021) Biophysical controls of increased tundra productivity in the western Canadian Arctic. *Remote Sensing of Environment* , 258, 112358.

Czerniawska, J., Chlachula, J. (2020) Climate-change induced permafrost degradation in Yakutia, East Siberia. *Arctic* , 72: 509-528.

de Jong, R., de Bruin, S., de Wit, A., Schaepman, M.E., Dent, D.L. (2021) Analysis of monotonic greening and browning trends from global NDVI time-series (2011) *Remote Sensing of Environment* , 115: 692-702.

Dinerstein, E, D Olson, A Joshi, C Vynne, N D Burgess, E Wikramanayake, N Hahn, S Palminteri, P Hedao, R Noss, M Hansen (2017) An ecoregion-based approach to protecting half the terrestrial realm.*BioScience* 67: 534-545.

Druckenmiller, M.L., Thoman, R.L., Moon, T.A. (2022) Arctic Report Card 2022. https://doi.org/10.25923/yix6-r184.

Du, J., Kimball, J. S. (2021). Daily Global Land Surface Parameters Derived from AMSR-E and AMSR2, Version 3. Boulder, Colorado USA. NASA National Snow and Ice Data Center Distributed Active Archive Center. doi: http://dx.doi.org/10.5067/JIKQZ6WO5C5M. [12/15/2020].

Duncan, B.N., Ott, L.E., Abshire, J.B., Brucker, L., et al. (2020) Space-based observations for understanding changes in the arctic-boreal zone. *Reviews of Geophysics* , 58. E2019RG000652.

Euskirchen, E.S., Bruhwiler, L.M., Commane, R., Parmentier, F.-J.W., Schadel, C., Schuur, E.A.G., Watts, J.D. (2022) Current knowledge and uncertainties associated with the Arctic greenhouse gas budget. In Balancing Greenhouse Gas Budgets, pp 159-201, Elsevier.

Feng, D., C.J. Gleason, P. Lin, X. Yang, M. Pan, Y. Ishitsuka (2021) Recent changes to Arctic river discharge. *Nature Communications* , 12, 6917.

Foster, A.C., Wang, J.A., Frost, G.V., Davidson, S.J., Hoy, E., Turner, K.W., Sonnentag, O., Epstein, H., Berner, L.T., Armstrong, A.H. (2022) Disturbances in North American boreal forest and Arctic tundra: impacts, interactions, and responses. *Environmental Research Letters* , 17, 113001.

Fujiwara, J. (2017) Flood risk and migration in the Sakha Republic (Yakutia). In: Hiyama, T., Takakura, H. (eds) Global Warming and Human – Nature Dimension in Northern Eurasia. Global Environmental Studies. Springer, Singapore. https://doi.org/10.1007/978-981-10-4648-3_8

Ge, Y., Dou, W., Liu, N. (2017) Planning resilient and sustainable cities: identifying and targeting social vulnerability to climate change. *Sustainability* , 9, 1394.

Giglio, L., Boschetti, L., Roy, D., Hoffmann, A. A., Humber, M., Hall, J. V. (2020) Collection 6 MODIS Burned Area Product User's Guide Version 1.3. NASA Technical User's Guide for MCD64A1. https://modis-fire.umd.edu/files/MODIS_C6_BA_User_Guide_1.3.pdf

Guay, K. C., Beck, P. S. A. Goetz, S.J. (2015). Long-Term Arctic Growing Season NDVI Trends from GIMMS 3g, 1982-2012. Data set. Available on-line [http://daac.ornl.gov] from Oak Ridge National Laboratory Distributed Active Archive Center, Oak Ridge, Tennessee, USA. http://dx.doi.org/10.3334/ORNLDAAC/1275

Hansen, M., Song, X. (2018). Vegetation Continuous Fields (VCF) Yearly Global 0.05 Deg [VCF5KYR.001]. NASA EOSDIS Land Processes DAAC. Accessed 2022-01-03 from https://doi.org/10.5067/MEaSUREs/VCF/VCF5KYR.001

Helbig, M., Wischnewski, K., Kljun, N., et al. (2016) Regional atmospheric cooling and wetting effect of permafrost thaw-induced boreal forest loss. *Global Change Biology* , 22: 4048–4066.

Helbig, M., Waddington, J.M., Alekseychik, P., Amiro, B.D., Aurela, M., Barr, A.G., et al. (2020) Increasing contribution of peatlands to boreal evapotranspiration in a warming climate. *Nature Climate Change* , 10: 555-560.

Hersbach, H., Bell, B., Berrisford, P., Hirahara, S., Horanyi, A., et al. (2020) The ERA5 global reanalysis. *Q. J. R. Meteorol. Soc.* , 146, 1999-2049. Doi:10.1002/qj.3803.

Hicks Pries, C.E., McLaren, J.R., Smith Vaughn, L., Treat, C., Voigt, C. (2022) The changing biogeochemical cycles of tundra. In: Multi-scale Biogeochemical Processes in Soil Ecosystems: Critical Reactions and Resilience to Climate Changes. https://doi.org/10.1002/9781119480419.ch7.

Holloway, J.E., Lewkowicz, A.G., Douglas, T.A., Li, X., Turetsky, M.R., Baltzer, J.L., Jun, H. (2020) Impact of wildfire on permafrost landscapes: a review of recent advances and future prospects. *Permafrost and Periglacial Processes* , 31: 371-382.

Huang, Q., Ma, N., Wang, P. (2022) Faster increase in evapotranspiration in permafrost-dominated basins in the warming Pan-Arctic. *J. Hydrology* , 615, 128678.

Jones, M.O., Kimball, J.S., Jones, L.A. (2013) Satellite microwave detection of boreal forest recovery from the extreme 2004 wildfires in Alaska and Canada. *Global Change Biology* , 19: 3111-3122.

Karesdotter, E., Destouni, G., Ghajarnia, N., Hugelius, G., Kalantari, Z. (2021) Mapping the vulnerability of arctic wetlands to global warming. *Earth's Future* , 9, e2020EF001858.

Keenan, T.F., Riley, W.J. (2018) Greening of the land surface in the world's cold regions consistent with recent warming. *Nature Climate Change* , 8: 825-828.

Kowe, P., Mutanga, O., Odindi, J., Dube, T. (2019) Exploring the spatial patterns of vegetation fragmentation using local spatial autocorrelation indices. *Journal of Applied Remote Sensing* , 13, 024523.

Kim, Y., Kimball, J.S., Zhang, K., McDonald, K.C. (2012) Satellite detection of increasing Northern Hemisphere non-frozen seasons from 1979 to 2008: Implications for regional vegetation growth. *Remote Sensing of Environment* , 121: 472-487.

Kim, Y. ,Kimball, J.S., Parazoo, N., Kirchner, P. (2020) Diagnosing environmental controls on vegetation greening and browning trends over Alaska and Northwest Canada using complementary satellite observations. In: Yang, D., Kane, D.L., (eds) Arctic Hydrology, Permafrost, and Ecosystems. Pp. 583-613. Doi.org/10.1007/978-3-030-50930-9_20.

Kim, Y., Kimball, J. S., Du, J., Kundig, T. (2021) A Global Data Record of Daily Landscape Freeze/Thaw Status Version 5.0. MEaSUREs Global Record of Daily Freeze/Thaw [1975 to 2020]. Boulder, Colorado, USA: National Snow and Ice Data Center. Digital media (http://dx.doi.org/10.5067/MEASURES/CRYOSPHERE/nsidc-0477.004)

Kirpotin, S.N. (2014) Western Siberia in a changing climate. *International Journal of Environmental Studies* , 71: 591-594.

Kumar, A., Perlwitz, J., Eischeid, J., Quan, X., Xu, T., Zhang, T., Hoerling, M., Jha, B., Wang. W. (2010) Contribution of sea ice loss to Arctic amplification. *Geophysical Research Letters* , 37. https:/doi.org/10.1029/2010GL045022.

Li, C., Huang, H., Sun, F. (2021) A pixel-based greenness trend analysis over the Russian tundra with all available Landsat data from 1984 to 2018. *Remote Sensing* , 13, 4933.

Liu, L., Chen, X., Ciais, P., Yuan, W., Maignan, F., Wu, J., et al. (2022) Tropical tall forests are more sensitive and vulnerable to drought than short forests. *Global Change Biology* , 28: 1583–1595.

Magnusson, R.I., Groten, F., Bartholomeus, H., van Huissteden, K., Heijmans, M.P.D. (2023) Tundra browning in the Indigirka Lowlands (North-Eastern Siberia) explained by drought, floods, and small-scale vegetation shifts. *JGR Biogeosciences* , 128. https://doi.org/10.1029/2022JG007330.

Meredith, M., Sommerkorn, M., Cassotta, S., Derksen, C., Ekaykin, A., Hollowed, A., Kofinas, G., et al. (2019). Polar Regions. In: IPCC Special Report on the Ocean and Cryosphere in a Changing Climate. [H.-O. Portner, D.C. Roberts, V. Masson-Delmotte, P. Zhai, M. Tignor, E. Poloczanska, K., Mintebeck, A. Alegria, M. Nicolai, A. Okem, J. Petzold, B. Rama, N.M. Weyer (eds.)]. Cambridge University Press, Cambridge, UK, and New York, NY, USA. Pp. 203-320. https://doi.org/10.1017/9781009157964.005.

Miner, K.R., Turetsky, M.R., Malina, E., Bartsch, A., Tamminen, J., McGuire, A.D., Fix, A., Sweeney, C., Elder, C.D., Miller, C.E. (2022) Permafrost carbon emissions in a changing Arctic. *Nature Reviews Earth & Environment* , 3, 55-67. https://doi.org/10.1038/s43017-021-00230-3

Mirabel, A., Girardin, M.P., Metsaranta, J., Way, D., Reich, P.B. (2023) Increasing atmospheric dryness reduces boreal forest tree growth.*Nature Communications* , 14, 6901.

Mitchell, A (2005) The ESRI guide to GIS Analysis. Volume 2. ESRI. Press.

Moesinger, L., Dorigo, W., de Jeu, R., van der Schalie, R., Scanlon, T., Teubner, I., Forkel, M. (2020). The global long-term microwave vegetation optical depth climate archive (VODCA). *Earth Syst. Sci. Data* , 12, 177-196. https://doi.org/10.5194/essd-12-177-2020.

Myers-Smith, I.H., Kerby, J.T., Phoenix, G.K., Bjerke, J.W., Epstein, H.W., Assman, J.J., John, C., et al. (2020) Complexity revealed in the greening of the Arctic. *Nature Climate Change* , 10: 106-117.

Muñoz-Sabater, J., Dutra, E., et al. (2021). ERA5-Land: A state-of-the-art global reanalysis dataset for land applications.*Earth Syst. Sci. Data* , 13, 4349-4383

Natali, S., & Watts, J.D., Rogers, B.M., Potter, S., Ludwig, S.M., et al. (2019) Large loss of CO2 in winter observed across the northern permafrost region. *Nature Climate Change* , 9: 852-857.

Obu, J.,Westermann, S., Barboux, C., Bartsch, A., Delaloye, R., Grosse, G., Heim, B., Hugelius, G., Irrgang, A., Kääb, A. M., Kroisleitner, C., Matthes, H., Nitze, I., Pellet, C., Seifert, F. M., Strozzi, T., Wegmüller, U., Wieczorek, M., Wiesmann, A. (2021). ESA Permafrost Climate Change Initiative (Permafrost_cci): Permafrost active layer thickness for the Northern Hemisphere, v3.0. NERC EDS Centre for Environmental Data Analysis, 28 June 2021.

http://dx.doi.org/10.5285/67a3f8c8dc914ef99f7f08eb0d997e23

Overland, J., Dunlea, E., Box, J.E., Corell, R., Forsius, M., Kattsov, V., Olsen, M.S., Pawlak, J., Reiersen, L-O., Wang, M. (2019) The urgency of Arctic change. *Polar Science* , 21: 6-13.

Peng, C., Ma, Z., Lei, X., Zhu, Q., et al. (2011) A drought-induced pervasive increase in tree mortality across Canada's boreal forests.*Nature Climate Change* , 1: 467–471.

Phoenix, G.K., Bjerke, J.W. (2016) Arctic browning: extreme events and trends reversing arctic greening. *Global Change Biology* , 22: 2960-2962.

Pithan, F., Mauritsen, T. (2014) Arctic amplification dominated by temperature feedbacks in contemporary climate models. *Nature Geosciences* , 7: 181-184.

Potter, Stefano, Yang, Y., Burrell, A., Talucci, A., Veraverbeke, S., Anderson, J.T., Goetz, S.J. Berner, L.T., Mack, M.C., Walker, X., Natali, S.M., Rogers, B.M. (2024) Mapping Boreal and Tundra North American Burned Area Using Convolutional Neural Networks. In Review at*Remote Sensing of Environment* .

Qian, B., Gregorich, E.G., Gameda, S., Hopkins, D.W., Wang, X.L. (2011) Observed soil temperature trends associated with climate change in Canada. *JGR Atmospheres* , 116. https://doi.org/10.1029/2010JD015012.

Randerson, J.T., G.R. van der Werf, L. Giglio, G.J. Collatz, and P.S. Kasibhatla. 2018. Global Fire Emissions Database, Version 4, (GFEDv4). ORNL DAAC, Oak Ridge, Tennessee, USA. *https://doi.org/10.3334/ORNLDAAC/1293*

Rantanen, M., Karpechko, A.Y., Lipponen, A., Nordling, K., Hyvarinen, O., Ruosteenoja, K., Vihma, T., Laakonen, A. (2022) The Arctic has warmed nearly four times faster than the globe since 1979. *Nature Communications Earth & Environment* , 3, 168.

Rogers, C.D.W., Kornhuber, K., Perkins-Kirkpatrick, S.E., Loikith, P.C., Singh, D. (2022) Sixfold increase in historical Northern Hemisphere concurrent large heatwaves driven by warming and changing atmospheric circulations. *Journal of Climate* . DOI: 10.1175/JCLI-D-21-0200.1

Schuur, E.A.G., McGuire, A.D., Schadel, C., Grosse, G., Harden, J.W., Hayes, D.J., Hugelius, G., Koven, C.D., Kuhry, P., Lawrence, D.M., Natali, S.M., et al. (2015) Climate change and the permafrost carbon feedback. *Nature* , 520, 171-179.

Schuur, E.A.G., & Mack, M.C. (2018) Ecological response to permafrost thaw and consequences for local and global ecosystem services.*Annual Reviews of Ecology, Evolution, and Systematics* , 49, 279-301, https://doi.org/10.1146/annurev-ecolsys-121415-032349.

Sedano, F., Randerson, J.T. (2014) Multi-scale influence of vapor pressure deficit on fire ignition and spread in boreal forest ecosystems. *Biogeosciences* , 11: 3739-3755.

Strand, S.M., Christiansen H.H., Johansson, M., Akerman, J., Humlum, O. (2020) Active layer thickening and controls on interannual variability in the Nordic Arctic compared to the circum-Arctic. *Permafrost & Periglacial Processes* , 32: 47-58.

Talucci, A.C., Loranty, M.M., Alexander, H.D. (2022) Siberian taiga and tundra fire regimes from 2001-2020. *Environmental Research Letters* , 17. Doi: 10.1088/1748-9326/ac3f07.

Thoman, R.L., Moon, T.A., Druckenmiller, M.L. (2023) Arctic Report Card 2023. http://doi.org/10.25923/5vfa-k694.

Walvoord, M.A., Kurylyk, B.L. (2016) Hydrologic impacts of thawing permafrost – a review. *Vadose Zone Journal* . https://dor.org/10.2136/vzj2016.01.0010.

Wang, J.A., Friedl, M.A. (2019) The role of land cover change in Arctic-boreal greening and browning trends. *Environmental Research Letters* , 14, 125007.

Wang, J., Yuan, Q., Shen, H., Liu, T., Li, T., Yue, L., Shi, X., Zhang, L. (2020) Estimating snow depth by combining satellite data and ground-based observations over Alaska: A deep learning approach.*J. Hydrology* , 585.

Wang, Y.-R., Hessen, D.O., Samset, B.H., & Stordal, F. (2022) Evaluating global and regional land warming trends in the past decades with both MODIS and ERA5-Land land surface temperature. *Remote Sensing of Environment* , 280, https://doi.org/10.1016/j.rse.2022.113181.

Wang, T., Zhang, H., Zhao, J., Wu, R., Li, H., Guo, X., Zhao, H. (2023) Increased atmospheric moisture demand induced a reduction in the water content of boreal forest during the past three decades.*Agricultural and Forest Meteorology* , 342, 109759.

Watts, J.D., Natali, S.M., Minions, C., Risk, D., Arndt, K., Zona, D., Euskirchen, E.S., Rocha, A.V., et al. (2021) Soil respiration strongly offsets carbon update in Alaska and northwest Canada.*Environmental Research Letters* , 16, 084051.

Watts, J.D., Farina, M., Kimball, J.S., Schiferl, L., et al. (2023) Carbon uptake in Eurasian boreal forests dominates the high-latitude net ecosystem carbon budget. *Global Change Biology* , 29: 1870-1889.

Webb, E.E., A.K. Liljedahl, J.A. Cordeiro, M.M. Loranty, C. Witharana, J.W. Lichstein (2022) Permafrost thaw drives surface water decline across lake-rich regions of the Arctic. *Nature Climate Change* . https://doi.org/10.1038/s41558-022-01455-w.

Williams, M., Zhang, Y., Estop-Aragones, C., Fisher, J.P., Xenakis, G., Charman, D.J., Hartley, I.P., Murton, J.B., Phoenix, G.K. (2020) Boreal permafrost thaw amplified by fire disturbance and precipitation increases. *Environmental Research Letters* , 15. DOI: 10.1088/1748-9326/abbeb8.

Xie, Y., Wu, G., Liu, Y., Huang, J., Nie, H. (2021) A dynamic and thermodynamic coupling view of the linkages between Eurasian cooling and Arctic warming. *Climate Dynamics* , 58: 2725-2744.

Zhang, K., Kimball, J.S., Kim, Y., McDonald, K.C. (2011) Changing freeze-thaw seasons in northern high latitudes and associated influences on evapotranspiration. *Hydrological Processes* , 25: 4142-4151.

Zona, D., Lafleur, P.M., Hufkens, K., Gioli, B., Bailey, B., Burba, G., Euskirchen, E.S., Watts, J.D., Arndt, K., Farina, M., et al. (2023) Pan-arctic soil moisture control on tundra carbon sequestration and plant productivity. *Global Change Biology* . https://doi.org/10.1111/gcb.16487.

Figures

Figure 1. Regional changes over North America and Eurasia, and their tundra and boreal sub-regions. Indicators are: (a) near-surface air temperature (AT; °C); (b) non-frozen season (NFS; days per year); (c) active-layer thickness (ALT; m); (d) precipitation (PPT; m); (e) non-winter vapor pressure deficit (VPD; kPa); (f) sum of winter snow cover (SC; million km^2); (g) soil moisture (SM; cm^3 cm^{-3}); (h) surface fractional water coverage (FW; %); (i) non-frozen season normalized difference vegetation index (NDVI; unitless); (j) non-frozen season vegetation optical depth (VOD; unitless); (k) pixel-percent tree cover (TC; %); (l) pixel-percent non-tree cover (NTC; %).

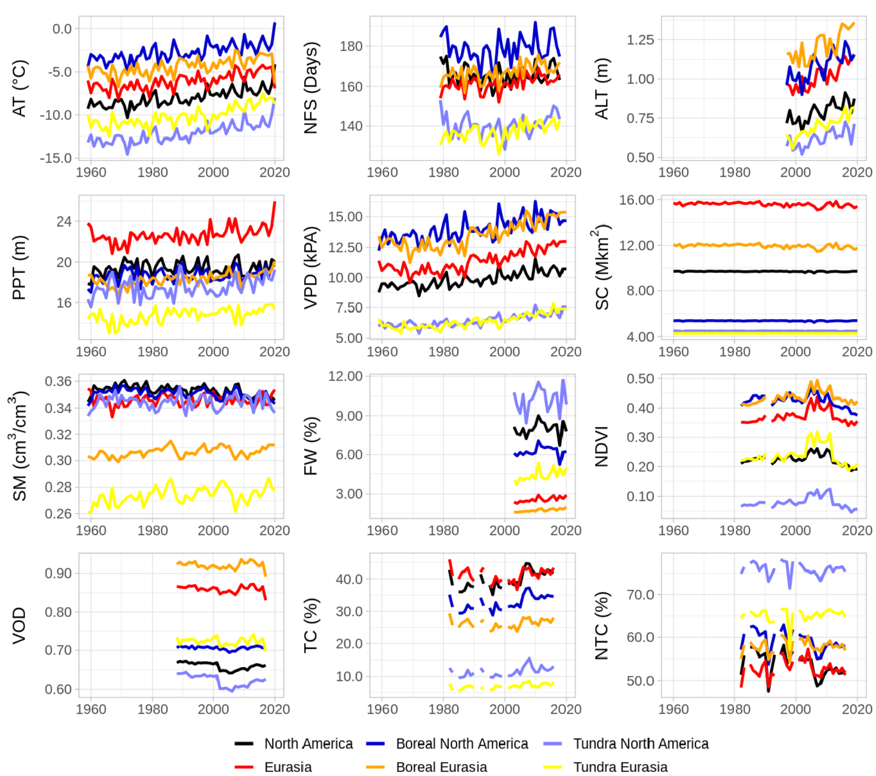

Figure 2. Percent of total regional area showing a significant increasing (red) or decreasing (blue) trend

in Indicator status over the 1997–2020 period, according to boreal forest (BF), boreal wetland (BWL), boreal non-forest (BNF; including shrubland and grassland, G/S), and tundra (TUN) for Eurasia and North America. Indicators include: (a) annual average AT (°); (b) annual total NFS (days); (c) annual maximum ALT (m); (d) annual total PPT (m); (e) annual total winter SC (Mkm^2); (f) annual average VPD (kPa); (g) annual non-frozen season SM (cm^3/cm^3); (h) annual average non-frozen season FW (% pixel coverage); (i) annual non-frozen season NDVI (unitless); (j) annual non-frozen VOD (unitless).

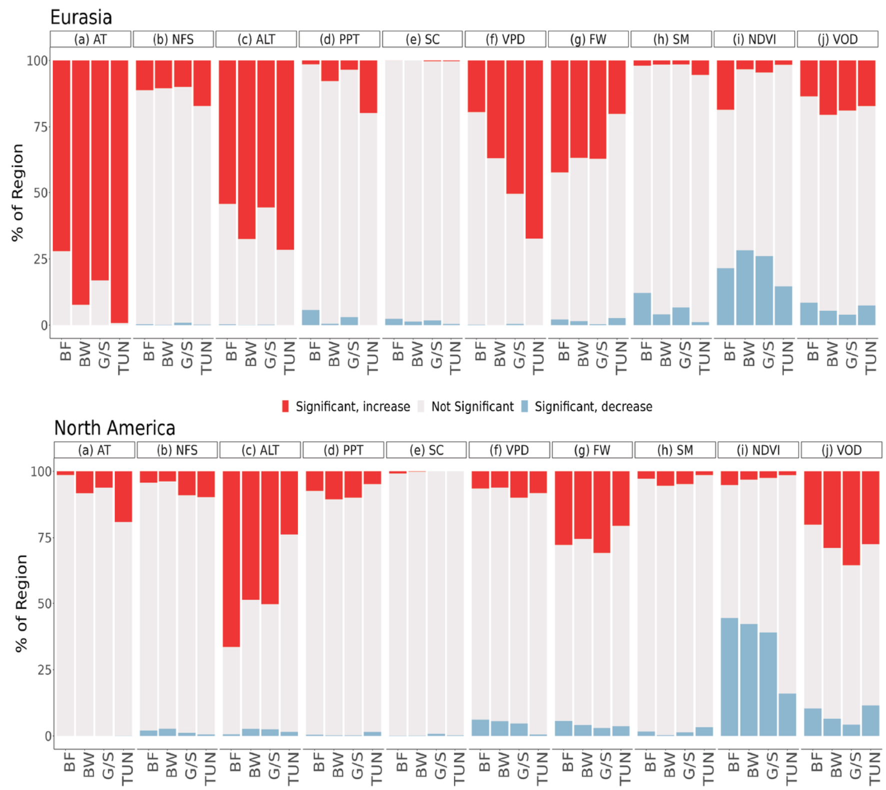

Figure 3. Multivariate change hotspot maps for the 1997–2020 period (unless otherwise indicated), according to select directional changes in thermal, moisture, and vegetation Indicators. Thermal includes: average increase in annual AT (°C); increase in annual NFS (days); and increase in annual ALT (m). Moisture includes: decrease in annual PPT (m); increase in annual VPD (kPa); decrease in annual non-frozen season SM (cm^3 cm^{-3}). Vegetation includes decreases in annual non-frozen season average NDVI (unitless; 1998–2020) and VOD (unitless; 1998–2017). Panels (a) through (c) show identified change hotspots based on pixel-level analyses; (d) through (f) show Indicator change across individual ecoregions.

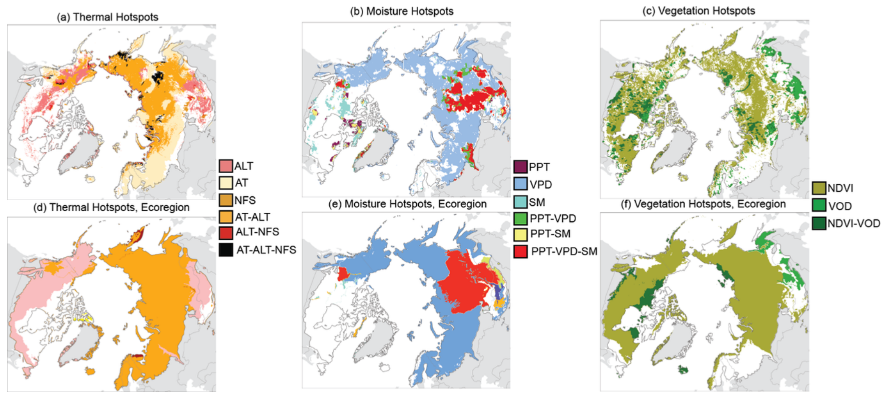

Table 1 Most vulnerable Arctic-boreal ecoregions identified according to per-pixel multivariate indicator hotspot results (Figure 3) having a total score of 6 or above. Scores were obtained by assigning a point (1) for each thermal, moisture, and vegetation Indicator hotspot. The full list of ecoregion scores is provided in SI Table 8.

Rank	Ecoregion Name	Continent	Ecoregion Area (km^2)	Permafrost Affected?	*Ther*
1	East Siberian Taiga	EA	3.92E+06	Yes	3
2	Cherskii-Kolyma mountain tundra	EA	5.60E+05	Yes	3
2	Northern Cordillera forests	EA	2.64E+05	Yes	3
2	Taimyr-Central Siberian tundra	EA	9.62E+05	Yes	3
2	Trans-Baikal Bald Mountain tundra	EA	2.19E+05	Yes	2
2	Trans-Baikal conifer forests	EA	2.01E+05	Yes	2
2	Mid-Continental Canadian forests	NA	3.70E+05	Yes	2
2	Muskwa-Slave Lake forests	NA	2.64E+05	Yes	2
2	Northwest Territories taiga	NA	3.48E+05	Yes	2
3	Middle Arctic tundra	NA	1.03E+06	Yes	2
3	Da Hinggan-Dzhagdy Mountains conifer forests	EA	2.47E+05	Yes	2
3	Daurian forest steppe	EA	2.10E+05	Yes	2
3	Eastern Gobi desert steppe	EA	1.05E+04	Yes	2
3	Mongolian-Manchurian grassland	EA	2.79E+05	Yes	2
3	Northeast Siberian taiga	EA	1.13E+06	Yes	2
3	Okhotsk-Manchurian taiga	EA	4.04E+05	Yes	2
3	Sayan Alpine meadows and tundra	EA	8.11E+04	Yes	2
3	Sayan montane conifer forests	EA	2.98E+05	Yes	2
3	South Siberian forest steppe	EA	2.70E+04	Yes	2
3	West Siberian taiga	EA	1.68E+06	Yes	2

Supplemental Information (SI)

1. Description of Remote Sensing and Climate Data Indicators

1.1 Geospatial Indicators

A brief description of each Indicator is provided below (and summarized in SI Table 1). Please refer to the referenced publications for additional details.

ERA5 is the fifth generation ECMWF (European Centre for Medium-Range Weather Forecasts) atmospheric reanalysis of global climate (Hersbach et al., 2020) produced by the Copernicus Climate Change Service.

ERA5 atmospheric, oceanic and land climate variable products are obtained using physically based models guided using data assimilation (see documentation for CY47; ECMWF 2021). The data assimilation system for ERA5 includes a wide array of global observations from satellite, oceanographic and land sensors (e.g., see https://apps.ecmwf.int/odbgov/reporttype/). The ERA5-Land records provide hourly climate variable estimates from 1950–present at 0.01 degree resolution, which are obtained through the atmospheric forcing (using ERA5) of a land surface model (i.e., ECMWF Scheme for Surface Exchanges over Land, incorporating land surface hydrology: H-TESSEL). These variables included monthly average near-surface (2-m) air temperature (AT; °C), total monthly precipitation (PPT; m), soil moisture (SM; cm^3 cm^{-3}; for the uppermost 7 cm of soil) and per pixel percentage snow cover (SC). To obtain monthly average vapor pressure deficit (VPD; kPa), we used the Plantecophys package in R (Duursma 2015) which uses input AT and 2 m dew point temperature. More information about ERA5-Land is provided through Muñoz-Sabater et al. (2021). For this assessment, we first calculated the monthly average SC area, and then obtained an annual or seasonal total (km^2). For SM, we obtained monthly average estimates over the annual soil non-frozen period based on microwave surface frozen/unfrozen status records.

The NASA MEaSUREs (Making Earth System Data Records for Use in Research Environments) land surface freeze-thaw (FT) database is derived from 37 GHz (V-pol) satellite brightness temperature (T_b) observations from the Scanning Multichannel Microwave Radiometer (SMMR), Special Sensor Microwave Imager (SSM/I), and SSM/I Sounder (SSMIS) sensors (Kim et al., 2021). The FT database provides a daily record indicating surface frozen, unfrozen, or transitional (AM frozen and PM thawed) state at a 25-km resolution from 1979–2020. See Kim et al. (2017) for a detailed description of the FT algorithm. For this study we focused on the annual duration (days) of the surface non-frozen season (NFS; see *SI Section 2.1*).

Permafrost active layer thickness (ALT; m) data from the European Space Agency's (ESA) Climate Change Initiative (CCI) permafrost project, part of ESA's Climate Research Data Package Version 2 (CRDP V2), was derived from a ground thermal model (i.e., CryoGrid) constrained by MODIS (Moderate Resolution Imaging Spectroradiometer) Land Surface Temperature (MOD11; Wan, 2013) satellite data merged with downscaled ERA5 reanalysis (Hersbach et al., 2020) near-surface air temperature data (Obu et al., 2021). CryoGrid is also constrained by 300-m MERIS (Medium Resolution Imaging Spectrometer) based ESA CCI Landcover (ESA, 2017). The resulting ALT, which is the annual maximum depth of seasonal ground thaw per ~ 927-m grid cell, is obtained by identifying the depth at which CryoGrid model-estimated soil temperatures continuously remain $< 0^{\circ}$ C each year. Although known problems with the magnitude of estimated ALT exist (substantial underestimation of ALT relative to observation sites, i.e., root mean square errors of 0.25 ($<$ 1 m depth) to 0.5 m ($>$ 1 m depth); Bartsch et al., 2020) we include this product because it remains the most widely used pan-Arctic product available to date, and because even with the known bias it is useful for identifying regions where ground thaw may be accelerating.

The AMSR (Advanced Microwave Scanning Radiometer) global land parameter database integrates calibrated brightness temperature (T_b) retrievals from NASA AMSR-E (AMSR for Earth Observing System) and JAXA (Japan Aerospace Exploration Agency) AMSR-2 sensors to simultaneously obtain daily air temperature (at 2 m height), fractional cover of open water on land (FW), vegetation canopy microwave transmittance, surface soil moisture, and atmospheric water vapor content (Jones et al., 2011) over years 2003–2020. The integrated land surface parameter retrieval algorithm is based on a forward radiometric model which uses AMSR 18.7 and 23.8 GHz (horizontal) H- and (vertical) V- T_b to estimate FW – the open water fraction in the sensor field of view – at a 25-km resolution (Watts et al., 2012). Prior to algorithm input, T_b data are screened and removed for precipitation events, radio frequency interference and frozen or snow-covered conditions. The most recent version of the AMSR land parameter database is described in Du et al. (2017) and Du & Kimball (2021). Passive microwave sensing is especially advantageous in high latitude environments as it provides high frequency observations that are relatively insensitive to atmospheric conditions (e.g., water vapor and particulates) and are not impacted by changes in solar radiation that can greatly affect optical/near-infrared retrievals. Both morning (AM; descending pass) and afternoon (PM; ascending pass) passes are available for the AMSR global land parameter database. FW retrievals do not occur under frozen surface conditions. For our assessment of FW (% coverage per 25 x 25 km grid cell), we used the records provided with a 60-day per-pixel smoothed average (i.e., average over 60 preceding days) and averaged the FW coverage over the annual non-frozen period, or spring, summer and autumn months.

The GIMMs3g product refers to the third generation Global Inventory Monitoring and Modeling System (GIMMS) NDVI from AVHRR (Advanced Very High-Resolution Radiometer). The NDVI (unitless) is a widely used vegetation index that utilizes shorter-wave spectral reflectance characteristics within red (˜600 to 700 nm) and infrared (˜ 700 to 1000) bands to track relative vegetation density and health (see Du et al., 2019; Duncan et al., 2019). For example, higher NDVI corresponds to denser vegetation; lower NDVI tends to indicate sparse vegetation coverage or unhealthy or senescing vegetation. The GIMMS3g NDVI observations are provided at ˜8-km resolution (0.08°) with 15-day coverage from 1982 through 2017 (Pinzon et al., 2014). Over high latitude regions, the GIMMS3g record covers summer months when lowlight conditions and snow cover are not problematic. For this assessment, we only used high quality NDVI pixels (according to pixel QAQC flags); those not meeting this standard were removed, including following the 1991 eruption of Mount Pinatubo which severely reduced optical clear sky retrievals.

The global long-term microwave Vegetation Optical Depth Climate Archive (VODCA) product integrates passive microwave observations from multiple sensors including SSM/I, TMI (TRMM Microwave Imager), AMSR-E, WindSat, and AMSR2 within a radiometric Land Parameter Retrieval Model to track vegetation biomass characteristics (Moesinger et al., 2020). Vegetation optical depth (VOD; unitless) uses information from microwave bands to describe the attenuation of longer-wave energy (primarily due to water content) by aboveground biomass. Higher VOD values are associated with more water content. The VODCA product provides three options for daily observed VOD: 1) derived from Ku-band T_b (from 1987–2017); 2) derived from K-band T_b (from 1997–2018); 3) derived from C-band T_b (from 2002–2018). The differing temporal periods of the VOD products reflects sensor operational status. Generally, estimates of VOD derived from longer wavelengths (i.e., C-band) are more sensitive to stem/woody biomass whereas VOD from shorter wavelengths (i.e., Ku-band) are more sensitive to leaf moisture content. For this analysis, we focused on the 0.25° Ku-derived VOD record (spring, summer and autumn months only) due to the longer observational period and sensitivity to leaf water stress. The dataset spans the full 1987–2017 time series with the exception of spring months in 1987, and autumn months in 2017.

We included the NASA MEaSUREs Vegetation Continuous Fields (VCF) Version 1 data product at a 0.05° resolution (VCF5KYR v001) to assess how changes in tree cover might be influencing observed trends in NDVI and VOD. The VCF uses long-term information from AVHRR and MODIS to estimate percent of tree cover, non-tree vegetation and bare ground within each pixel (Hansen et al., 2017; Hansen & Song, 2018). The AVHRR NDVI time series, spanning multiple NOAA (US National Oceanic and Atmospheric Administration) satellites and AVHRR sensors, was first normalized using calibrated observations from MODIS to remove artifacts resulting from changes in sensor design, observational solar zenith angles, orbital drift, and sensor degradation (Song et al., 2018). Supervised regression trees were then developed using normalized AVHRR observations and training data from the circa-2000 30-m Landsat Vegetation Continuous Fields (VCF) percent tree cover product (Sexton et al., 2016). The VCF percent TC and NTC product estimates are not available in 1991/1992 and 2000.

1.2 Ancillary geospatial data

Additional geospatial information used in this study included merged vegetation cover from the Circumpolar Arctic Vegetation Map (CAVM; Walker et al., 2005) and the ESA CCI-LC 2010 Epoch land cover product (Kirches et al., 2014) – see Watts et al. (2023) – in addition to permafrost categories from Brown et al. (2002) and ecoregion boundary information from Olson et al. (2001). The spatial distribution of vegetation cover and permafrost, and the ecosystem boundaries, are shown in SI Figure 1.

We also used the Global Fire Emissions Database, Version 4.1 (GFED4s) which provides global estimates of monthly burned area, gas and particulate emissions (van der Werf et al., 2017; Randerson et al., 2018). The dataset, spanning 1997 through 2016, was produced by combining 500-m MODIS Collection 5.1 burned area (MCD64A1) maps with active fire data (˜ 0.25°) from the Visible and Infrared Scanner (VIRS) and ATSR

(Along-Track Scanning Radiometer) sensors. The GFED4 product is provided at a 0.25° resolution. We include this product to understand the influence of fire disturbance on identified trends within the thermal, moisture and vegetation indicators.

2. Data Processing Steps and Statistical Analysis

2.1 Temporal aggregation

We acquired raster files for all indicator variables at their native resolutions (SI Table 1; SI Section 1).

The ERA5 AT, PPT and VPD records at monthly temporal resolution were aggregated to provide yearly grid cell averages (AT, VPD) and totals (PPT) across annual (all months), spring (March – May), summer (June – August), and autumn (September – November) periods each year. For AT we also obtained winter (December – February) averages. The AMSR surface FW records were aggregated to averages for the spring (when flooding is typically more rampant), summer and autumn periods. For GIMMS3g NDVI and VODCA VOD records, the grid cell data were aggregated to obtain annual non-frozen season, spring, summer and autumn averages for each year (excluding pixels where snow was present). To identify the annual and seasonal depth of soil thaw for permafrost regions, we obtained the estimates directly from the ESA CCI permafrost product. Similarly, annual observations of per-pixel percent TC and NTC were obtained directly from the VCF5KYR v001 records.

The NFS length was derived from the SMMR/SSMI/SSMIS Land Surface Freeze/Thaw State record. We used the "Combined" FT product (Kim et al., 2017, 2021), which uses information from morning (AM) and afternoon (PM) satellite passes. To identify the timing (i.e., day of year) and duration of annual surface frozen season for each grid cell, we applied a "80% rule" moving window approach developed by Kim et al. (2012) for the northern hemisphere. This approach identifies the primary date of annual surface thaw as the first day when 12 out of 15 consecutive days are classified as non-frozen (thawed) by the FT algorithm between January through June. The primary date of annual surface freeze is the first day when 12 out of 15 days are classified as frozen within the September through December period. Similarly, we also used the 80% rule 15-day moving window approach to identify the first and last dates of annual SC within the ERA5 snow cover product. Annual surface non-frozen season length was calculated for each grid cell (using each product's native grid) as the total days between the identified thaw and freeze dates and identified snow-off and snow-on dates. We also calculated the NF days for spring and autumn periods. For autumn, winter, and spring SC we calculated the total pixel snow covered area as indicated by the ERA5 records for the given periods. For ERA5 SM we only included estimates over the annual non-winter period (spring through autumn).

For SC, we first determined snow covered area per pixel by multiplying the coverage fraction by the cell size area. We then obtained the average of SC area in a pixel stack for each individual month. Next, we took the average snow cover area for each season. To assess SC change within a domain, we then summed up total seasonal coverage.

Maps of the average annual state of each Indicator, at their respective native resolutions, are shown in SI Figure 2.

2.2 Change detection approaches

2.2.1 Trend analysis

As described in the main body of the manuscript, we applied a non-parametric Mann-Kendall test that detects monotonic upward or downward trend. For this we used the ZYP package in R, Version 0.10-1.1 (Bronaugh & Werner, 2013) that provides z-scores and associated p-values. We then used the Theil-Sen estimator of slope (median-based) for each time series where trend significance was detected. We applied this approach according to region-based averages over: 1) the full (FD) domain which encompasses northern North America (NA) and Eurasia (EA) zones; 2) individual NA and EA zones; 3) NA and EA zones separated according to tundra and boreal land cover. This approach has often been used in past assessments of high latitude change. We then used a more detailed approach by applying the Mann-Kendall and Theil-Sen estimators to individual pixel-based time series. This step allowed us to diagnose more localized changes that may not be reflected in Indicator averages over large regions.

2.2.2 Change spot analysis

Unlike the Mann-Kendall approach, change spot analysis uses neighborhood-based statistics to detect significant clusters of change. For this we used the Environmental Science Research Institute (ESRI; https://www.esri.com/en-us/home) ArcGIS Pro version 2.9 software and the ESRI Emerging Hotspot Analysis (EHA; https://pro.arcgis.com/en/pro-app/2.8/tool-reference/space-time-pattern-mining/emerginghotspots.htm) algorithm. To identify change "hot spots", the EHA first applies a Getis-Ord Gi* spatial statistic, which examines each pixel within the context of the neighboring pixels. A pixel surrounded by neighboring high (low values) is more likely to be a hot (cold) change spot respectively. The Getis-Ord Gi* statistic outputs z-scores and p-values and a hotspot bin classification. These hot and cold spot classifications are then evaluated with a Mann-Kendall trend test (Mann, 1945), which itself results in a z-score and p-value for each pixel within the temporal data. These z-scores and p-values are then used to determine the confidence of an emerging hot or cold spot. Output values range of values from -3 (99% confidence of a cold spot), -2 (95% confidence of a cold spot) -1 (90% confidence of a cold spot), 0 (no significant change), 1 (90% confidence of a hotspot), 2 (95% confidence of a hotspot), and 3 (99% confidence of a hotspot).

We first ran an EHA on individual input Indicator variables according to annual and seasonal (winter, spring, summer, autumn) periods. As a final step we applied a multivariate hotspot ranking based on Thermal, Wetness, and Vegetation change scenario themes (see Table 2). The change themes reflect landscape changes considered to be detrimental (e.g., a threat) to ecosystems and human populations. We selected AT (increasing), NFS (increasing), and ALT (increasing) for the Thermal multivariate ranking; PPT (decreasing), VPD (increasing) and SM (decreasing) were selected for the Moisture multivariate ranking; NDVI (decreasing) and VOD (decreasing) were used for the vegetation ranking. While we acknowledge that in some low-lying regions (e.g., the Alaska Yukon-Kuskokwim Delta) an increase in PPT may be detrimental if it contributes to local flooding, here we selected "decreasing PPT" as having an undesired impact on the region because of overall influences on drought and ecosystem susceptibility to fire.

For the ranking scheme, we assigned a score of "1" to pixels where only an individual Indicator showed a hotspot according to the selected change scenarios. A score of "2" was assigned to pixels when two Indicators showed hotspots of change. A score of "3" was assigned to pixels where three Indicators showed hotspots of change.

2.3. Fire disturbance assessment

To evaluate how trends in individual indicators were related to wildfires we used GFED4s, which documents burned area from 1997–2016. To determine the historical status of fire for each grid cell, we first calculated the sum of the historical burned area. We then grouped grid cells into low, medium and high fire-affected classes based on three identified quantiles. Low was classified as grid cells having burned areas of >0-0.80 km^2; medium was burned areas of 0.81-5.65 km^2; high was burned area of 5.66-343 km^2. We then evaluated the co-occurrence of the burned area classes with grid cells having identified significant trends.

3. Annual and Seasonal Trend Assessment Results

The annual regional Theil-Sen trends for Indicators over the 1959–2020, 1980–2020, and 1997–2020 periods are provided in *SI Table 3* . The regional trends for the winter season are provided in *SI Table 4* . These include seasonally averaged AT (°C), total days having non-frozen surface conditions (NF; number of days per season), total PPT (m), total snow-covered area (SC; km^2), and average VPD (kPa). Regional spring Indicator trends are provided in *SI Table 5* ; summer trends are in *SI Table 6* ; autumn trends are in*SI Table 7* . Spring and autumn Indicators include average AT, total NF days, total PPT, total SC area, average SM, VPD, NDVI, VOD. Summer trends include AT, total NF days, total PPT, average SM, VPD, NDVI, VOD.

SI Figure 3 shows the Indicator time series for the FD, and boreal and tundra sub-regions. See Figure 1 in the main manuscript for time series according to NA and EA sub-regions.

SI Figures 4, 5, and 6 show the per-pixel trend maps for *Thermal* ,*Moisture* and *Vegetation* Indicators. SI Figure 7 provides a summary of the annual trend results according to continuous, discontinuous, and sporadic/isolated permafrost classes (see Figure 2 in the main manuscript for trend summaries according to vegetation type).

Maps showing the seasonal Theil-Sen trends, on a per-pixel basis, are provided in SI Figure 10 (winter); SI Figure 11 (spring); SI Figure 12 (summer); SI Figure 13 (autumn).

Associated figures indicating the percent of region impacted by a seasonal change in Indicator status, according to boreal forest, boreal wetland, boreal non-forest (i.e., non-forest and non-wetland shrubland and/or grassland), and tundra within Eurasia or North America are as follows: SI Figure 14 (winter); SI Figure 15 (spring); SI Figure 16 (summer); SI Figure 17 (autumn).

An overview of the regional and pixel-based Theil-Sen trend results is provided below.

4.1 Thermal Trends

4.1.1. Near-surface air temperature (AT)

Based on the regional trend analysis, the full domain experienced significant increases in annual AT over the 1959–2020 and 1980–2020 periods (*SI Table 3* ; also see Figure 1 and SI Figure 3). More recently, from 1997–2020, only EA showed significant, annual,*regional* warming, with median rates of 1.12 °C dec^{-1} in the tundra zone and 0.57 °C dec^{-1} in the boreal. The most substantial warming (approaching 1.7 °C dec^{-1}) occurred in the far eastern Siberian tundra and throughout central Siberia spanning from the Yamal and Taymyr Peninsulas south towards Krasnoyarsk and Lake Baikal (SI Figure 4b). On a per-pixel basis, ~99% of the Eurasian tundra region experienced significant warming (see Figure 2 EA-a), as did 72% of the Eurasian boreal forests, 92% of the Eurasian boreal wetlands, and 83% of the Eurasian grassland/shrublands.

During the 1997–2020 time period a slight neutral to cooling phase in Canada resulted in non-significant annual AT trends over NA tundra and boreal regions. However, the local per-pixel based trend assessments indicated significant warming (0.08-0.18 °C dec^{-1}) over the Alaska Seward Peninsula and North Slope, and the Canadian Mackenzie River Delta (SI Figure 4-b). This warming contributed to 19% of the tundra pixels in North America having significant increase in annual AT (Figure 2 NA-a), compared to only 1.3% of boreal forest, 8.2% of boreal wetlands, and 6% of grass/shrub.

All domains showed substantial regionally-based warming in winter (December-February) and spring (March-May) over the full 1959–2020 period in the regional-based trend assessment. For 1980–2020 the EA tundra zone and NA boreal and tundra zones had significant increases in winter AT (*SI Table 4*). Over 1997–2020 only the EA and EA tundra zones showed a significant increase in winter AT (for EA tundra, this was a quite substantial 2.16 °C dec^{-1}). However, the pixel-based trend assessment also indicated significant local increases in winter AT in the northern EA boreal and the NA Seward Peninsula, North Slope and northern Mackenzie River Delta (SI Figure 10-b). Over the 1980–2020 spring seasons (*SI Table 5*) the EA tundra and boreal zones (0.95 and 0.66 °C dec^{-1}), and the NA tundra (0.46 °C dec^{-1}), showed significant regional rates of warming. More recently (1997–2020) significant regional spring warming occurred in the EA tundra and boreal (1.75 and 0.96 °C dec^{-1}). The NA regions were not significant, however the pixel-based trends showed a few areas of localized warming over the northern Alaska and far western Canadian coastal tundra (SI Figure 11), whereas local cooling was observed in southern boreal Quebec.

Summaries of per-pixel AT trends according to vegetation classes (i.e., tundra, boreal forest, boreal wetland, and boreal grass/shrub) are shown in SI Figure 15 (winter), SI Figure 16 (spring), SI Figure 17 (summer), and SI Figure 18 (autumn).

Regional trend assessments for summer AT showed significant increases across the FD over 1959–2020 and 1980–2020 (*SI Table 6*). For 1997–2020 all regions, except the NA boreal, had a significant increase in summer AT. Based on the regional trend assessment, the most substantial increases in AT occurred in the EA tundra (0.77 °C dec^{-1}). However, a different story emerged from the per-pixel trend assessments (SI Figure 12-b), which showed more localized regional warming during the 1997–2020 period over a portion of central Siberia (Yamal and Taymyr Peninsulas stretching south towards Lake Baikal), far eastern Siberia, the Alaska Seward Peninsula, northern Greenland and Ellesmere Island.

Similar to the summer period, the regional trend assessments showed significant increases in autumn AT over the full domain from 1959–2020 and 1980–2020 (*SI Table 7*). Over the 1997–2020 period only the EA tundra zone showed a significant trend, an increase in AT of 1.27 °C dec^{-1}. The per-pixel trend map for the same time period (SI Figure 13-b) primarily agrees with the regional trend assessment, with widespread warming occurring across the EA tundra zone. However, the per-pixel assessments showed autumn EA warming trends spanning the tundra yet also extending southward into the northern boreal. In far eastern Siberia, significant autumn warming based on the per-pixel assessments was also observed north of China near the Stanovoy Range. In NA, the majority of Alaska showed significant autumn warming, with the most severe warming rates occurring within the North Slope (0.21 °C dec^{-1}).

4.1.2. Surface non-frozen (NF) season

The regional trend assessment showed significant increases in annual NF days for the EA tundra and boreal domains over the 1980–2020 and 1997–2020 periods (*SI Table 3*). For 1997–2020 the largest increase was observed over the EA tundra (4.2 days dec^{-1}); the NA tundra domain also had a significant increase (3.97 days dec^{-1}). The per-pixel assessments indicate more localized regions of increase in the annual NF season (Figure 2; (SI Figure 4-d). In EA approximately 17% of the tundra region, 11% of boreal forests, 10.4% of boreal wetland, and 9.9% of boreal shrub/grassland pixels had significant increase in annual NF days. In NA 9.7% of the tundra, 4% of boreal forest, 3.7% of boreal wetland, and 9% of boreal grass/shrub pixels experienced a significant increase in the number of annual NF days. The positive per-pixel trends primarily occurred within portions of central and southern Alaska, western Canada, and central and eastern Siberia (including the Chersky Range, the Chukchi and Kamchatka Peninsulas), ranging from 0.69 to 0.98 days dec^{-1}. In contrast, local regions within eastern Canada and south-central Siberia had a decrease in the annual non-frozen season.

Significant regional increases in winter NF days were only observed over the shorter 1997–2020 period, for the EA, EA Tundra, EA Boreal and NA regions (*SI Table 4*). Local changes in pixel-based winter NF were minimal, but western Russia did show increases in the non-frozen season days (SI Figure 10; SI Figure 15). Although both the EA tundra and boreal regions showed significant increases in spring NF days from 1980–2020 (0.7 and 2.08 days dec^{-1}), over 1997–2020 only the EA boreal was significant (1.42 days dec^{-1}). The per-pixel trends for 1980–2020 (SI Figure 11-c) showed widespread increases in spring NF days across much of Eurasia, portions of Alaska, and far western Canada. However, over the 1997–2020 period, trends were no longer observed over a majority of the domain (SI Figure 16-b). Remaining trends in spring NF days were primarily located in the south-central Siberian boreal (north of Kazakhstan and western Mongolia), within localized areas in the western Canadian tundra, in the southwestern Canadian boreal (British Columbia), and over the Alaska Seward Peninsula. For the autumn, the regional analysis showed a significant increase in NF days for the NA boreal over the 1997–2020 period (3.44 days dec^{-1}; *SI Table 7*). However, the per-pixel trends revealed substantial increases (0.44 to 1.21 days dec^{-1}) in NF days across much of the EA northern boreal and tundra, and within Interior to Southern Alaska (SI Figure 13-d; SI Figure 18).

4.1.3. Permafrost active layer thickness (ALT)

The ALT is provided on an annual basis. Because of this, only annual changes in ALT are discussed here. According to the regional trend assessments (*SI Table 3*), all domains had a significant increase in annual ALT over the available product time period (1997–2020) with regional median rates of ranging from 0.06 m dec^{-1} to 0.1 m dec^{-1}. We found that in EA 72% of tundra, 54% of boreal forest, 67% of boreal wetland, and 56% of boreal grass/shrub had a significant increase in ALT (Figure 2). For NA 24% of tundra, 66% of boreal forest, 49% of boreal wetland, and 50% of boreal grass/shrub pixels had a significant increase in

ALT. The pixel-based trends show a majority of the ALT increase occurring across Siberia (tundra and boreal), Alaska, and western Canada. As mentioned earlier (SI Section 1.1), the ALT product has known problems underestimating magnitudes of change in annual thaw. Given this problem we use the trend results to identify the regions having change in ALT, while assuming that the identified rates of change are largely underestimating actual changes in depths of ground thaw.

4.2 Moisture Trends

4.2.1 Precipitation (PPT)

The regional trend assessments showed increases in annual PPT over the 1959–2020 (0.13 to 0.21 m dec^{-1}), 1980–2020 (0.12 to 0.31 m dec^{-1}) and 1997–2020 periods (0.3 to 0.76 m dec^{-1}), except for the EA boreal zone which did not show significant trends in any period, and the NA boreal zone which did not show a significant regional trend over the 1997–2020 period (*SI Table 3*). The most substantial regional increases were observed in 1997–2020 for the EA Tundra region, at 0.76 m dec^{-1}. Although the NA boreal region had increasing regional PPT trends over the first two time periods, it did not show a significant trend for 1997–2020.

As seen in the per-pixel trend results (SI Figure 5-b), the patterns of change in annual PPT are spatially complex. Over the 1997–2020 period, in EA PPT increased over 19.8% of the tundra, ˜8% of boreal wetland, and 3 and 1.4 % for boreal grass/shrub and forest pixels. Whereas PPT decreased over 5.7% of boreal forests and 3% of boreal grass/shrub pixels in EA. In NA, 4.8% tundra, 7% of boreal forest, 10.5% boreal wetland, and 9.9% of boreal grass/shrub pixels had an increase in annual PPT. Compared to a decreasing PPT within 1.5% of NA tundra and <1% for the other NA vegetation categories. Locally, PPT decreased over portions of central Siberia (primarily in the boreal) while clusters of PPT increase were observed across portions of the northern EA tundra region, especially in far eastern Siberia (i.e., the Kolyma Range towards the Chukchi Peninsula). Increases in PPT occurred within the more central to southern portions of Alaska, including the Yukon-Kuskokwim Delta. In Canada, increasing annual PPT occurred in the Mackenzie River Delta, in portions of southern boreal British Columbia, and southern boreal Quebec.

Regional trends in winter PPT were not observed over the 1959–2020 and 1980–2020 time periods. However, in the 1997–2020 time series the EA tundra and NA boreal both had significant increases in PPT of 0.34 and 0.15 m dec^{-1} (*SI Table 4*). The per-pixel trends (SI Figure 10-f) primarily show small, localized increases in winter PPT in portions of central and far eastern Siberia (also see SI Figure 15). No significant regional changes in PPT were observed for the spring and summer seasons over the 1997–2020 period (*SI Tables 5, 6*). Patterns of change in the spring per-pixel trend map (SI Figure 11-f) included slight, local, increases in PPT in the western Siberian boreal, and small local decreases in central Canada, however made up a very small portion of the regional domains (SI Figure 16). The summer per-pixel trends (SI Figure 12-d) indicated decreasing PPT in the southcentral Siberian boreal region (south of the Siberian Plateau), and localized areas of increasing PPT in some places including the Mackenzie River Delta in Canada. Also see SI Figure 17. Over the autumn period (*SI Table 7*) the NA tundra region experienced a significant increase in PPT over all three time periods (0.06, 0.08, 0.2 m dec^{-1}, respectfully). Increases in PPT over the EA tundra region were observed for the 1980–2020 and 1997–2020 periods (0.14 and 0.29 m dec^{-1}). The autumn pixel-based trends (SI Figure 13-f) did not show large regional changes in PPT, however small clusters of regional increase (SI Figure 18) occurred in boreal southern Scandinavia, southwestern Russia, far eastern Siberia, Interior Alaska, the Alaska Yukon-Kuskokwim Delta, and southern British Columbia.

4.2.2 Snow Cover (SC)

Significant region-wide trends in winter SC were not observed over the 1997–2020 period (*SI Table 4*), however the EA tundra and boreal regions showed a decrease in total snow cover from 1959–2020 and 1980–2020. In EA (Figure 2; SI Figure 15) only 0.5% of the tundra, 2.4% of boreal forests, 1.3% of boreal wetlands, and 1.9% boreal grass/shrubland had pixels with a significant decrease in SC and very few (0.02-0.26%) of the land cover types had pixels with significant increase in SC. In NA, land cover types had very few pixels with increasing SC (0.1-0.8%) or decreasing (0.12-0.8%) SC. Only one area of significant change in winter

SC was observed in the per-pixel based trend maps (an increase of ~ 5 x 10^4km^2 dec^{-1} east of Lake Baikal; SI Figure 10-i, -j).

The regional assessments showed a significant decline in total spring SC across all regions, from 1959–2020 (*SI Table 5*). During 1980–2020 only the EA tundra and boreal zones had significant declines in total spring SC, and for 1997–2020 only the EA boreal zone showed a decline in SC (-23.8 x 10^4 km^2). The per-pixel trend maps (SI Figure 11-g, -h) indicate that most of areas of decreasing spring SC were within southern boreal Siberia, although the total area impacted was very small (SI Figure 16). The regional trend results showed most of the high latitude region to also be impacted by declines in autumn SC (*SI Table 7*) over the 1959–2020 and 1980–2020 periods, except for the NA boreal zone. Though, for the 1997–2020 period only the EA tundra had a significant regional decline in SC (-17.99 x 10^4 km^2). As with the spring SC trends, the autumn decline in SC was primarily observed in the southern Siberian boreal zone (SI Figure 13-h). However, some areas of boreal NA did show a significant increase in autumn SC (SI Figure 18).

4.2.3 Vapor Pressure Deficit (VPD)

Widespread regional increases in annual average VPD were observed over the 1959–2020 period (*SI Table 3*). For 1997–2020 significant regional increases in annual VPD occurred in the EA tundra and boreal (0.02 and 0.01 kPa dec^{-1}), and in the NA tundra (0.01 kPa dec^{-1}). The per-pixel results showed that, for EA, 67% of the tundra, 19% boreal forest, 37% boreal wetland, and 50% boreal grass/shrub pixels had a significant increase in VPD (Figure 2). In contrast, over NA the number of pixels having an increase in annual VOD were relatively similar across vegetation classes (6-10% of total pixels) and each NA boreal vegetation class also show some pixels with a VPD decrease (5.5-6% of total pixels). Local pixel trends (SI Figure 5-f) showed much of the increase occurring across northern to central Siberia, and over portions of Interior to northern Alaska, and southwest Canada.

Similar regional patterns of VPD increase were observed in the winter period (*SI Table 4* ; SI Figure 15); locally, the increases in VPD were primarily over Interior and southern Alaska, and northwestern to northcentral Russia (SI Figure 10-h). Regional increases in spring VPD (1997–2020) were only observed for the EA tundra and boreal (*SI Table 5*). The per-pixel maps (SI Figure 11-j) show relatively large increasing trends (up to 0.05 kPa dec-1) over much a majority of Eurasia (SI Figure 16; especially southern Siberia towards northern Mongolia and China), much of southern Alaska, and western Canada. The regional summer trends (*SI Table 6*) show increasing VPD over EA tundra and boreal zones, and the NA tundra. The per-pixel trends (SI Figure 12-f) show substantial increases in summer VPD within the West Siberian Plain and the Central Siberian Plateau, which are also reflected in the larger number of pixels having a significant positive trend in the EA tundra (SI Figure 17). For the 1997–2020 regional autumn trends (*SI Table 7*) only the NA boreal had a significant increase in VPD, and the pixel-based trends (SI Figure 13-j) showed local increases in VPD primarily in local areas across eastern Siberia, western Canada, and the Alaska Seward Peninsula (also see SI Figure 18).

4.2.4 Soil Moisture (SM)

Significant regional changes in annual non-frozen season SM were not observed over the most recent 1997–2020 period (*SI Table 3*). However, over the longer term, regional SM drying was observed for the EA boreal (1959–2020 and 1980–2020) and SM wetting was observed for the NA tundra (1959–2020 only). In EA, approximately 1.2% of tundra, 12% of boreal forest, 4% boreal wetland, and 6.7% of boreal grass/shrub pixels showed a significant decrease in SM. Whereas ~ 1.5% of pixels showed drying in each of the boreal vegetation classes, compared to 5.4% in the tundra class. In NA, 3.3% of tundra, 1.7% forest, and 1.4% boreal grass/shrub pixels showed significant drying; 1.5% of tundra, 2.8% boreal forest, 5.4% boreal wetland and 4.8% boreal grass/shrub pixels had a significant non-frozen season increase in SM.

The per-pixel assessments indicate that most of the recent SM drying occurred in the central Siberian boreal (SI Figure 5-h); localized areas of annual SM increase include the Mackenzie River Delta. For the spring period, only the EA tundra region showed a significant change (increase; 0.004 cm^3 cm^{-3}dec^{-1}) over the 1997–2020 period (*SI Table 5*), which was primarily driven by local areas in the east Siberian tundra (SI

Figure 11-l; SI Figure 16). However, increasing spring SM was also observed locally in the Mackenzie River Delta. For the same period, per-pixel based decreases in spring SM were observed in the southern Siberian boreal and in localized areas of the western Canadian boreal. For summer, the only significant regional trend was a decrease in SM over the EA boreal (-0.007 cm^3 $cm^{-3}dec^{-1}$; *SI Table 6*). The pixel-based trends (SI Figure 12-h) showed this decrease in summer SM occurring primarily within the Siberian Central Plateau. Also see SI Figure 17. Significant regional trends in autumn SM were not observed for the 1997–2020 period (*SI Table 7*) through the per-pixel trends (SI Figure 13-l) indicate local patterns of SM decrease in central Siberia, substantial wetting within the Mackenzie River Delta, and more minimal wetting within the Alaska North Slope, local areas in the Yukon-Kuskokwim Delta, and portions of far eastern Siberia. Also see SI Figure 18.

4.2.5 Fraction of Surface Water (FW)

The regional trend assessments indicated that the annual non-frozen season FW coverage (i.e., surface water inundation) increased within the EA tundra and boreal regions (over 2003-2020; 0.44 and 0.19%, respectfully), with no significant change detected for the NA regions (*SI Table 3*). However, the per-pixel trends revealed that in EA 20% of the tundra, 42% of the boreal forest, 37% of boreal wetland and 37% of boreal grass/shrub domains experienced an increase in FW (Figure 2) and relatively few pixels (<3%) showed significant FW drying. Similar wetting occurred in NA, with an increase in FW observed 21% of tundra, 28% of boreal forest, 26% of boreal wetland, and 31% boreal grass/shrub pixels. The per-pixel trends (SI Figure 5-i) showed widespread increases in FW throughout the EA tundra and boreal regions, within much of Alaska, central to western Canada, and the Canadian Quebec region. These trends also show a decrease in FW in the Hudson Bay region, and much of southern boreal Ontario. The regional trends show a small increase in spring FW (*SI Table 5*) within the EA boreal and the NA tundra (pixel areas of 0.002 and 0.005% dec^{-1}). Summer regional FW trends also showed increasing surface water coverage in all domains except for the NA tundra (*SI Table 6* ; ˜0.002% dec^{-1}). And in autumn, only the EA tundra and boreal regions had significant changes (increase) in FW (*SI Table 7* ; 0.004 and 0.002% dec^{-1}). The spring, summer, and autumn per-pixel trends (SI Figure 14) indicate widespread, localized increases in FW throughout the high latitude region (SI Figures 16-18). However, the most substantial increases were observed in summer, across much of Canada, southern Alaska (including the Yukon-Kuskokwim Delta) and central to eastern Siberia.

4.3 Vegetation Trends

4.3.1 Normalized Difference Vegetation Index (NDVI)

The regional trend assessment indicated decreasing annual non-frozen season NDVI (i.e., a measure of vegetation greenness) in the EA boreal zone at a rate of -0.009 dec^{-1} from 1988–2020 and ˜ -0.03 dec^{-1} from 1997–2020 (*SI Table 3*).

On a per-pixel basis, in EA ˜14.6% of the tundra, 21.5% of boreal forest, 28% of boreal wetland, and 26% of boreal grass/shrub vegetation types had a significant decrease in NDVI. In contrast, a positive trend (increasing NDVI) occurred across 18.5% of the boreal forest region, compared to 3% of boreal wetlands, 4.5% of boreal grass/shrub and 1.6% of tundra. Similar decreases in NDVI occurred in NA tundra (16%), with much larger decreases observed in the other land cover categories (44% boreal forest, 42% boreal wetland, 40% boreal grass/shrub). Increases in NA NDVI were also small: 5% of boreal forests, 3% boreal wetland, 2.5% boreal grass/shrub, and 1.4% tundra.

For the spring period (*SI Table 5*), only the NA boreal region showed a significant change in NDVI from 1997–2020 (-0.012 dec^{-1}). Whereas over the longer 1988–2020 period, significant increase in NDVI occurred over the EA tundra and boreal (˜ 0.01 dec^{-1}); the only significant regional decrease was observed in the NA boreal (-0.006 dec^{-1}). However, the per-pixel results showed more complex patterns across the high latitude domains (SI Figure 11-n). Much of the southern boreal in EA showed an increase in NDVI, with more substantial trends in southern Finland, western Russia, and the North Siberian Lowland. In NA, the larger increases in spring NDVI occurred in southern boreal British Columbia, and the Northwest Territories.

Meanwhile, decreases in spring NDVI occurred across the Canadian boreal zone, and (to a smaller extent) within Interior Alaska. No regional summer trends were detected for the 1997–2020 period (*SI Tables 6*), through the EA Boreal had a near significant, positive trend (p=0.06). The per-pixel patterns revealed a more complex story (SI Figure 12-j) with summer increases in NDVI occurring in western Russia and throughout portions of Siberia (particularly in far eastern Siberia), and much of Alaska (except for the southern portion), and northwest Canada. Areas of decreasing summer NDVI were found across central Siberia and central to eastern Canada.

For autumn, all regions had a significant decreasing trend in NDVI that was observed over both time periods. However, the per-pixel results (Figure 13-n) show that much of Alaska (except for the southern portion), western and eastern Canada had increases in autumn NDVI, as did northern Siberia, western Russia, and portions of Scandinavia. Decreasing autumn NDVI was found across the central portions of Siberia, and central Canada.

4.3.2 Vegetation Optical Depth (VOD)

No significant regional trends in annual non-frozen season VOD (which is related to biomass water content) were observed during the 1988–2017 and 1997–2017 time periods (*SI Table 3*). However, the per-pixel trends for EA showed a significant VOD increase in 17% of tundra, 13.5% of boreal forest, 21% of boreal wetlands, and 19% of boreal grass/shrub (compared to decreases in 7%, 8%, 5%, and 4% of pixels for the respective vegetation classes). And in NA VOD increases occurred in 27% of tundra, 20% boreal forest, 29% boreal wetland, and 35% of boreal grass/shrub pixels (with respective decreases of 11%, 10%, 6.5% and 4%).

The local increases in VOD (SI Figure 6-d) were scattered over much of the EA and NA regions, especially in Alaska (except in the eastern Interior towards Canada), the southwestern Canadian boreal, the eastern Canadian boreal, eastern and central Siberia, and western Eurasia. The exact ecological signal reflected by the increase in VOD is unknown, although most likely indicates an increase in aboveground biomass (and hence, an increase in biomass water content). Local areas having a decrease in annual non-frozen season VOD included the far southern Siberian boreal, the West Siberian Plain, and southern boreal Saskatchewan and Manitoba. Time series where an abrupt, sharp, and persistent decrease in VOD has occurred most likely indicate a removal of live biomass (e.g., severe plant mortality or removal via fire or logging) whereas gradual declines are more likely indicating plant stress (e.g., from drought) and possibly mortality (through less severe impacts on the plant community).

The regional assessment showed all domains having a significant increase in spring VOD for the 1997–2017 period (*SI Table 5*). The per-pixel trends for spring (SI Figure 11-p) show patterns of increasing VOD over much of the region (SI Figure 16), except for the southern Siberian boreal zone. Regional trends were not observed for summer in the 1997-2017 period, but in autumn there were significant trends in the EA Tundra. (*SI Tables 6, 7*). However mixed patterns of VOD change in summer were observed across the domain (SI Figure 12-l) with increasing VOD trends observed in boreal western Russia, eastern Russia, and much of Alaska except for the Interior which had decreasing summer VOD. Other areas of VOD decrease included much of Canada and central to southern Siberia. See SI Figure 17 for a summary of pixel-based trends according to vegetation classes in EA and NA. The regional pixel-based patterns in summer are similar those observed over the autumn period (SI Figure 13-p).

4.3.3 Vegetation tree cover (TC) and non-TC (NTC) status

Regional increases in TC were observed over the 1997–2017 period for the EA boreal and tundra zones (1.5 and 3% dec^{-1}), and in the NA boreal (1.9% dec^{-1}; *SI Table 3*). An increase in TC within the NA tundra (0.49% dec^{-1}) was only observed over the longer 1988–2017 period. Based on the per-pixel trends, an increase in annual TC occurred in over most of the high latitude region, especially in the Mackenzie River Delta region, eastern Canada, and western Europe/Russia. For NTC, the only significant regional trend for 1997–2017 was an increase observed in the NA tundra (0.49% dec^{-1}), whereas the per-pixel trends show decreases in NTC (SI Figure 6-f). Over the 1988–2017 period, NTC was observed to decrease in the EA boreal (-1.44% dec^{-1}). As the observed changes in TC and NTC were not very substantial, we focus instead on the other vegetation Indicators for purposes of ecosystem change and vulnerability assessments.

5. Regional Trend Summaries Associated with Permafrost & Fire Disturbance

5.1 Permafrost class

See SI Figure 7. The associated regional trends are summarized here.

According to the per-pixel based trends, we found that over the 1997–2020 period, 93% of the EA continuous permafrost zone was impacted by significant increases in annual average AT, compared to 79% in the EA discontinuous zone, and 55% of the EA sporadic/isolated zone (SI Figure 7). In contrast, only ~19% of the NA continuous permafrost zone was impacted by significant increases in annual AT, and only ~6% of the discontinuous zone and 1% of the sporadic/isolated zone had significant increases in AT.

Approximately 11% of the full EA permafrost zone experienced a significant increase in annual NFS. This was observed across 14%, 6.6%, and 8.5% of the EA continuous, discontinuous, and sporadic/isolated zones, respectively. In NA, 4.5% of the full permafrost zone had a significant increase in the annual NFS. This included 7.5% of the continuous zone, 6.9% of the discontinuous zone, and 7% of the sporadic/isolated zone. ~2.8% of the NA permafrost region showed a decrease in the NFS.

Over 60% of the Arctic-boreal permafrost region had an increase in annual ALT, with less than 1% having a significant decrease in ALT. For the EA region, 64% of the continuous zone had a significant increase in ALT, followed by 51% in the discontinuous zone, and 41% in the sporadic/isolated zone. Approximately 33% of NA region had an increase in annual ALT; 26% of the continuous zone; 54% of the discontinuous zone; 33% of the sporadic/isolated zone. For both EA and NA regions, we recognize that tracking deeper ALT changes in the more degraded discontinuous and sporadic/isolated zones using model-based approaches is often much more difficult relative to the continuous zone where ALT is relatively shallow. Because of this, it is likely that ALT increase (deepening) is severely underestimated for the discontinuous and sporadic/isolated zones.

The percentage of the permafrost region impacted by significant increases or decreases in annual PPT was minimal (6% and 3%, respectively). In EA, 9% of the continuous zone, 3% of the discontinuous zone, and 1% of the sporadic/isolated zone had a significant increase in PPT. Whereas 6% of the EA sporadic/isolated zone had a significant decrease in PPT; 2% and 1% in the respective discontinuous and continuous zones. Only 6% of the NA permafrost region had significant increase in annual PPT (less than 1% had a significant decrease); 6% of the continuous zone; 8% of the discontinuous zone; 3% of the sporadic/isolated zone.

In EA, ~54% of the continuous zone experienced an increase in annual VPD, compared to 21% of pixels in the discontinuous and 10% of pixels in the sporadic/isolated zones. Very few pixels (<1%) in each permafrost region had a significant decrease in VPD. The increase in VPD was less prevalent in NA, encompassing only 6.8% of pixels in the continuous domain, 11% in the discontinuous, and 5% in the sporadic/isolated domain. In the sporadic/isolated zone, 8% of pixels had a decrease in VPD (compared to <1% of pixels in the other permafrost zones).

For FW within the EA region 31% of pixels in the continuous, 35% of the discontinuous, and 40% in the sporadic/isolated zones had a significant increase; less than 2% of pixels per zone had a significant decrease in FW. In NA, 24% of pixels in the continuous, ~30% in the discontinuous, and 26% in the sporadic/isolated zone had an increase in FW, compared to respective decreases of 4%, 2.6%, and 4%. For non-frozen season SM, 7% of the EA permafrost had significant decrease (11% sporadic/isolated, 6% discontinuous, 5% continuous), while 3% had a significant increase (~2-3% across categories). In NA, ~3% of the permafrost domain had a significant increase in SM (2.6% continuous, ~1% sporadic/isolated and discontinuous, and ~2% had a significant decrease (3.6% continuous, ~2% discontinuous and sporadic/isolated).

For vegetation trends, in EA 32% of pixels in the continuous zone, 35% of the discontinuous zone, and 24% of the sporadic/isolated zone had a significant decrease in non-frozen season NDVI. Whereas only a small percentage had a significant increase in NDVI (1%, 2.4% and 4.4% respectfully). In NA, 15% of pixels in the continuous zone had a decrease in NDVI; 19% in the discontinuous zone, and 34% in the sporadic/isolated zone. Increase in NDVI in NA was slightly higher relative to EA: 6.4% continuous, 7.3% discontinuous, 3% sporadic/isolated.

For VOD, in EA 19% of the continuous zone, 14% of the discontinuous zone, and 11% of the sporadic/isolated zone had a significant increase. Whereas 5%, 8.5% and 11% had a significant decrease. The amount of increase was higher in NA, at 22.6% (continuous), 30.5% (discontinuous), and 33% (sporadic/isolated). Over the same period a decrease in VOD was observed for 11% of pixels in the NA continuous zone, 4.8% in the discontinuous zone, and 4.9% in the sporadic/isolated zone.

5.2 Fire disturbance

SI Figure 8 shows the spatial patterns of wildfire disturbance across the domain for two periods, 1997–2006 and 1997–2016 (GFED4s burned area through 2020 was not available at the time of this assessment). The maps show much of the fire activity occurring within Interior Alaska, boreal Canada, and boreal Siberia.

The associated SI Figure 9 indicates the percentage of pixels for each Indicator having a significant positive or negative trend as impacted by wildfire activity according to three categories of disturbance (i.e., minimum, moderate, large). These results are summarized as follows:

In EA we found that 33%, 35% and 50% of the pixels showing significant increase in annual AT have been influenced by wildfire in the minimum, moderate and large categories respectively. In contrast, we found that 50%, 0% and 50% of the pixels showing significant decreases in AT have been impacted by wildfire in the minimum, moderate, and large categories respectively. Winter snow has been significantly decreasing by 27%, 24% and 50% of the pixels in the minimum, moderate and large categories, while it has been increasing by 35%, 31% and 34% of the pixels in the same categories. For SM we found that 45%, 37% and 17% of the pixels show a significant increase in the minimum, moderate and large classes, while it has been decreasing by 14%, 37% and 48% of the pixels in the same classes. For NDVI, 50%, 29% and 21% of the pixels are increasing in the minimum, moderate and large categories while 25%, 36% and 40% of the pixels are decreasing. For VOD, 23%, 40% and 37% of the pixels are increasing in the minimum, moderate and large categories while 34%, 38% and 28% of the pixels are decreasing (SI Figure 9).

In NA, we found that 31%, 42% and 28% of the pixels showing significant increase in annual AT have been impacted by recent wildfire in the minimum, moderate and large categories respectively. In contrast, we found that 36%, 64% and 0% of the pixels showing significant decreases in AT have been impacted by wildfire in the minimum, moderate, and large categories respectively. Winter snow has been significant decreasing by 30%, 7% and 63% of the pixels in the minimum, moderate and large categories, while it has been increasing by 36%, 62% and 3% of the pixels in the same categories. For SM we found that 55%, 28% and 17% of the pixels show a significant increase in the minimum, moderate and large classes, while it has been decreasing by 43%, 27% and 27% of the pixels in the same classes. For NDVI, 28%, 32% and 40% of the pixels are increasing in the minimum, moderate and large categories while 33%, 25% and 42% of the pixels are decreasing. For VOD, 40%, 27% and 33% of the pixels are increasing in the minimum, moderate and large categories while 36%, 33% and 31% of the pixels are decreasing (SI Figure 9).

Although lessening cold temperature and frozen soil constraints are likely contributing to areas of NDVI increase across the high latitude domain (Kim et al., 2012; Keenan & Riley, 2018), a recent study of Landsat-based NDVI trends over Alaska and northwest Canada reported that many of the pixels having strong NDVI trends were related to changes in land cover, often following a disturbance. For example, if logging or wildfire occurred earlier in the time series, the resulting trend was often positive, reflecting NDVI recovery. In contrast, a disturbance later in the record often produced a negative trend. Similar patterns related to NDVI and disturbance have been reported elsewhere (e.g., Jones et al., 2013).

6. Annual and Seasonal Univariate Change Spot Assessments

As mentioned previously (SI Section 2.2.2), unlike the Theil-Sen approach which allows for tests of significance, the Getis-Ord Gi* hot spot analysis relies on spatial neighborhood relationships. To be a statistically significant hot (positive change) or cold (negative change) a given pixel must have a substantial change value, and also be surrounded by other pixels having a substantial change value with the same change sign. The change spots shown in this assessment indicate where the identified change is much larger than random chance (confidence intervals > 90%). The location of identified "spots" may not always align with the identified pixels where a significant change was detected using the Theil-Sen metrics, though in most cases the spatial patterns are similar, yet with a larger area identified as a "change spot" through Getis-Ord Gi*. Getis-Ord Gi* does not provide indication of the rate of change.

For the univariate and multivariate change results we focus the term "hot spots" as areas having an "undesired" change direction in a specified Indicator.

For discussion of rates, please refer to the previous sections.

The SI figures showing the Getis-Ord Gi* change spots are as follows:

SI Figure 19 shows maps of change spots for the Indicators over annual time steps (1997–2020).

SI Figures 20, 21, 22, 23 show maps of change spots for the Indicators over seasonal (winter, spring, summer, autumn) time steps.

SI Figure 24 summarizes the annual Indicator change spot occurrences according to vegetation class (for EA and NA).

SI Figures 25, 26, 27, 28 summarize the seasonal Indicator change spot occurrences according to vegetation class (for EA and NA).

SI Figure 19 summarizes annual Indicator change spot occurrences according to permafrost type.

6.1 Thermal change spots

The annual AT change spot results for 1997–2020 (SI Figure 19-a) are similar to the significant trends detected through the Thiel-Sen approach (SI Figure 4), and show most of the recent (and severe) high latitude warming occurring across Eurasia. The pixel-based results for the EA region indicated that 99% of tundra, 94% of boreal wetlands, 83% of boreal grass/shrub and 77% of boreal forest coincided with a hotspot of increase in annual AT (SI Figure 24). The hot spot assessment also showed severe warming within the North Slope of Alaska, the Mackenzie River Delta in Canada, and moderate severity within portions of Interior Alaska and the Yukon-Kuskokwim Delta. The winter assessment (SI Figure 20) results show that much of the increase in AT occurred across northern EA, some portions of southern Siberia (bordering China), the North Slope of Alaska, southern Alaska including the Yukon-Kuskokwim Delta, and a swath of western Canada including the Mackenzie River Delta (which were not detected in the Theil-Sen assessment). Spring hot spots (SI Figure 21) were widespread across all of Scandinavia, western Russia, and much of Siberia, western Canada and Alaska (with the exception of the southern North Slope and southern Alaska). In summer (SI Figure 22), the AT hot spots were over much of central and far eastern Siberia, central Alaska (including the Interior and Seward Peninsula), and portions of the Canadian southern boreal. Autumn AT (SI Figure 23) hot spots were primarily across northern portions of EA, central and western portions of Alaska, and southern British Columbia.

As seen with the Theil-Sen results, change in annual surface NFS was more spatially variable (SI Figure 19-b) with localized hot spots (i.e., increases in the length of NFS) occurring in portions of western Russia (e.g., Karelia), Siberia, the Seward Peninsula of Alaska, and western Canada. Whereas cold spots (decrease in the NFS) were also observed, spanning central to eastern Canada, southern Siberia, western Russia and Scandinavia. In Eurasia (SI Figure 24), boreal forest (11% of the vegetation type) and boreal grass/shrub (14%) were the primary land cover types coinciding with a decrease in annual NFS. Whereas 12% of the EA tundra class experienced an increase in NFS. In NA, 15.5% of the tundra, 12% of the boreal forest, 22.5% of boreal wetlands, and 12% of boreal grass/shrub coincided with a decrease in the annual surface NFS. Seasonally, notable changes in the winter NF period was an increase in the NF period (cold spot) in boreal Quebec and south of the Hudson Bay. This general area also had NF period cold spots in spring, and a few local regions of spring NF season hot spots (increase in NF period) were observed across the portions of Siberia, southern Finland, northern Alaska, and British Columbia. In autumn, bands of NF season hot spots occurred across Scandinavia, western Russia, central and southern Alaska, and Canada.

The hot spot assessment revealed stronger patterns of increase in ALT (SI Figure 19-c) relative to the trend results (SI Figure 4). Similar to the trend analysis, much of Siberia showed an increase in ALT, as with Alaska and western Canada. However, the hot spot results also highlight increases in ALT extending into central Canada, and local areas in eastern Canada. Overall in EA (SI Figure 24), 81% of tundra, 77% of boreal forest, 75% of boreal wetlands, and 74.5% of boreal grass/shrub pixels coincided with an ALT hotspot. In NA this was 26%, 72%, 60%, and 63.5% respectfully.

6.2 Moisture change spots

Substantial differences in spatial patterns for annual PPT were observed between the Getis-Ord Gi* and Theil-Sen approaches. While the Thiel-Sen results (SI Figure 5) showing significant trend were perhaps more conservative, a larger area of annual PPT hot spots (decreasing PPT) were detected, primarily across central Siberia, and in Canada (SI Figure 19). Areas of more localized cold spots (increasing annual PPT) were identified in eastern Siberia, southern Alaska (including the Yukon-Kuskokwim Delta), the Mackenzie River Delta, and southern Quebec, Canada. By vegetation class (SI Figure 24), in EA 45% of the tundra, 14.5% of boreal forest, 29% of boreal wetlands, and 13% of boreal grass/shrub coincided with a PPT cold spot (increase in PPT), compared to 0.3%, 29%, 9.5%, and 24% coinciding with a PPT hot spot (decrease in PPT). In NA, 14.5%, 19%, 28%, and 28% of vegetation class pixels, respectfully, coincided with a cold spot and 12.5%, 9%, 4% and 4% coincided with a hot spot.

The Getis-Ord Gi analysis also picked up more localized regions of change in annual SC (SI Figure 19), with portions of southern boreal Siberia, and southern boreal Canada showing decreases in SC (hotspots) whereas Scandinavia and Interior Alaska showed increases in annual SC (cold spots). Overall, in EA, 7% of the boreal forest, 5.7% of boreal wetlands, 2.4% of boreal grass/shrub, and 1% of tundra coincided with a cold spot, compared to 2.6%, 4.4%, 2.9%, and 1.3% in NA, respectively. Regarding hot spots in EA (NA), the boreal forest domain was 10% (20.7%), boreal wetlands were 1.8% (5.5%), boreal grass/shrub were 4.3% (6.2%), and tundra was 0.2% (0.3%)

The identified change spots for annual VPD show somewhat similar spatial patterns to those observed in the Theil-Sen trend results, with VPD hot spots (increasing VOD; SI Figure 19) shown over Interior and portions of northern Alaska, western Canada, and Siberia. However, a much larger portion of Russia is revealed to have a substantial increase in VPD relative to what was shown in the Theil-Sen results. Overall, in EA 94% of tundra, 83-84% of boreal forest, wetland and grass/shrub pixels coincided with identified VPD hot spots (SI Figure 24). In NA, this was 29.5%, 39.5%, 41%, and 51.5% respectfully. Of note are the localized VPD cold spots in southern (boreal) British Columbia and northern Quebec. Substantial increases in winter VOD (SI Figure 20; hot spots) include western Russia, northern Siberia, southern Alaska, the North Slope of Alaska, and western Canada. Spring hot spots of VPD included Scandinavia, Siberia (except for the far east), central and southern Alaska, and western Canada. Summer (SI Figure 22) showed mixed hot spot and cold spot occurrences spatially, with substantial regional hot spots over western Russia, portions of central and eastern Siberia, and Alaska (except for the Interior). VPD hot spots in autumn (SI Figure 23) were over much of Interior Alaska, British Columbia, and portions of Siberia and far eastern Russia. Scandinavia, in contrast, was a VPD cold spot.

Hot spots in annual SM (i.e., decreasing SM) were identified over much of central Siberia, a small portion of western Siberia, and portions of Canada and Interior Alaska (SI Figure 19), spanning a larger geographic area than had been identified through the Theil-Sen results. Local cold spots (increasing annual SM) were observed over the Kamchatka Peninsula, The northern Chukotka and Sakha Republic districts, the Krasnoyarsk Territory, western Russia, southern Alaska, a section of the North Slope of Alaska, the McKenzie River Delta, southern British Columbia, and portions of Quebec. Over EA, 4.5% of tundra, 33% boreal forest, 17% boreal wetland, 30.5% boreal grass/shrub pixels were associated with annual SM hot spots (SI Figure 24) compared to 21.5%, 7.7%, 8%, and 5.5% of the pixels for respective vegetation classes that were associated with a SM cold spot. Whereas in NA, 5% tundra, 5.6% boreal forest, 19% boreal wetland and 11.5% boreal grass/shrub pixels were associated with a SM hot spot and 21% tundra, 23% boreal forest, 7% boreal wetland, and 11% grass/shrub pixels coincided with a SM cold spot. SM hot spots in spring were primarily in portions of Scandinavia, western Russia, southern Siberia, the Yukon-Kuskokwim Delta, and Canada (SI Figure 21), and cold spots were also observed across portions of Siberia, the Alaska North Slope and the McKenzie River Delta. Large hot spots in summer spanning central Siberia, portions of northern Alaska (Brooks Range region), and British Columbia. In autumn (SI Figure 23) the SM hot spots included central Siberia, and portions of Canada.

Regarding annual changes in non-frozen season FW (surface water inundation) both the Getis-Ord Gi* and Theil-Sen results indicated increasing FW across much of the domain (SI Figure 19) with substantial regional cold spots in EA over the Russian Far East, southern Siberia along the border with China and Mongolia, central Siberia, and the southern Ural and Volga regions. In NA the FW cold spots spanned much of Alaska, western Canada, along the western side of the Hudson Bay, and southern Quebec. When aggregated according to vegetation class, in EA 39.5% of the tundra, 48% of boreal forest, 52% of boreal wetland, and 47% of boreal grass/shrub pixels fell within identified FW cold spots (for FW hot spots, we identified 10% of EA tundra, 4.5% of boreal forest, 2.5% boreal wetland and 2% of boreal grass/shrub). In NA, 33% of tundra, 39% boreal forest, 35% boreal wetland and 46% of grass/shrub coincided with cold spots, compared to 6%, 6.5%, 5% and 4% falling under FW hot spots, respectively (SI Figure 24). Seasonally, FW increased (cold spot) over much of the region, with notable exceptions (i.e., hot spots) in summer in parts of central Alaska, northwest Canada, portions of the southern Canadian boreal, and portions of western Russia (SI Figure 22).

6.3 Vegetation change spots

Over the 1997–2017 record we identified substantial decreases in non-frozen season NDVI across the region. In EA we found that 59.6% of tundra, ˜31% boreal forest, 59% boreal wetland and boreal grass/shrub pixels were associated with a NDVI hot spot of decrease (SI Figure 24). In the change spot map (SI Figure 19) the locations of NDVI decrease in EA spanned northern and central Siberia, and northern Scandinavia. We also found that 30.8% of EA boreal forest pixels were associated with an NDVI increase compared to 2-6.5% for the other vegetation categories. The locations of NDVI increase were primarily in southern Scandinavia, western Russia, and the southern Siberian boreal. In NA, 50% of tundra, 61% of boreal forest, 66% of boreal wetland, and 63.5% boreal grass/shrub pixels were associated with NDVI decrease. As seen in the change spot map, much of Canada and Alaska (except for the North Slope which was neutral, and the Interior which showed NDVI increase) had decreasing NDVI. Approximately 2%, 7%, 3.6% and 4% of the respective NA vegetation categories had cold spots (increase in NDVI). Increasing NDVI in tundra included small, localized portions of the islands of Nunavut, boreal British Columbia, and boreal Interior Alaska.

Decreases in spring NDVI (SI Figure 21) were observed across much of boreal Canada and portions of Alaska, whereas increases in spring NDVI occurred across far western Canada and Nunavut. In EA, increasing spring NDVI occurred in western Russia, the Taymyr Peninsula/ North Siberian Lowlands, and portions of the southern Siberian boreal. And areas of decreasing NDVI were scattered primarily across central and southern boreal Siberia, and far eastern Siberia.

Increases in summer NDVI (SI Figure 22) occurred over much of Alaska (except for southern Alaska including the Yukon-Kuskokwim Delta), western Canada, southern Scandinavia, western Russia, and portions of Siberia (scattered throughout the domain). Areas of decreasing summer NDVI occurred in southern Alaska, over much of the Canadian tundra and boreal, northern Scandinavia, and were scattered throughout the Siberian tundra and boreal (including the Taymyr Peninsula, North Siberian Lowlands, and south of the Central Siberian Plateau). Over the autumn season (SI Figure 23), a majority of NA, a majority of northern Siberia and Scandinavia, showed a decrease in NDVI. Whereas small areas of autumn NDVI increase were primarily observed along the southern Siberian boreal, and southern Europe (western Russia and southern Scandinavia).

VOD (a microwave product, instead of optical product) was observed to increase (VOD cold spot) across much of Siberia, western Russia, portions of Scandinavia (including Norway), Alaska (except for the Interior), western Canada and other portions of boreal Canada (SI Figure 19). Areas of VOD decrease (hot spot) include portions of southern Siberia, portions of tundra in the Russian Far East, Central Siberian Plateau and southward into the West Siberian Plain. In NA, the VOD hot spots primarily occurred across central Canada (boreal extending into the northern tundra). Overall, according to vegetation category, in EA 28.5% tundra, 40% boreal forest, 46% boreal wetland, 47% boreal grass/shrub pixels were associated with a VOD cold spot (SI Figure 24). Likewise, 17% of EA tundra, 12% boreal forest, 11.5% boreal wetland, and 9% boreal grass/shrub were associated with a VOD hot spot. In NA, 36% of tundra, 32% of boreal forest, 35% boreal wetland and 50% of grass/shrub pixels were associated with a VOD cold spot, compared to 29% of tundra, 16% boreal forest, 20% boreal wetland, 12.5% boreal grass/shrub pixels associated with a VOD hot spot. In spring, VOD hot spots were observed over portions of southern Siberia, and central Canada (SI Figure 21). Much more of the region showed spring VOD cold spots, including across western Russia, Siberia, Alaska, western Canada, and southern Quebec. In summer (SI Figure 22) VOD hot spots occurred in portions of Interior Alaska, across much of boreal Canada, portions of Siberia, and Scandinavia. Whereas strong cold spots were observed in western Russia, eastern and central Siberia, southern and northern Alaska. Patterns of VOD change spots in autumn (SI Figure 23) were similar to those observed for summer.

Annual TC increased (TC cold spot) over much of the domain, including across Siberia, western Russia, Scandinavia, central Alaska, and boreal Canada (SI Figure 19). At the same time, NTC decreased (hot spot) over much of Scandinavia, western Russia, central and southern Siberia, Interior Alaska, western Canada and the southern portions of the central and eastern Canadian boreal. According to vegetation category in EA 12% tundra, 2% boreal forest, 3% boreal wetland and 5% boreal grass/shrub pixels were associated with a TC hotspot. Additionally, in NA 5% tundra, 41% boreal forest, 30% boreal wetland and 19% boreal grass/shrub pixels were associated with a NTC hotspot. For cold spots in EA 4% tundra, 50% boreal forest, 28% boreal wetland and 27% boreal grass/shrub pixels were observed to be TC cold spots. Likewise, in NA, 29% tundra, 6% boreal forest, 4% boreal wetland and 13% boreal grass/shrub pixels were associated with a NTC cold spot

Figures

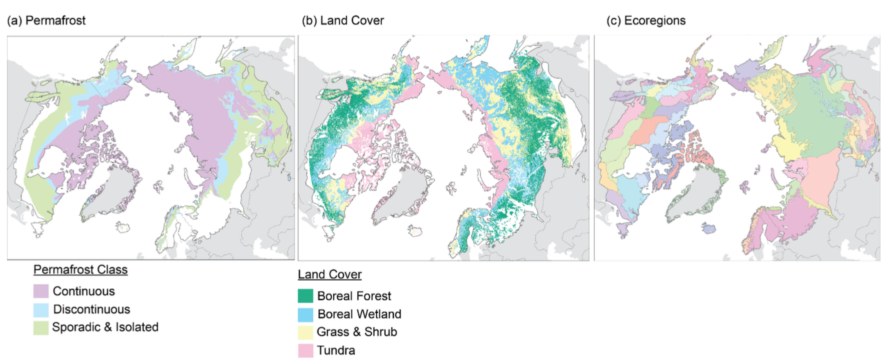

SI Figure 1. Maps showing the (a) spatial distribution of permafrost categories (continuous, discontinuous, sporadic/isolated; Brown et al., 2002); (b) land cover classes (adapted from Watts et al., 2023; see SI 1.2); (c) delineations of the 58 ecoregions within the Arctic-boreal region (see Olson et al., 2001 and our project's data repository for a description of individual region

SI Figure 2. Spatial patterns of multi-year average indicator state (in native spatial resolutions) across the Arctic-boreal region for annual: (a) average AT (°C; 1997–2020); (b) NFS length (days; 1997–2020); (c) ALT (m; 1997–2019); (d) sum PPT (m; 1997–2020); (e) average VPD (kPa; 1997–2020); (f) sum of snow cover (km^2; 1997–2020); (g) average non-winter season SM (m^3 m^{-3}; 1997–2020); (h) average non-frozen season FW coverage (% of 25x25 km grid cell; 2003–2020); (i) average NDVI (unitless; 1997–2017); (j) average VOD (unitless; 1997–2020); (k) TC (% of 0.05° grid cell; 1997–2016); (l) NTC (% of 0.05° grid cell; 1997–2016).

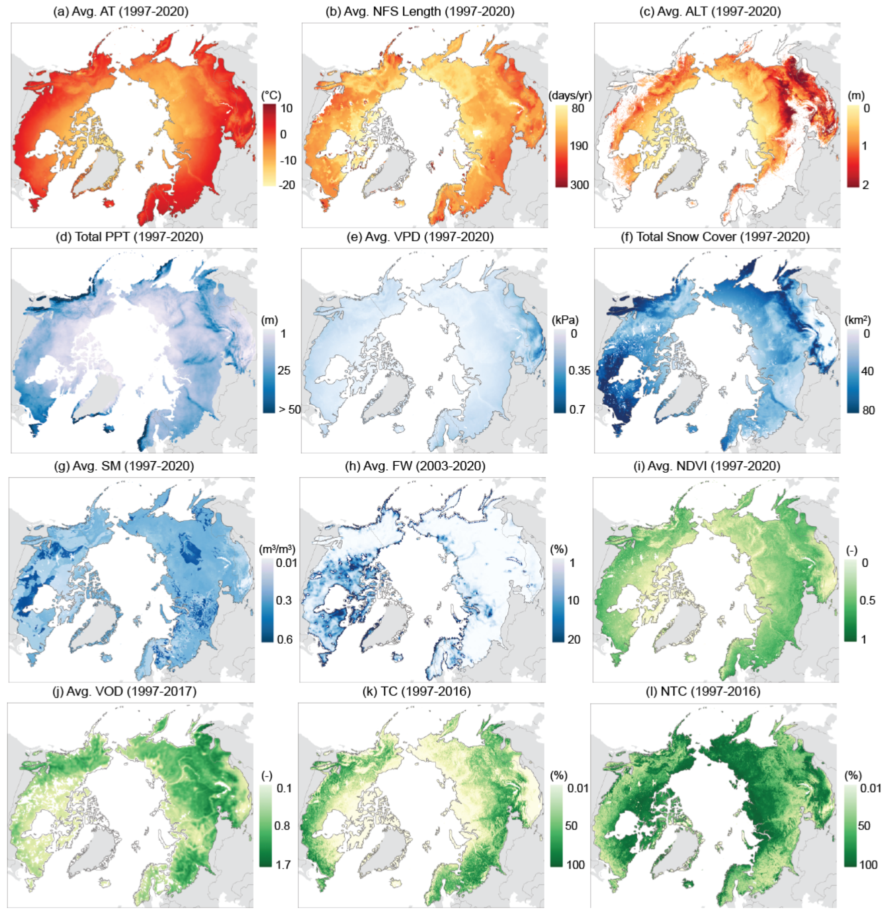

SI Figure 3. Indicator time series over the full Arctic-boreal domain, the full tundra region, and the full boreal region for: (a) annual average AT (°); (b) annual total NFS (days); (c) annual maximum ALT (m); (d) annual total PPT (m); (e) annual total winter SC (Mkm^2); (f) annual average VPD (kPa); (g) annual non-frozen season SM (cm^3/cm^3); (h) annual average non-frozen season FW (% pixel coverage); (i) annual non-frozen season NDVI (unitless); (j) annual non-frozen VOD (unitless); (k) annual TC (%); (l) annual NTC (%).

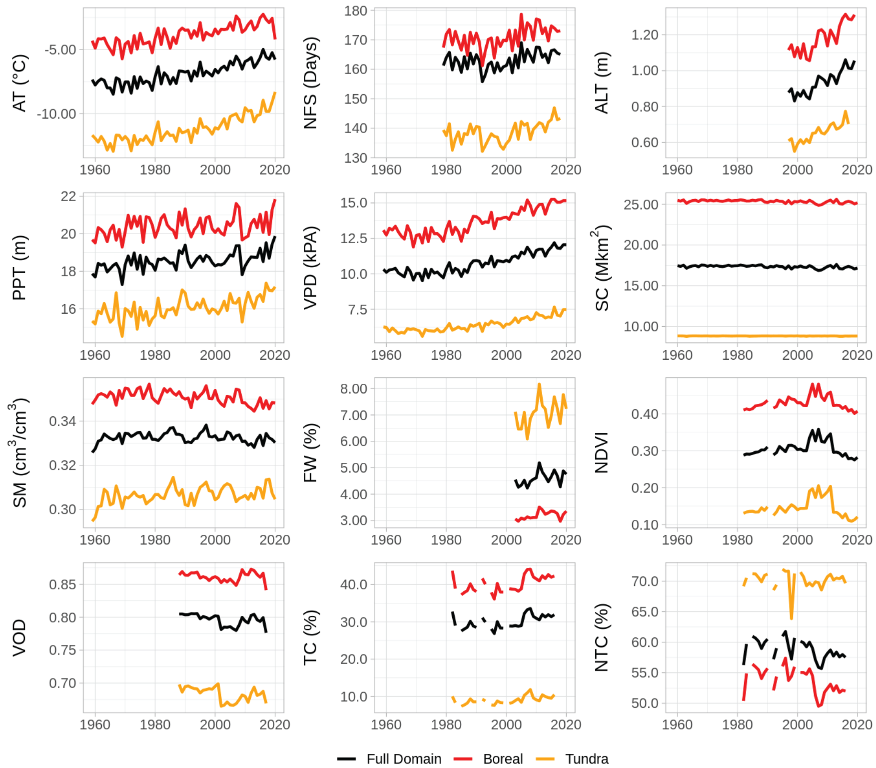

SI Figure 4. Thiel-Sen trend maps for (a, b) annual average AT (°C/decade; 1980–2020) and (°C/decade; 1997–2020); (c, d) annual NFS length (days/decade; 1980–2020) and (days/decade; 1997–2020); (e) annual ALT (m/decade; 1997–2019). Shown are grid cells having significant trend (α = 0.05).

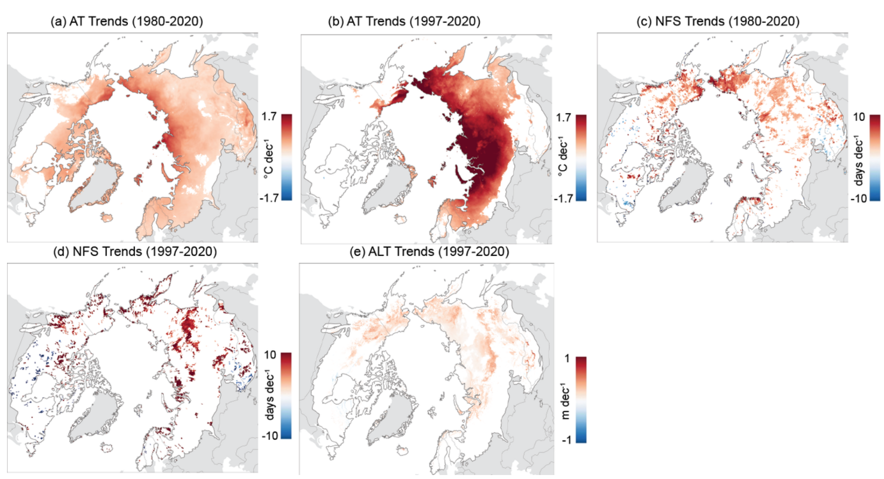

SI Figure 5. Thiel-Sen trend maps for annual (a, b) total PPT (m/decade; 1980–2020; 1997–2020); (c, d) total snow cover (km^2/decade; 1980–2020; 1997–2020); (e, f) average non-winter VPD (kPa/decade; 1980–2020; 1997–2020); (g, h) average non-winter SM (cm^3 cm^{-3}/decade; 1980–2020; 1997–2019); (i) average non-winter FW (% dec^{-1}). Shown are grid cells having significant trend (α = 0.05).

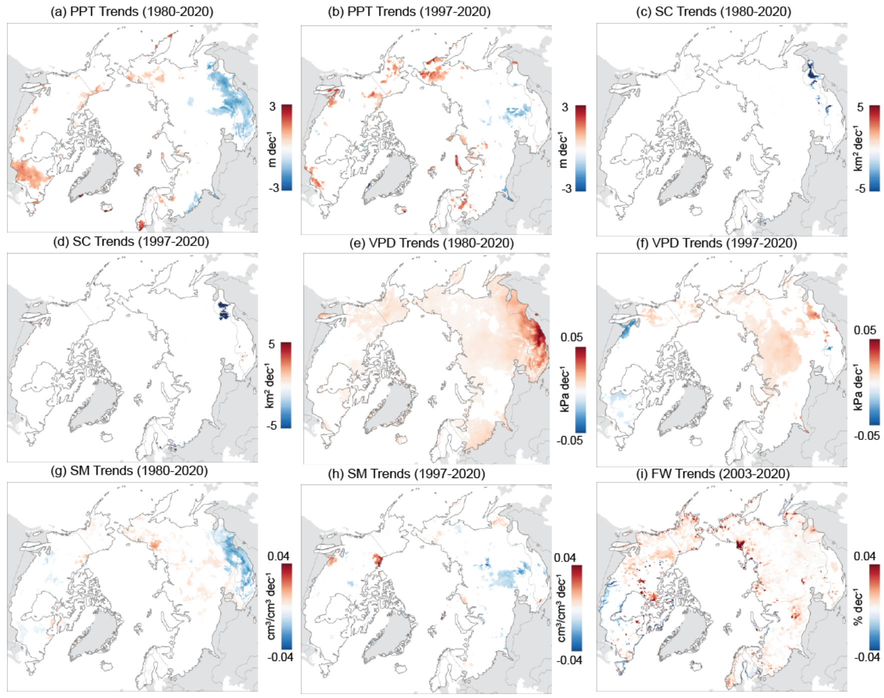

SI Figure 6. Thiel-Sen trend maps for annual average NDVI (a; 1987–2020) and (b; 1997–2020); annual average VOD (c; 1988–2017) and (d; 1997–2017); annual TC (e; 1997–2016) and NTC (f; 1997–2016). Shown are grid cells having significant trend (α = 0.05).

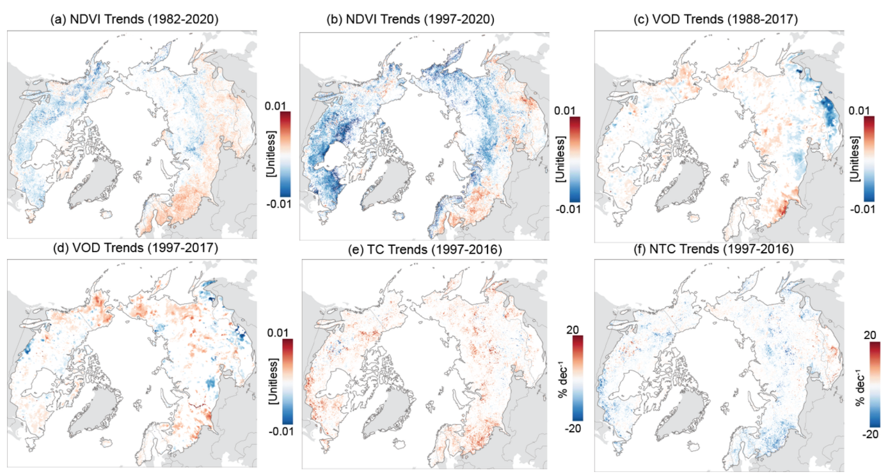

SI Figure 7. Percent of permafrost region impacted by significant change in annual: (a) average AT (°C); (b) total NFS (days); (c) maximum ALT (m); (d) total PPT (m); (e) total winter SC (km^2); (f) average VPD (kPa); (g) non-frozen season FW (%); (h) average non-frozen season SM (cm^{3}cm^{-3}); (i) average non-frozen season NDVI (unitless); (j) average non-frozen season VOD (unitless). Permafrost categories are continuous (C), discontinuous (D), sporadic/isolated (SI).

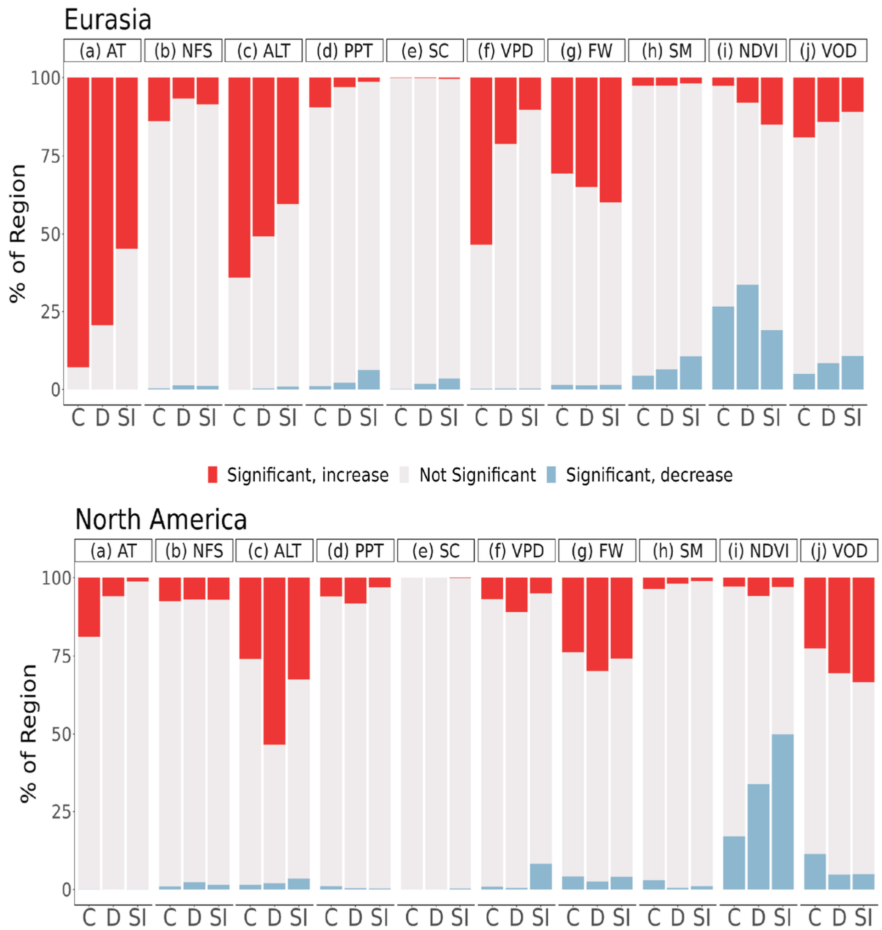

SI Figure 8. Locations of fire disturbance, according to decadal per-pixel (0.25 x 0.25°) burned area (ranging from ˜0.01 to >100 km^2) from GFED4 (Randerson et al., 2018) spanning (a) 1997–2006, and (b) 1997–2007.

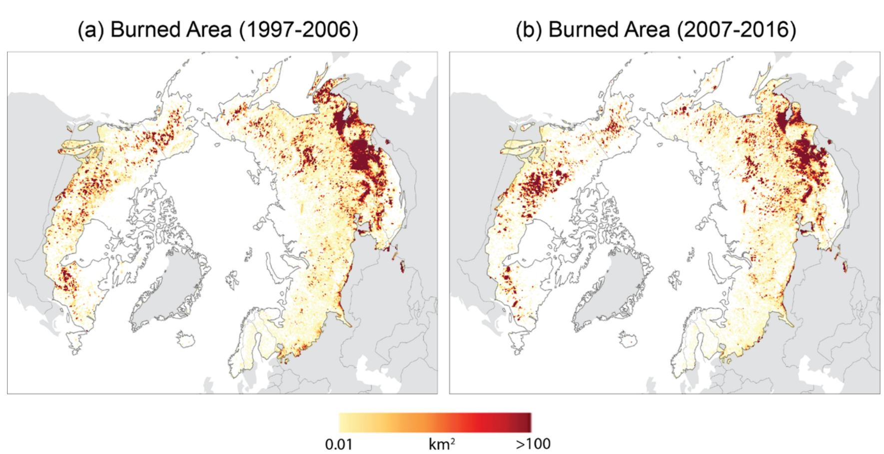

SI Figure 9. Percent of grid cells having a significant positive (+), negative (-), or no trend (0) as co-located with minimal (yellow; >0-0.8 km^2; yellow), moderate (0.81-5.65 km^2; orange) and large (5.66 – 343 km^2; red) fire disturbance within a grid cell, for 1) Eurasia and 2) North America, over the 1997–2020 period.

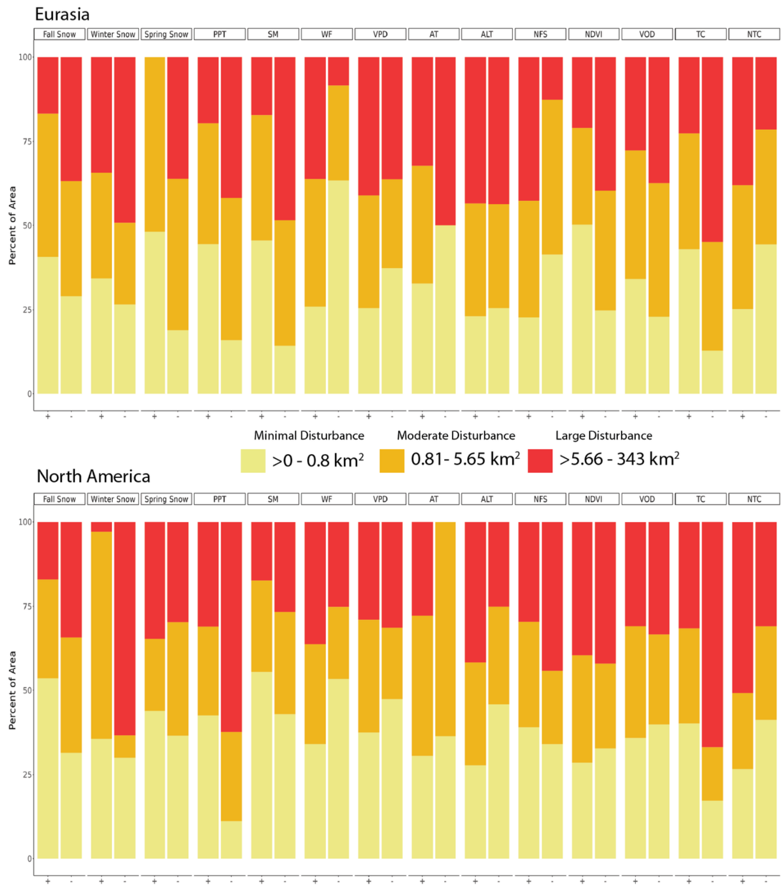

SI Figure 10. Thiel-Sen trend maps indicating changes in annual winter (December – February) conditions for (a, b) average AT (°C/decade; 1980–2020; 1997–2020); (c, d) NF length (days/decade; 1980–2020; 1997–2020); (e, f) total PPT (m/decade; 1980–2020; 1997–2019); (g, h) average VPD (kPa/decade; 1980–2020; 1997–2020); (i, j) total SC (km2/decade; 1980–2020; 1997–2020). Shown are grid cells having significant trend (α = 0.051).

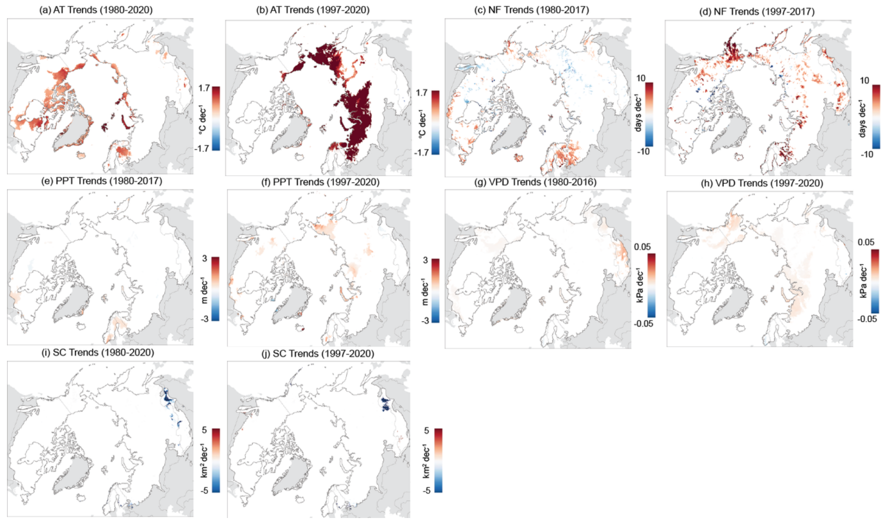

SI Figure 11. Thiel-Sen trend maps indicating changes in annual spring (March – May) conditions for (a, b) average AT (°C/decade; 1980–2020; 1997–2020); (c, d) NF length (days/decade; 1980–2020; 1997–2020); (e, f) total PPT (m/decade; 1980–2020; 1997–2019); (g, h) total SC (km^2/decade; 1980–2020; 1997–2020); (i, j) average VPD (kPa/decade; 1980–2020; 1997–2020); (k, l) average SM (cm^3/cm^3; 1980–2020; 1997–2020); (m, n) average NDVI (unitless; 1987–2020; 1997–2020); (o, p) average VOD (unitless; 1988–2017; 1997–2017). Shown are grid cells having significant trend ($\alpha = 0.051$).

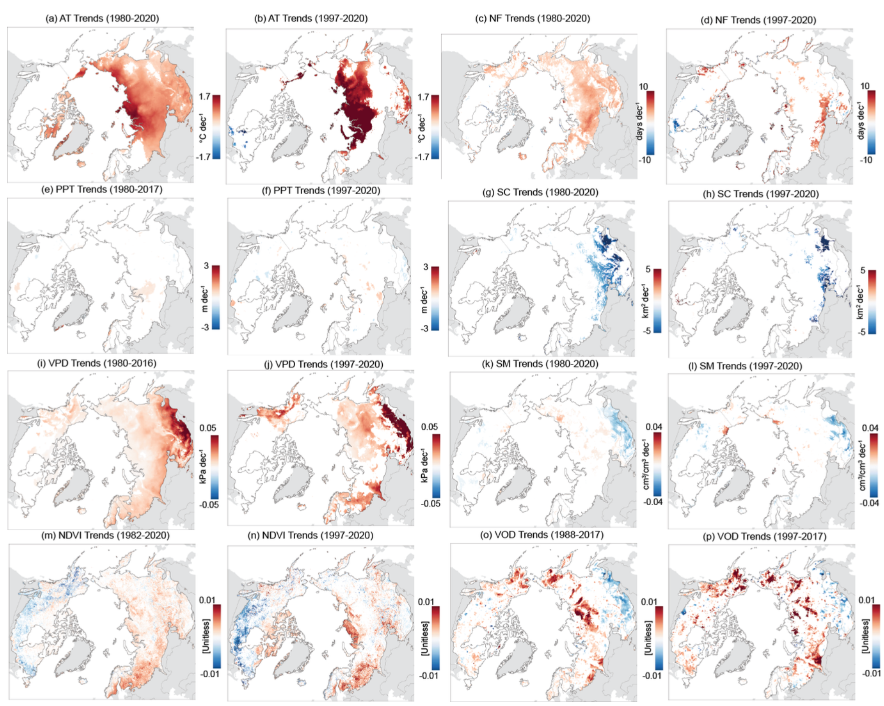

SI Figure 12. Thiel-Sen trend maps indicating changes in annual summer (June – August) conditions for (a, b) average AT (°C/decade; 1980–2020; 1997–2020); (c, d) total PPT (m/decade; 1980–2020; 1997–2019); (e, f) average VPD (kPa/decade; 1980–2020; 1997–2020); (g, h) average SM (cm^3/cm^3; 1980–2020; 1997–2020);

(i, j) average NDVI (unitless; 1987–2020; 1997–2020); (k,l) average VOD (unitless; 1988–2017; 1997–2017). Shown are grid cells having significant trend (α = 0.051).

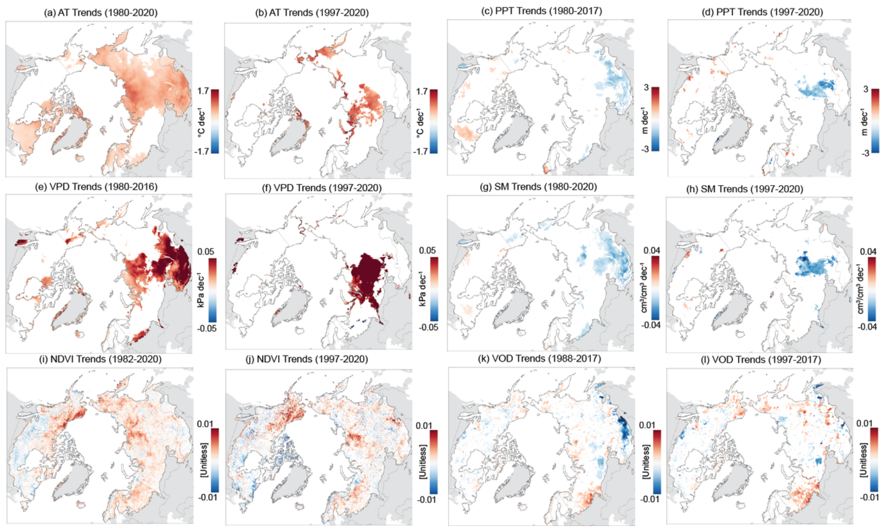

SI Figure 13. Thiel-Sen trend maps indicating changes in annual autumn (September – November) conditions for (a, b) average AT (°C/decade; 1980–2020; 1997–2020); (c, d) NF length (days/decade; 1980–2020; 1997–2020); (e, f) total PPT (m/decade; 1980–2020; 1997–2019); (g, h) total SC (km^2/decade; 1980–2020; 1997–2020); (i, j) average VPD (kPa/decade; 1980–2020; 1997–2020); (k, l) average SM (cm^3/cm^3; 1980–2020; 1997–2020); (m, n) average NDVI (unitless; 1987–2020; 1997–2020); (o,p) average VOD (unitless; 1988–2017; 1997–2017). Shown are grid cells having significant trend (α = 0.051).

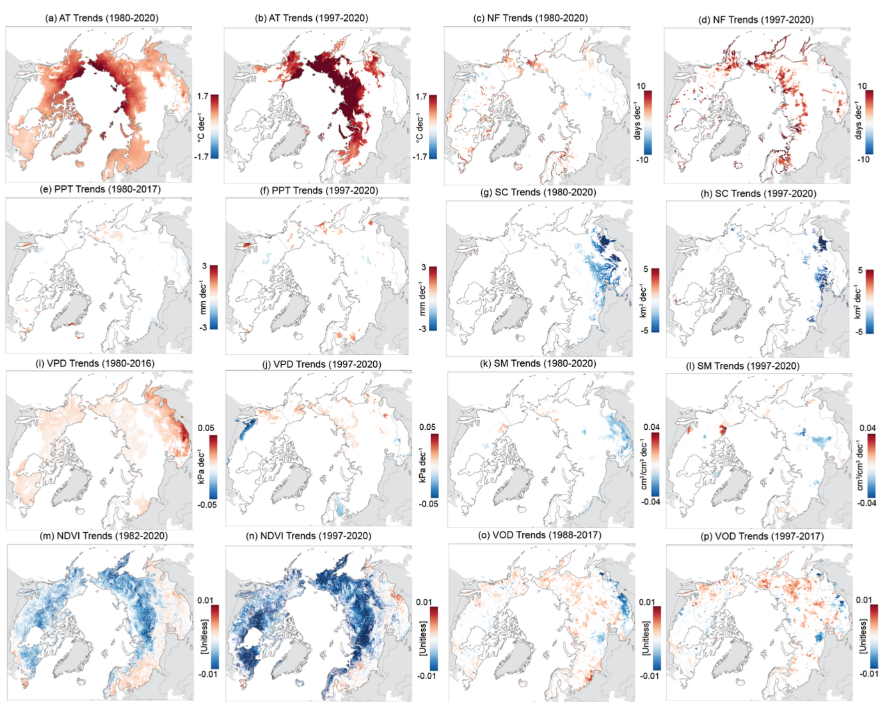

SI Figure 14. Thiel-Sen trend maps indicating changes in FW (%/decade) for spring (March–May), summer

(June–August) and autumn (September – November) seasons over the 2003–2020 period. Shown are grid cells having significant trend ($\alpha = 0.05$).

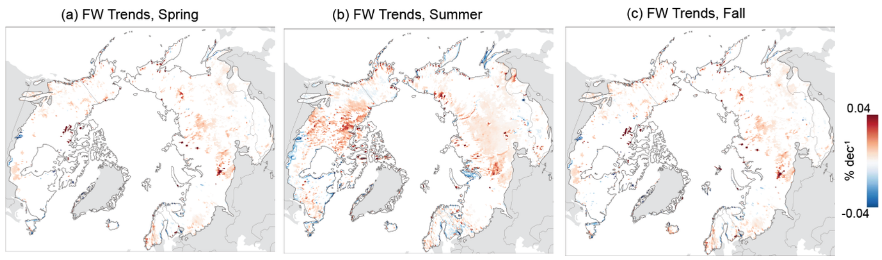

SI Figure 15. Percent of region impacted by significant change in winter (December–February): (a) average AT(°C); (b) total NF (days); (c) total PPT (m); (d) total winter SC (km^2); (e) average VPD (kPa). Land cover categories are boreal forest (BF), boreal wetland (BWL), boreal grass and shrub (G/S), and tundra (TUN) within (1) Eurasia and (2) North America.

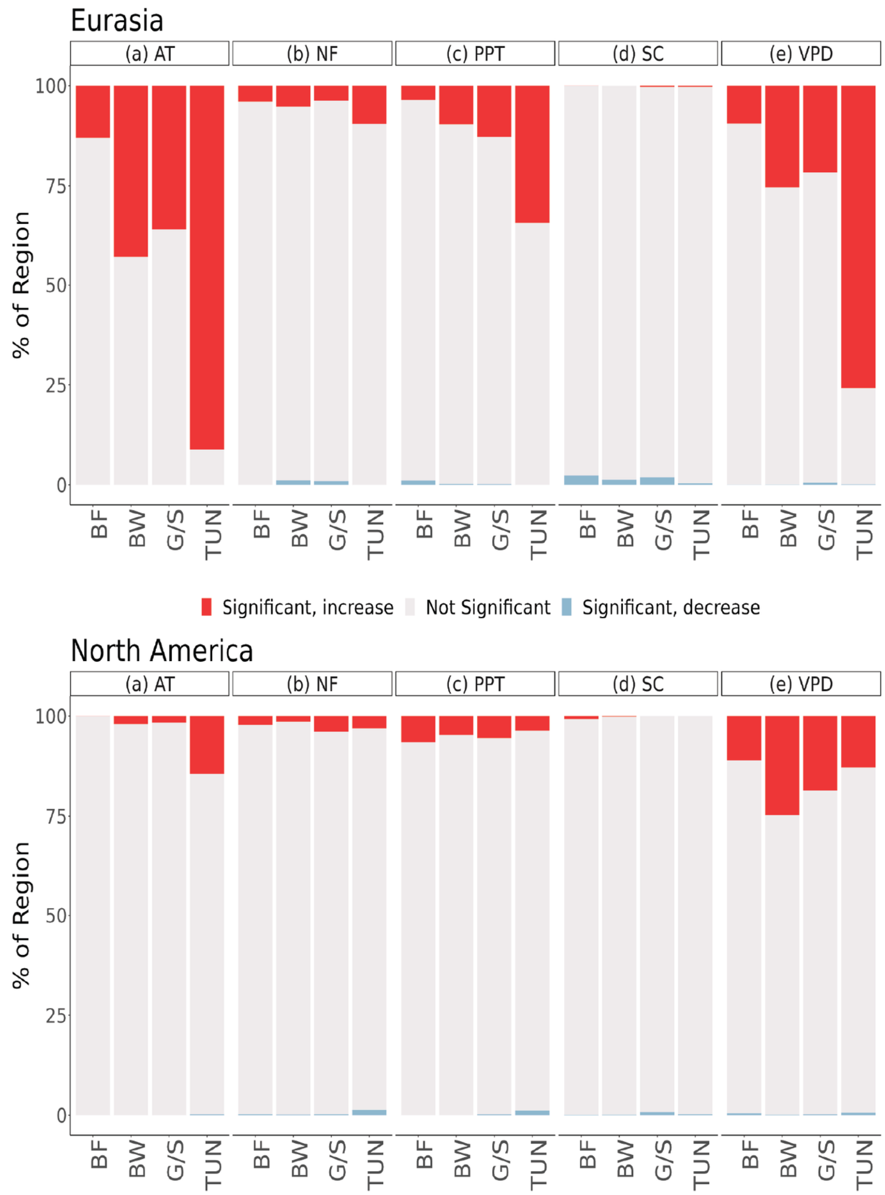

SI Figure 16. Percent of region impacted by significant change in spring (March–May): (a) average AT (°C); (b) total NF (days); (c) total PPT (m); (d) total SC (km^2); (e) average VPD (kPa); (f) average SM (cm^3/cm^3); (g) average NDVI (unitless); (h) average VOD (unitless). Land cover categories are boreal forest (BF), boreal wetland (BWL), boreal grass and shrub (G/S), and tundra (TUN) within (1) Eurasia and (2) North America.

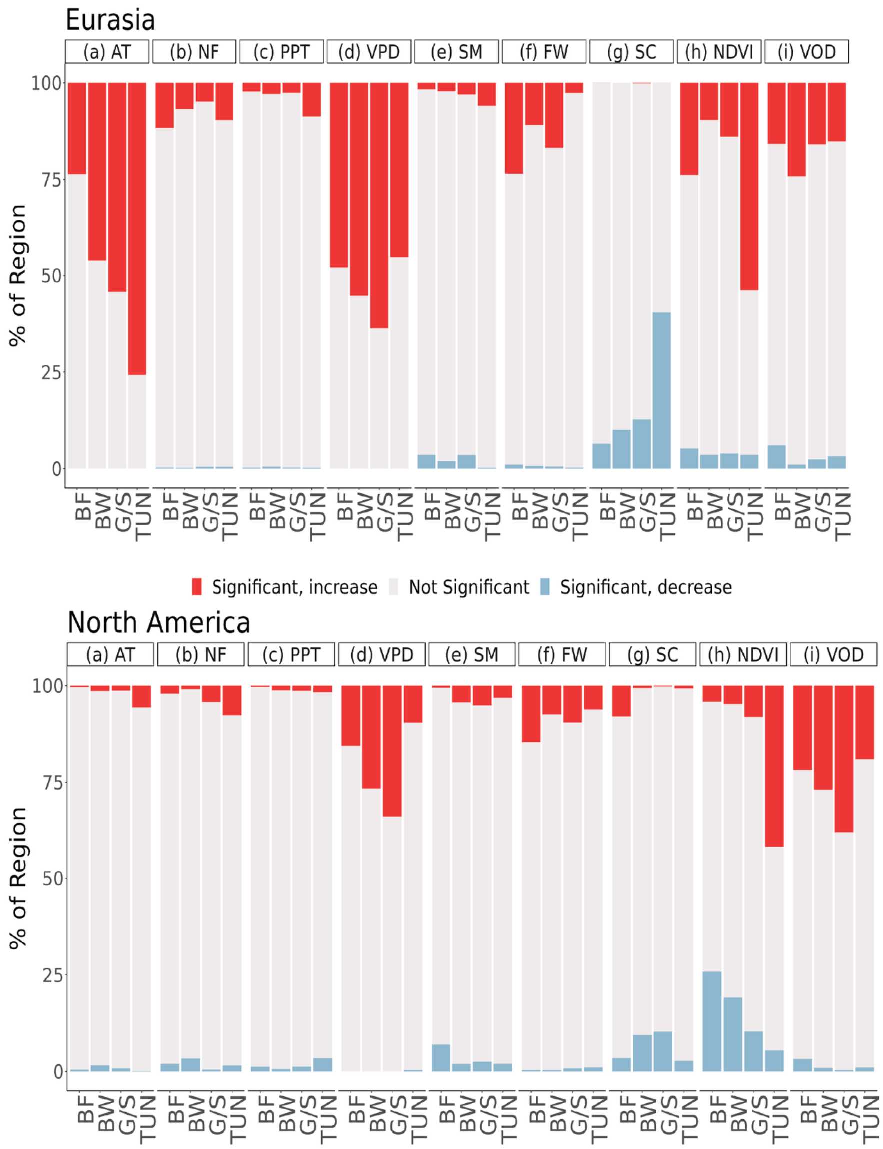

SI Figure 17. Percent of region impacted by significant change in summer (June–August): (a) average AT (°C); (b) total NF (count); (c) total PPT (m); (d) total SC (km^2); (e) average VPD (kPa); (f) average SM (cm^3/cm^3); (g) average NDVI (unitless); (h) average VOD (unitless). Land cover categories are boreal forest (BF), boreal wetland (BWL), boreal grass and shrub (G/S), and tundra (TUN) within (1) Eurasia and (2) North America.

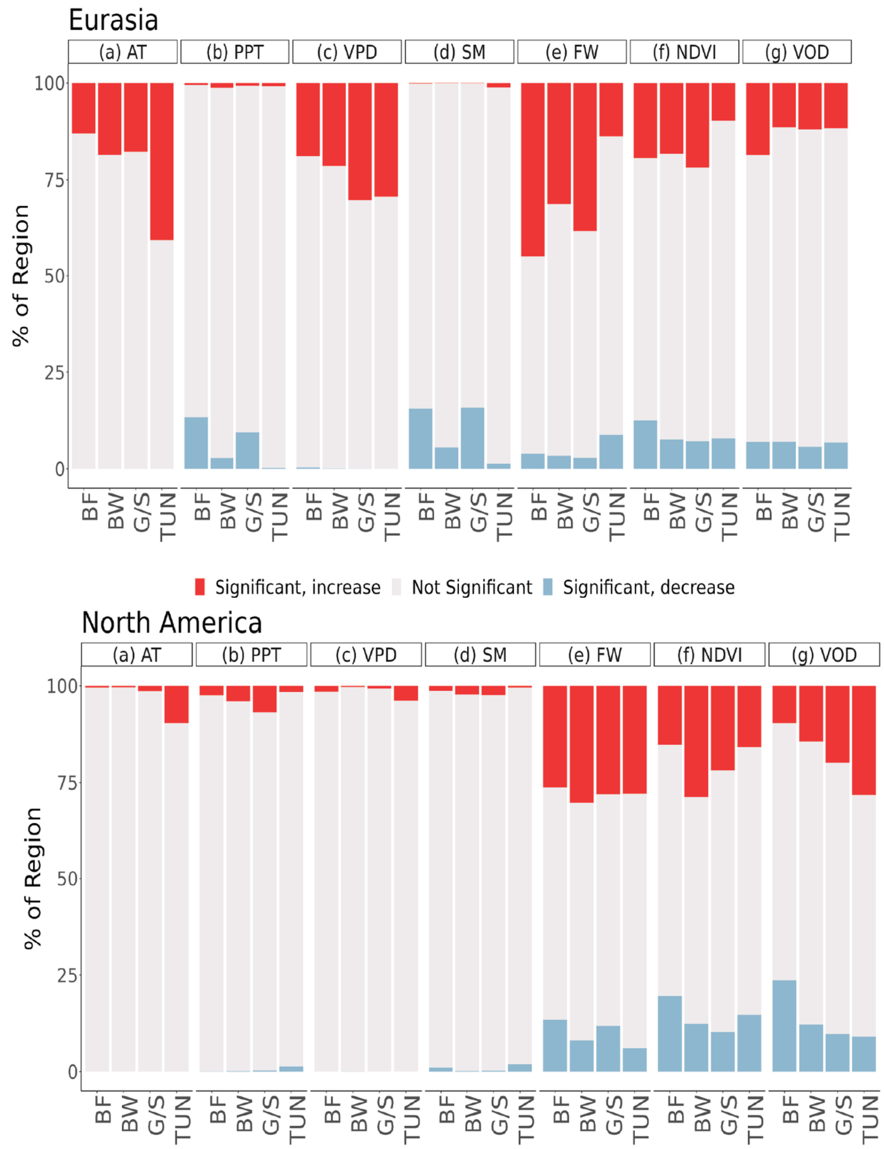

SI Figure 18. Percent of region impacted by significant change in autumn (September–November): (a) average AT (°C); (b) total NF (days); (c) total PPT (m); (d) total SC (km^2); (e) average VPD (kPa); (f) average SM (cm^3/cm^3); (g) average NDVI (unitless); (h) average VOD (unitless). Land cover categories are boreal forest (BF), boreal wetland (BWL), boreal grass and shrub (G/S), and tundra (TUN) within (1) Eurasia and (2) North America.

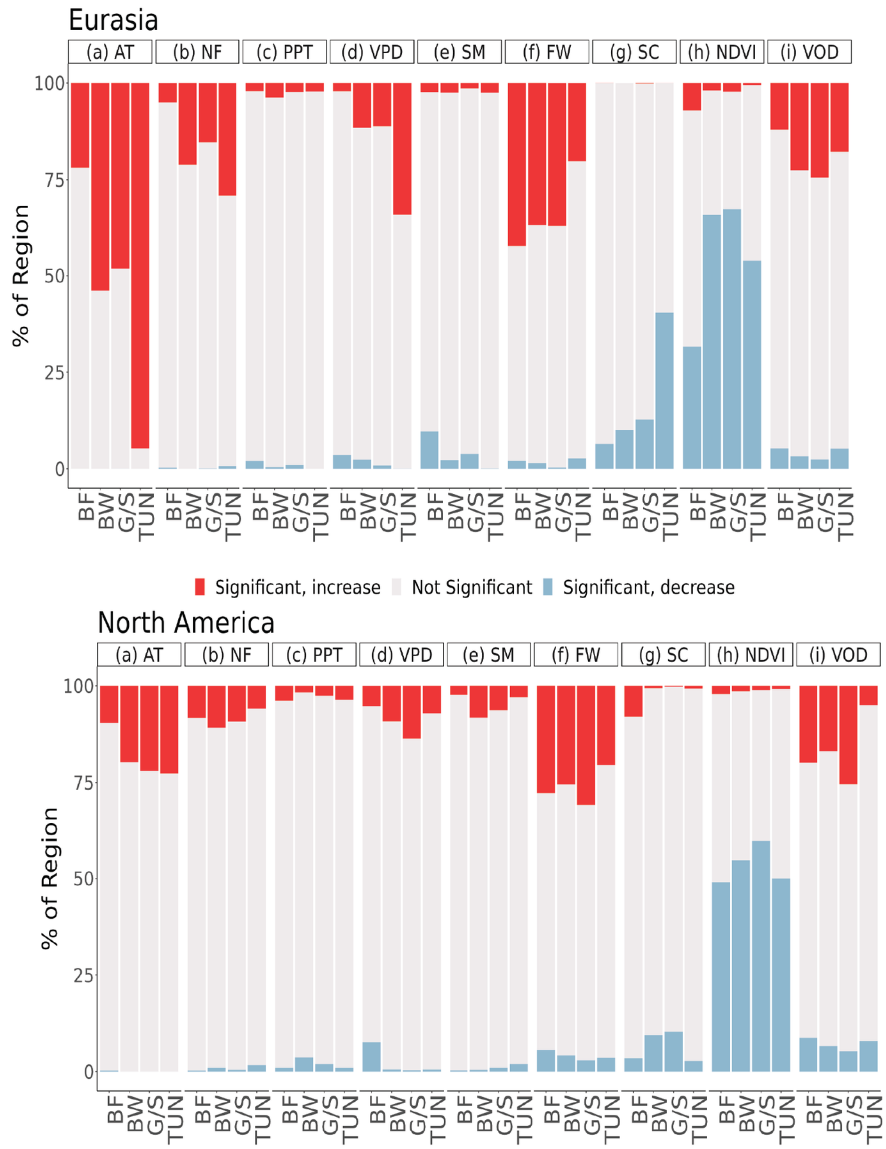

SI Figure 19. Maps of Indicator Getis-ord Gi* change spots for annual: (a) average AT (°C); (b) total NFS (days); (c) maximum ALT (m); (d) total PPT (m); (e) total frozen season SC area (km^2); (f) average VPD (kPa); (g) non-frozen season SM (cm^3 cm^{-3}); (h) non-frozen season FW (%); (i) non-frozen season NDVI (unitless); (j) non-frozen season VOD (unitless); (k) TC (%); (l) NTC (%). Negative values (blue colors) indicate areas of decrease; positive values (red colors) indicate areas of increase. Areas without detected changes (i.e., below a 90% confidence interval) are indicated in white.

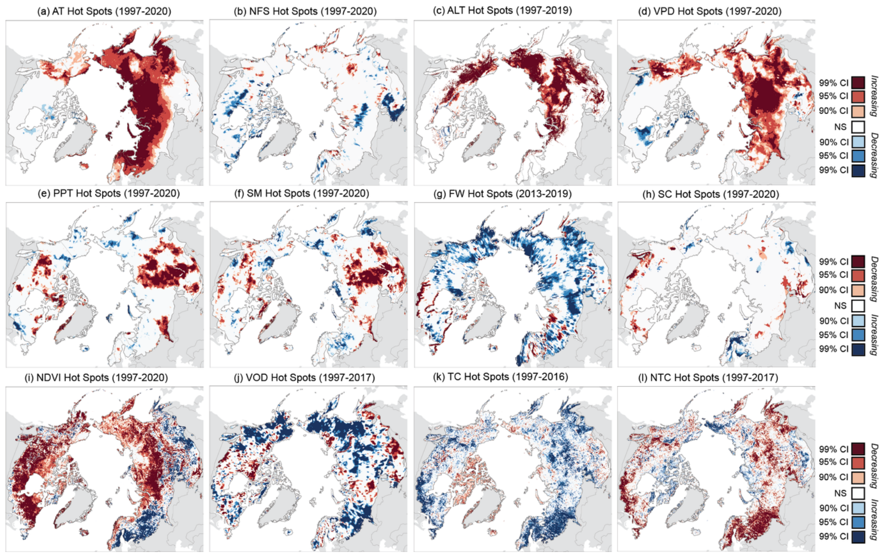

SI Figure 20. Maps of Indicator Getis-ord Gi* change spots for annual winter (December–February): (a) average AT (°C); (b) total FS (days); (c) total PPT (m); (d) total SC area (km^2); (e) average VPD (kPa). Negative values (blue colors) indicate areas of decrease; positive values (red colors) indicate areas of increase. Areas without detected changes (i.e., below a 90% confidence interval) are indicated in white.

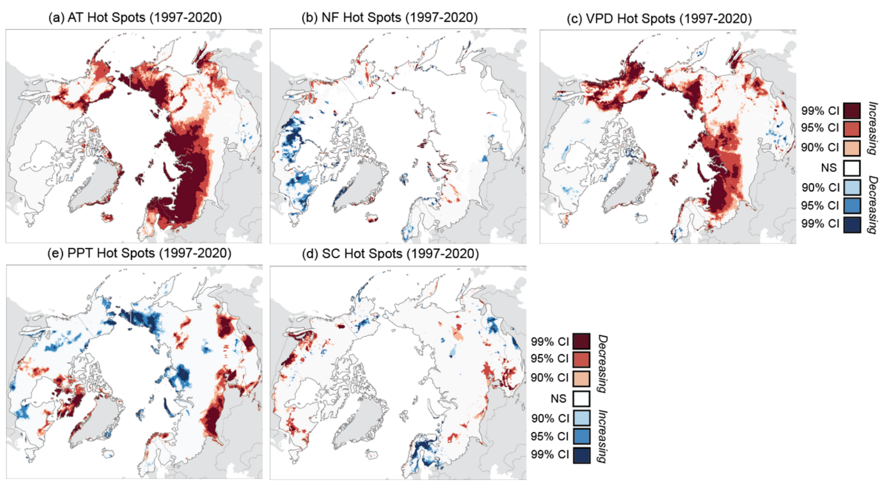

SI Figure 21. Maps of Indicator Getis-ord Gi* change spots for annual spring (March–May): (a) average AT (°C); (b) total NFS (days); (c) average VPD (kPa); (d) total PPT (m); (e) SM (cm^{3}cm^{-3}); (f) FW (%); (g) total SC area (km^2); (h) NDVI (unitless); (i) VOD (unitless). Negative values (blue colors) indicate areas of decrease; positive values (red colors) indicate areas of increase. Areas without detected changes (below a 90% confidence interval) are indicated in white.

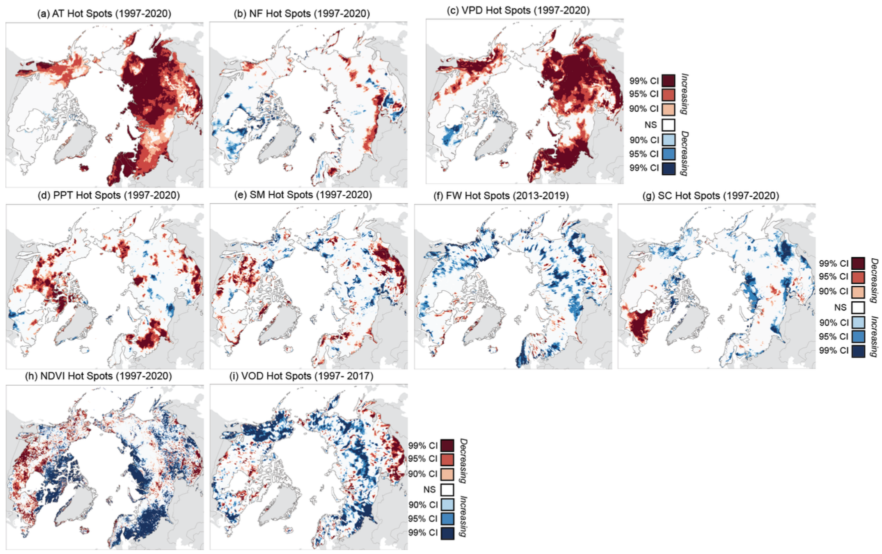

SI Figure 22. Maps of Indicator Getis-ord Gi* change spots for annual summer (June–August): (a) average AT (°C); (b) average VPD (kPa); (c) total PPT (m); (d) SM ($cm^3 cm^{-3}$); (e) FW (%); (f) NDVI (unitless); (g) VOD (unitless). Negative values (blue colors) indicate areas of decrease; positive values (red colors) indicate areas of increase. Areas without detected changes (i.e., below a 90% confidence interval) are indicated in white.

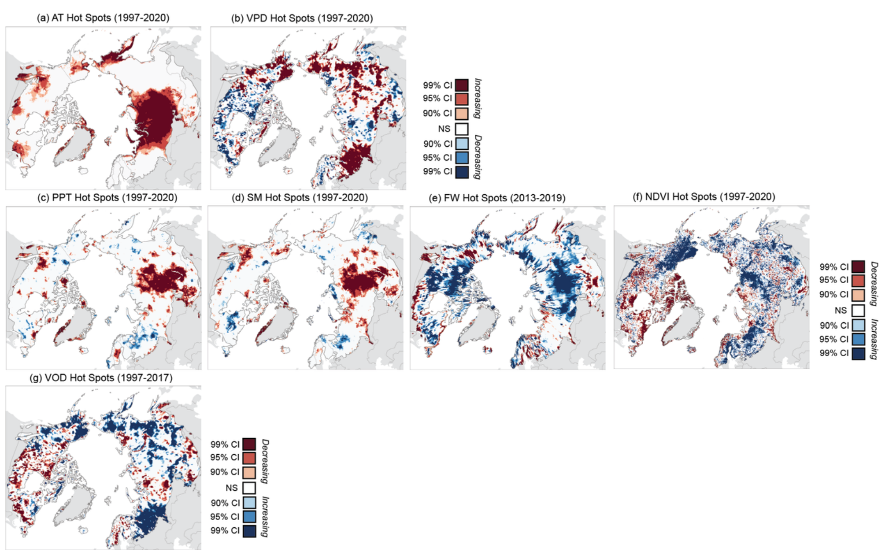

SI Figure 23. Maps of Indicator Getis-ord Gi* change spots for annual autumn (September–November): (a) average AT (°C); (b) total NFS (days); (c) average VPD (kPa); (d) total PPT (m); (e) SM (cm^3 cm^{-3}); (f) FW (%); (g) total SC area (km^2); (h) NDVI (unitless); (i) VOD (unitless). Negative values (blue colors) indicate areas of decrease; positive values (red colors) indicate areas of increase. Areas without detected changes (i.e., below a 90% confidence interval) are indicated in white.

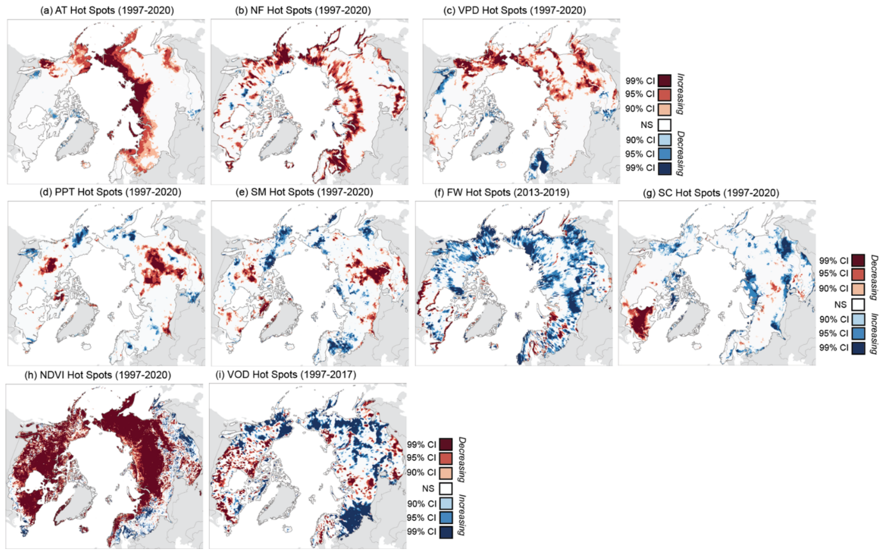

SI Figure 24. Percent of region impacted by identified change (according to Getis-ord Gi* analysis) in annual: (a) average AT (°C); (b) total NFS (days); (c) maximum ALT (m); (d) total PPT (m); (e) total winter SC (km^2); (f) average VPD (kPa); (g) non-frozen season FW (%); (h) average non-frozen season SM (cm^{3}cm^{-3}); (i) average non-frozen season NDVI (unitless); (j) average non-frozen season VOD (unitless), (k) TC (%), and (l) NTC (%) . Land cover categories are boreal forest (BF), boreal wetland (BW), boreal grass/shrub (G/S), and tundra (TUN).

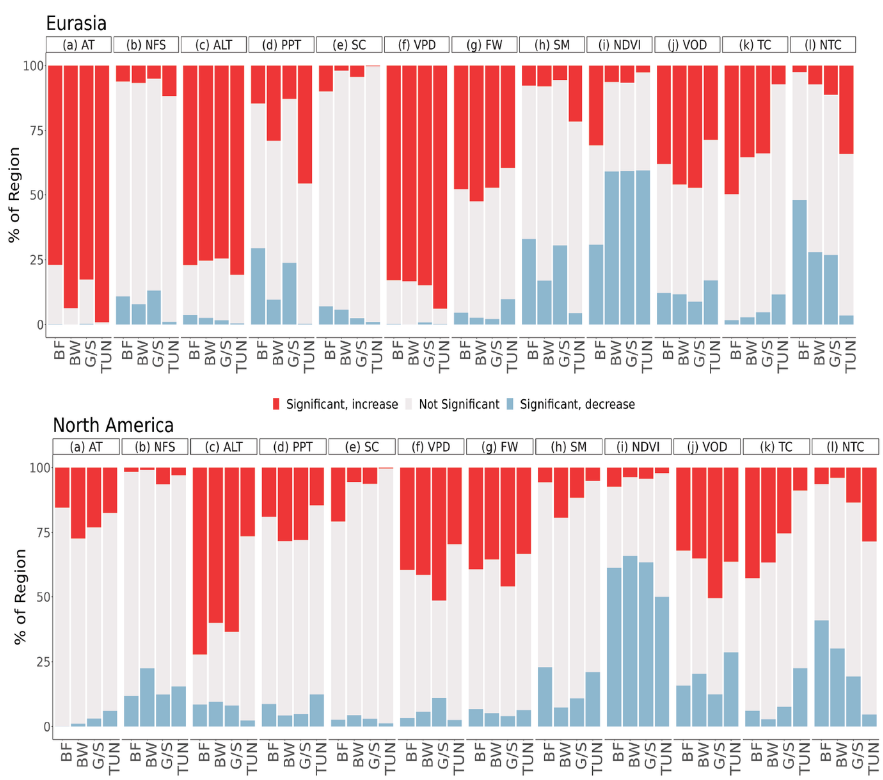

SI Figure 25. Percent of region impacted by identified change (according to Getis-ord Gi* analysis) in winter (December–February): (a) average AT(°C); (b) total NF (days); (c) total PPT (m); (d) total SC (km^2); (e) average VPD (kPa). Land cover categories are boreal forest (BF), boreal wetland (BWL), boreal grass and shrub (G/S), and tundra (TUN) within (1) Eurasia and (2) North America.

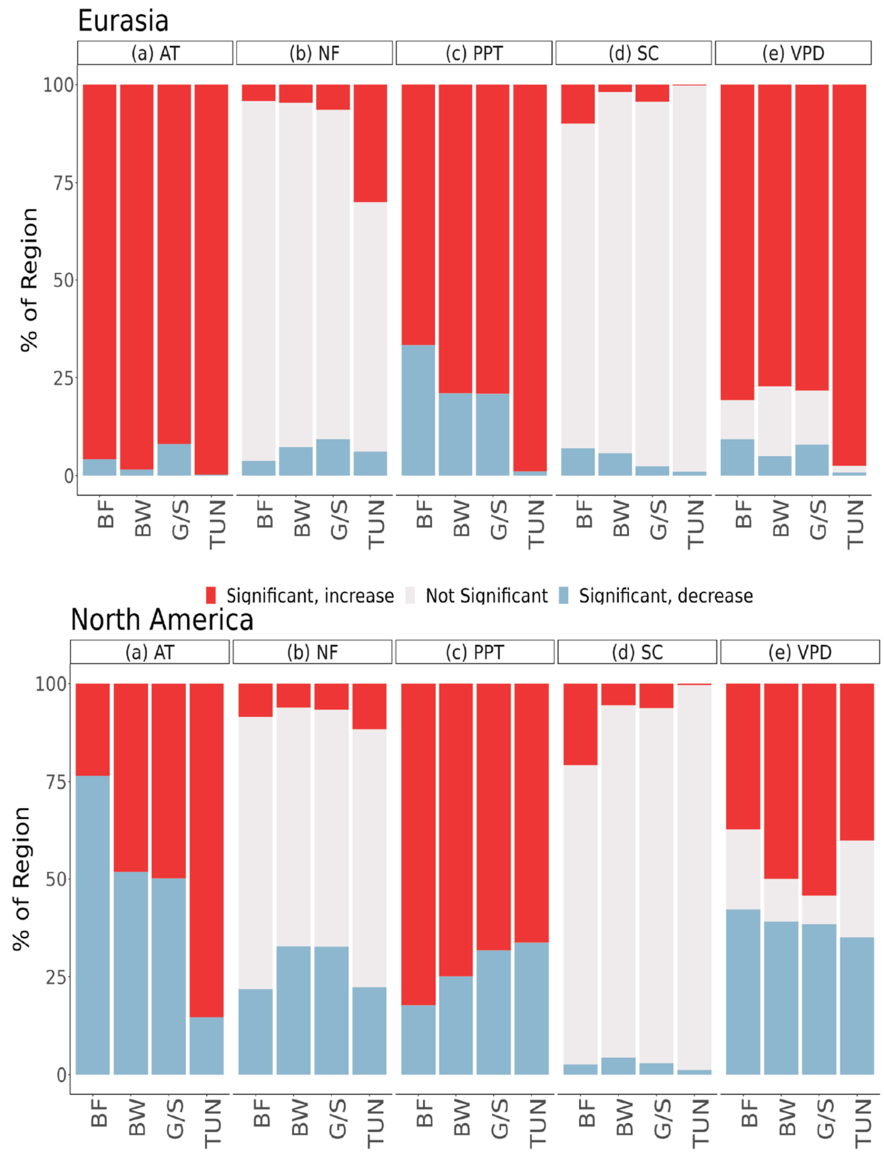

SI Figure 26. Percent of region impacted by identified change (according to Getis-ord Gi* analysis) in spring (March–May): (a) average AT (°C); (b) total NF (days); (c) total PPT (m); (d) total winter SC (km^2); (e) average VPD (kPa); (f) average SM (cm^3/cm^3); (g) average NDVI (unitless); (h) average VOD (unitless). Land cover categories are boreal forest (BF), boreal wetland (BWL), boreal grass and shrub (G/S), and tundra (TUN) within (1) Eurasia and (2) North America.

SI Figure 27. Percent of region impacted by identified change (according to Getis-ord Gi* analysis) in summer (June–August): (a) average AT (°C); (b) total PPT (m); (c) average VPD (kPa); (d) average SM (cm^3/cm^3); (e) average NDVI (unitless); (f) average VOD (unitless). Land cover categories are boreal forest (BF), boreal wetland (BWL), boreal grass and shrub (G/S), and tundra (TUN) within (1) Eurasia and (2) North America.

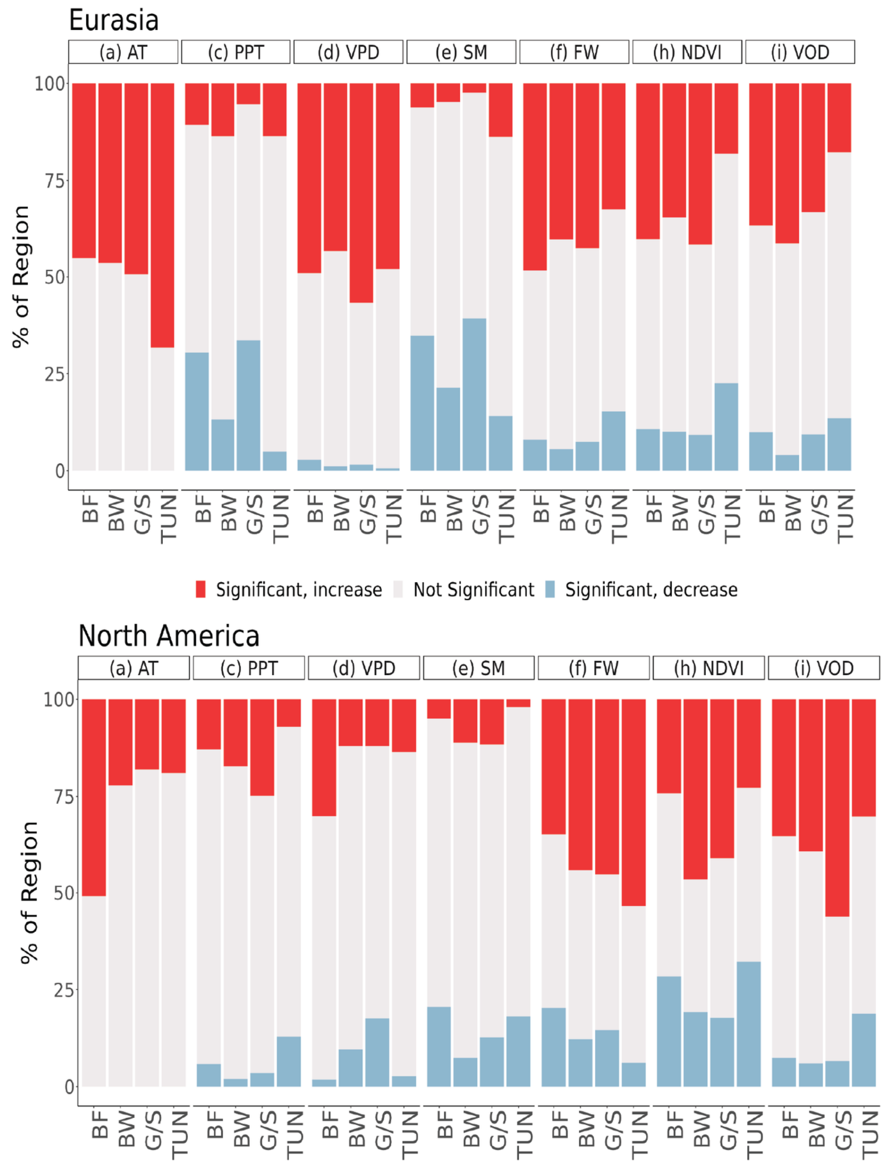

SI Figure 28. Percent of region impacted by identified change (according to Getis-ord Gi* analysis) in autumn (September–November): (a) average AT (°C); (b) total NF (days); (c) total PPT (m); (d) total SC (km^2); (e) average VPD (kPa); (f) average SM (cm^3/cm^3); (g) average NDVI (unitless); (h) average VOD (unitless). Land cover categories are boreal forest (BF), boreal wetland (BWL), boreal grass and shrub (G/S), and tundra (TUN) within (1) Eurasia and (2) North America.

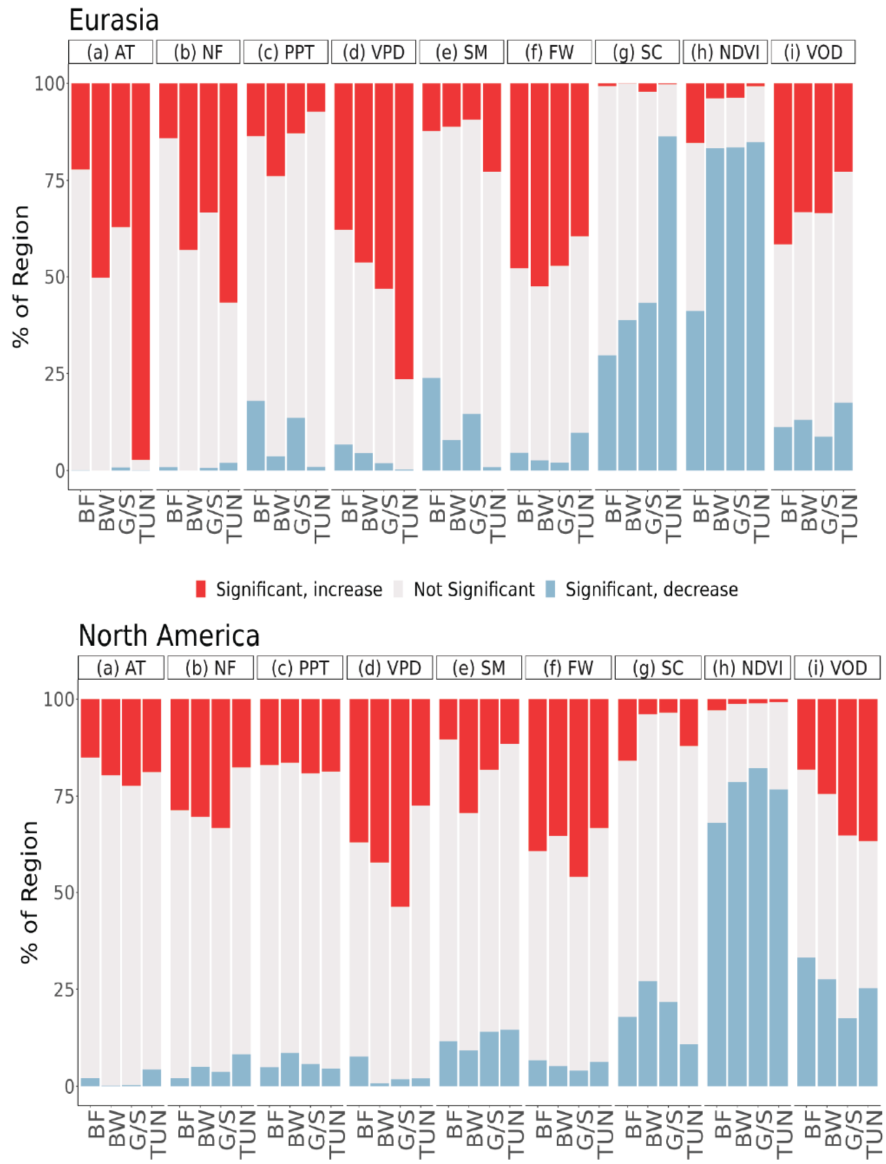

SI Figure 29. Percent of permafrost region impacted by identified change (according to Getis-ord Gi* analysis)) in annual: (a) average AT (°C); (b) total NFS (days); (c) maximum ALT (m); (d) total PPT (m); (e) total winter SC (km^2); (f) average VPD (kPa); (g) non-frozen season FW (%); (h) average non-frozen season SM (cm^3 cm^{-3}); (i) average non-frozen season NDVI (unitless); (j) average non-frozen season VOD (unitless). Permafrost categories are continuous (C), discontinuous (D), sporadic/isolated (SI).

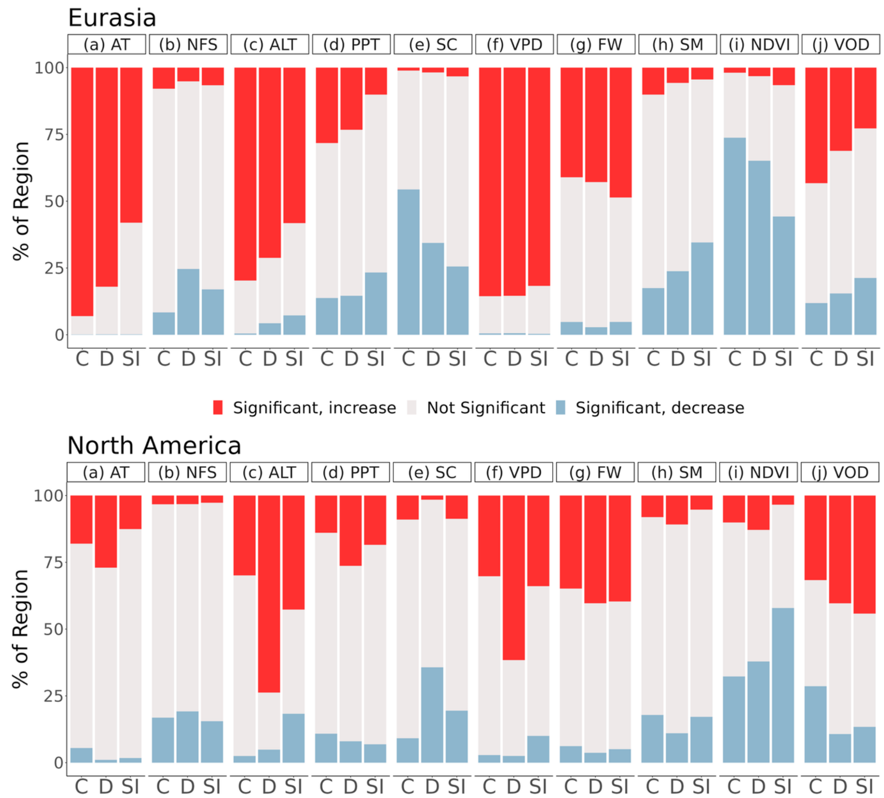

SI Figure 30. Multivariate Getis-ord Gi*-based change score maps for the spring (March – May) 1997–2020 period (unless otherwise indicated), according to select thermal, moisture, and vegetation Indicators, for which a change in an identified "detrimental" direction is occurring. Thermal (a) includes annual: average increase in AT (°C) and total NFS (days). Moisture (b) includes annual: declines in total PPT (m); increase in average VPD (kPa); decrease in average non-frozen season SM (cm^3 cm^{-3}). Vegetation (c) includes: decrease in average NDVI (unitless; 1997–2020), decrease in average VOD (unitless; 1998–2017).

If more than one variable is listed it indicates those variables are all showing change, if a single variable is indicated, it indicates only that variable is showing change.

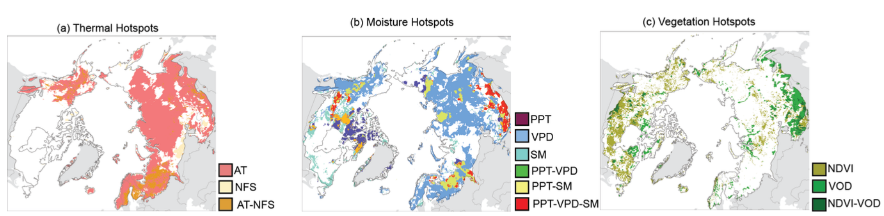

SI Figure 31. Multivariate Getis-ord Gi*-based change score maps for the summer (June – August) 1997–2020 period (unless otherwise indicated), according to select moisture and vegetation Indicators, for which a change in an identified "detrimental" direction is occurring. Moisture (b) includes annual seasonal: decreases in total PPT (m); increases in average VPD (kPa); decreases in average non-frozen season SM (cm^3 cm^{-3}). Vegetation (b) includes decreases in annual seasonal average NDVI (unitless; 1997–2020) and VOD (unitless; 1998–2017). If more than one variable is listed it indicates those variables are all changing, if a single variable is indicated, it indicates only that variable is changing.

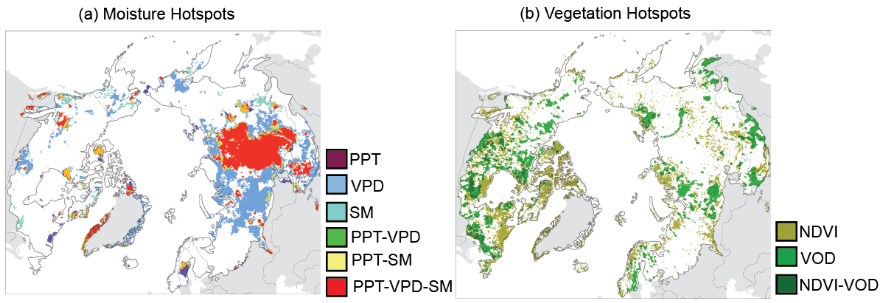

SI Figure 32 Multivariate Getis-ord Gi*-based change score maps for the autumn (September – November) 1997–2020 period (unless otherwise indicated), according to select thermal, moisture, and vegetation Indicators, for which a change in an identified "detrimental" direction is occurring. Thermal (a) includes annual seasonal: increase in average AT (°C) and total NFS (days). Moisture (b) includes annual seasonal: decrease in total PPT (m); increase in average VPD (kPa); decrease in average non-frozen season SM (cm^3 cm^{-3}). Vegetation (c) includes: decrease in annual seasonal average NDVI (unitless; 1997–2020) and average VOD (unitless; 1998–2017). If more than one variable is listed it indicates those variables are all changing, if a single variable is indicated, it indicates only that variable is changing.

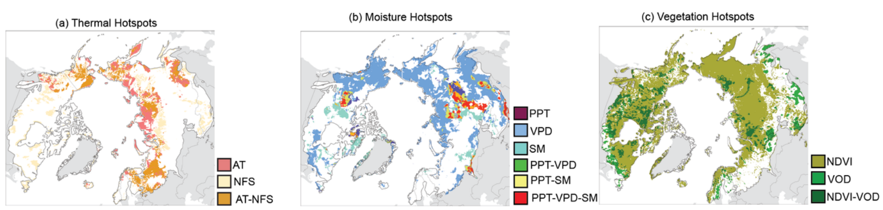

SI Figure 33. Multivariate Getis-ord Gi*-based change score maps for the winter (March – May) 1997–2020 period, according to select thermal Indicators. This includes annual seasonal: increase in average AT (°C) and total NFS (days). If more than one variable is listed it indicates those variables are all changing, if a single variable is indicated, it indicates only that variable is changing.

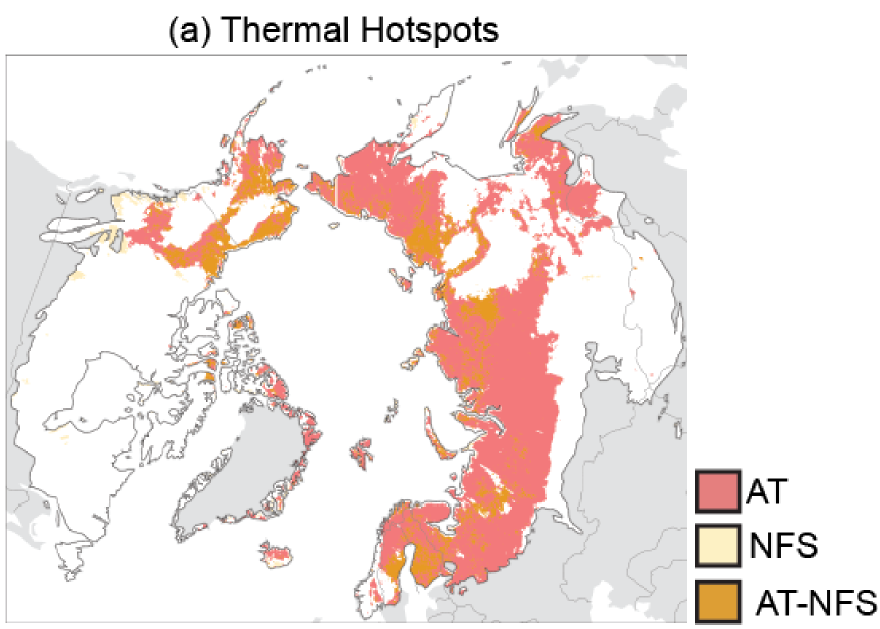

Table 1. Description of remote sensing and model-based climate products used to identify regional changes in terrestrial properties across the Arctic-boreal permafrost zone. Key indicators of ecosystem condition were included to represent thermal state, landscape moisture, vegetation and fire disturbance. *Observation frequency native to the product.

Product	Indicator Description	Spatial Resolution	Tempor
Thermal	**Thermal**	**Thermal**	**Therma**
ERA5[1]	Land Surface Air Temperature, LST (°Celsius)	0.1°	1959 – 2
SMMR;SSM/I;SSMIS[2]	Land Surface Non-frozen State, NFS (binary)	25 km	1979 – 2
ESA CCI CRDP V.2[3]	Permafrost Active Layer Thickness, ALT (m)	926 m	1997 – 2
Moisture	**Moisture**	**Moisture**	**Moistu**
ERA5[1]	Precipitation, PPT (m)	0.1°	1959 – 2
ERA5[1]	Snow Cover (%)	0.1°	1950 – 2
ERA5[1]	Vapor Pressure Deficit, VPD (kPa)	0.1°	1959 – 2
ERA5[1]	Near-surface Soil Moisture, SM (m^3 m^{-3}, 0-7 cm)	0.1°	1950 – 2
AMSR-E; AMSR2[4]	Land Surface Water Fraction (FW; %)	25 km	2003 – 2
Vegetation	**Vegetation**	**Vegetation**	**Vegetat**
GIMMs3g[5]	NDVI (unitless)	0.08°	1982 – 2
VODCA[6]	Ku-band Vegetation Optical Depth (unitless)	0.25°	1988 – 2
VCF5KYR v001 (AVHRR/MODIS)[7]	Tree & Non-Tree Cover Fraction (%)	0.05°	1982 – 2
Fire Disturbance	**Fire Disturbance**	**Fire Disturbance**	**Fire Di**
GFED4[8]	Land Surface Burned Date & Area (%)	0.25°	1995 – 2

[1] Hall et al. (2001, 2002) & Muñoz-Sabater et al. (2021).; [2] Kim et al. (2017, 2021);[3] Obu et al. (2021); [4] Du et al. (2021, 2016); [5] Pinzon et al. (2014);[6] Moesinger et al. (2020); [7] Hansen & Song (2018); [8] Randerson et al. (2018).

Table 2. Multivariate Getis-ord Gi*-based change spot scenarios for the Arctic-boreal permafrost region, according to select Indicators representing thermal, wetness, and vegetation states. All indicators were resampled to a 10 km spatial resolution for the change assessment.

Change Spot Detection Scenario	Variables	Unit	Change Direction	Spatial Resolution	Time Peri
Annual	**Annual**	**Annual**	**Annual**	**Annual**	**Annual**
Thermal	AT	°C	Increase	10 km	1997–2020
	NFS	days	Increase		1997–2020
	ALT	m	Increase		1997–2019
Wetness	PPT	m	Decrease	10 km	1997–2020
	VPD	kPa	Increase		1997–2020
	SM	cm^3 cm^{-3}	Decrease		1997–2020
Vegetation	NDVI	unitless	Decrease	10 km	1997–2017
	VOD	unitless	Decrease		1997–2017
Winter	**Winter**	**Winter**	**Winter**	**Winter**	**Winter**
Thermal	AT	°C	Increase	10 km	1997–2020
	NFS	days	Increase		1997–2020
Wetness	PPT	m	Decrease	10 km	1997–2020
	VPD	kPa	Decrease		1997–2020
Spring	**Spring**	**Spring**	**Spring**	**Spring**	**Spring**
Thermal	AT	°C	Increase	10 km	1997–2020
	NFS	days	Increase		1997–2020
	ALT	m	Increase		1997–2019

Change Spot Detection Scenario	Variables	Unit	Change Direction	Spatial Resolution	Time Peri
Wetness	PPT	m	Decrease	10 km	1997–2020
	VPD	kPa	Increase		1997–2020
	SM	cm^3 cm^{-3}	Decrease		1997–2020
Vegetation	NDVI	unitless	Decrease	10 km	1997–2017
	VOD	unitless	Decrease		1997–2017
Summer	**Summer**	**Summer**	**Summer**	**Summer**	**Summer**
Thermal	AT	°C	Increase	10 km	1997–2020
	ALT	m	Increase		1997–2019
Wetness	PPT	m	Decrease	10 km	1997–2020
	VPD	kPa	Increase		1997–2020
	SM	cm^3 cm^{-3}	Decrease		1997–2020
Vegetation	NDVI	unitless	Decrease	10 km	1997–2017
	VOD	unitless	Decrease		1997–2017
Autumn	**Autumn**	**Autumn**	**Autumn**	**Autumn**	**Autumn**
Thermal	AT	°C	Increase	10 km	1997–2020
	NFS	days	Increase		1997–2020
	ALT	m	Increase		1997–2019
Wetness	PPT	m	Decrease	10 km	1997–2020
	VPD	kPa	Increase		1997–2020
	SM	cm^3 cm^{-3}	Decrease		1997–2020
Vegetation	NDVI	unitless	Decrease	10 km	1997–2017
	VOD	unitless	Decrease		1997–2017

SI Table 3. Annual Theil-Sen (median) slope and associated p-values for Indicator variables, over three time periods: 1959–2020 (62 years); 1980–2020 (41 years); 1997–2020 (24 years) unless otherwise noted. Grey shading indicates trend significance ($\alpha = 0.05$). Trends are shown as decadal medians for the Arctic-boreal region (Full region); Eurasian (EA) tundra and/or boreal sub-regions; North America (NA) tundra and/or boreal sub-regions. [1]ALT records are through 2019. [2]FW records are 2003–2020.[3]Vegetation indicators are reported for 1988–2020 and 1998–2020 (NDVI), 1988–2017 and 1998–2017 (VOD); TC and NTC, are 1997–2016.

Ecosystem Indicators	**Ecosystem Indicators**	**Ecosystem Indicators**	Slope	P-value	Slope
Detection Category	**Dataset**	**Region**	**Years 1959–2020**	**Years 1959–2020**	**Years 1980–2020**
Thermal	AT (°C)	Full	0.38	<0.001	0.45
		EA	0.38	<0.001	0.45
		EA – Tundra	0.47	<0.001	0.61
		EA – Boreal	0.34	<0.001	0.38
		NA	0.35	<0.001	0.40
		NA – Tundra	0.40	<0.001	0.49
		NA – Boreal	0.30	<0.001	0.26
	NFS (days)	Full	-	-	1.05
		EA	-	-	1.27
		EA – Tundra	-	-	2.01
		EA – Boreal	-	-	1.54
		NA	-	-	0.23
		NA – Tundra	-	-	1.38
		NA – Boreal	-	-	0.45
	ALT (m)[1]	Full	-	-	-

Ecosystem Indicators	**Ecosystem Indicators**	**Ecosystem Indicators**	Slope	P-value	Slope
		EA	-	-	-
		EA – Tundra	-	-	-
		EA – Boreal	-	-	-
		NA	-	-	-
		NA – Tundra	-	-	-
		NA – Boreal	-	-	-

Ecosystem Indicators	**Ecosystem Indicators**	**Ecosystem Indicators**	Slope	P-value	Slope
			1959–2020	**1959–2020**	**1980–2020**
Wetness	PPT (m)	Full	0.13	<0.001	0.12
		EA	0.09	0.24	0.09
		EA – Tundra	0.19	0.01	0.31
		EA – Boreal	0.04	0.77	-0.04
		NA	0.21	<0.001	0.12
		NA – Tundra	0.19	<0.001	0.13
		NA – Boreal	0.18	<0.001	0.25
	[2]FW (%)	Full	-	-	-
		EA	-	-	-
		EA – Tundra	-	-	-
		EA – Boreal	-	-	-
		NA	-	-	-
		NA – Tundra	-	-	-
		NA – Boreal	-	-	-
	SM (cm^3 cm^{-3})	Full	0	0.24	-0.001
		EA	-0.001	0.01	-0.001
		EA – Tundra	0	0.97	0.001
		EA – Boreal	-0.001	<0.001	-0.002
		NA	0.001	0.07	0
		NA – Tundra	0.002	0.03	0
		NA – Boreal	0	0.8	0
	VPD (kPa)	Full	0.004	<0.001	0.006
		EA	0.004	<0.001	0.008
		EA – Tundra	0.002	0.01	0.004
		EA – Boreal	0.005	<0.001	0.01
		NA	0.004	<0.001	0.003
		NA – Tundra	0.002	0.03	0.001
		NA – Boreal	0.006	<0.001	0.002

Ecosystem Indicators	**Ecosystem Indicators**	**Ecosystem Indicators**	Slope	P-value	Slope	P-value	Slope	P-value
			1959–2020	**1959–2020**	**1988–2020[3]**	**1988–2020[3]**	**1997–2020[3]**	**1997–2020[3]**
Vegetation	[3]NDVI (unitless)	Full	-	-	0.00	0.46	-0.015	0.07
		EA	-	-	0.004	0.54	-0.015	0.53

Ecosystem Indicators	**Ecosystem Indicators**	**Ecosystem Indicators**	Slope	P-value	Slope	P-value	Slope	P-value
		EA – Tundra	-	-	-0.001	0.74	-0.022	0.09
		EA – Boreal	-	-	0.005	0.31	-0.09	0.79
		NA	-	-	-0.002	0.17	-0.018	0.07
		NA – Tundra	-	-	0.001	0.57	-0.012	0.17
		NA – Boreal	-	-	-0.009	<0.001	-0.025	<0.001
	[3]VOD (unitless)	Full	-	-	-0.005	0.05	0	0.67
		EA	-	-	-0.003	0.25	0.003	0.58
		EA – Tundra	-	-	-0.001	1	0.001	0.87
		EA – Boreal	-	-	-0.001	0.93	0.007	0.09
		NA	-	-	-0.005	0.24	0	0.92
		NA – Tundra	-	-	-0.008	0.30	0	0.42
		NA – Boreal	-	-	0	0.56	0.001	0.26
	[3]TC (%)	Full	-	-	0.94	<0.001	1.98	0.01
		EA	-	-	1.40	<0.001	2.67	0.02
		EA – Tundra	-	-	0.71	0.02	1.53	0.03
		EA – Boreal	-	-	1.63	<0.001	3.00	0.01
		NA	-	-	2.33	0.20	1.27	0.05
		NA – Tundra	-	-	0.49	<0.001	0.55	0.20
		NA – Boreal	-	-	0.07	0.34	1.93	0.04
	[3]NTC (%)	Full	-	-	-0.75	0.02	-1.54	0.37
		EA	-	-	-1.29	<0.001	-2.03	0.77
		EA – Tundra	-	-	-0.41	0.08	-0.91	0.69
		EA – Boreal	-	-	-1.44	<0.001	-2.38	0.09
		NA	-	-	0.20	0.92	-0.58	0.77
		NA – Tundra	-	-	0.12	0.57	0.49	0.02
		NA – Boreal	-	-	0.17	0.74	-1.32	0.28

SI Table 4. Winter (December–February) season Theil-Sen (median) slope and associated p-values. *Winter snow cover is provided in SI Table 3. Grey shading indicates trend significance (α = 0.051). Trends are shown for the Arctic-boreal (Full region); Eurasian (EA) tundra and/or boreal sub-regions; North America (NA) tundra and/or boreal sub-regions. Snow cover is scaled by 1e4 for the slopes.

Indicator	**Region**	1959–2020	1959–2020	1980–2020	1980–2020	1997–2020	1997–2020
		Slope	**P-value**	**Slope**	**P-value**	**Slope**	**P-value**
AT (°C)	Full	0.47	<0.001	0.45	<0.001	0.98	<0.001
	EA	0.47	<0.001	0.42	0.15	1.44	0.01
	EA – Tundra	0.51	<0.001	0.59	0.03	2.16	<0.001
	EA – Boreal	0.46	<0.001	0.31	0.40	1.20	0.07
	NA	0.47	<0.001	0.52	0.03	0.19	0.96
	NA – Tundra	0.43	<0.001	0.62	0.01	0.62	0.15
	NA – Boreal	0.3	<0.001	0.45	0.04	-0.05	0.56
NF (days)	Full	-	-	0.27	0.51	1.29	<0.001
	EA	-	-	0.40	0.48	1.56	0.01
	EA – Tundra	-	-	0.65	0.17	1.89	<0.001
	EA – Boreal	-	-	0.40	0.52	1.44	0.06
	NA	-	-	0.24	0.20	1.72	0.04
	NA – Tundra	-	-	0.04	0.44	0.84	0.14
	NA – Boreal	-	-	0.27	0.35	2.14	0.08
PPT (m)	Full	0.02	0.09	0.03	0.30	0.15	0.01
	EA	0.03	0.20	0.02	0.57	0.21	0.06
	EA – Tundra	0.03	0.09	0.05	0.36	0.34	<0.001
	EA – Boreal	0.03	0.33	0.03	0.65	0.10	0.25
	NA	0.02	0.32	0.04	0.33	0.06	0.09
	NA – Tundra	0.04	0.16	-0.002	0.72	-0.002	0.34
	NA – Boreal	-0.01	0.59	0.067	0.09	0.16	0.03
Snow Cover (km^2)	Full	-4.69	<0.001	-8.05	<0.001	-5.48	0.75
	EA	-4.03	0.01	-7.68	0.01	-6.52	0.60
	EA – Tundra	-0.05	<0.001	-0.08	0.05	-0.004	0.60
	EA – Boreal	-4	0.01	-7.68	0.01	-6.64	0.60
	NA	-0.35	0.03	-0.3	0.38	0.25	0.49
	NA – Tundra	-0.11	0.17	-0.14	0.54	-0.43	0.08

Indicator	Region	1959–2020	1959–2020	1980–2020	1980–2020	1997–2020	1997–2020
	NA – Boreal	-0.19	0.14	-0.16	0.45	0.77	0.07
VPD (kPa)	Full	0.001	<0.001	0.003	0.07	0.001	0.22
	EA	0.001	<0.001	0	0.09	0.002	0.03
	EA – Tundra	0.001	<0.001	0.001	0.28	0.002	0.01
	EA – Boreal	0.001	<0.001	0	0.30	0	0.96
	NA	0.001	<0.001	0.001	0.03	0.001	0.15
	NA – Tundra	0.001	<0.001	0.001	0.03	0.001	0.03
	NA – Boreal	0	<0.001	0.001	0.12	-0.001	0.19

SI Table 5. Spring (March–May) season Theil-Sen (median) slope and associated p-values. Grey shading indicates trend significance (α = 0.051). Trends are shown as decadal medians for the Arctic-boreal (Full region); Eurasian (EA) tundra and/or boreal sub-regions; North America (NA) tundra and/or boreal sub-regions. [1]FW records are 2003–2020. [2]NDVI is 1998 through 2020; VOD is 1988 through 2017. Snow cover is scaled by 1e4 for the slopes.

Indicator	Region	1959–2020	1959–2020	1980–2020[2]	1980–2020[2]	1997–2020[2]	1997–2020[2]
		Slope	**P-value**	**Slope**	**P-value**	**Slope**	**P-value**
AT (°C)	Full	0.46	<0.001	0.57	<0.001	0.72	<0.001
	EA	0.53	<0.001	0.75	<0.001	1.11	<0.001
	EA – Tundra	0.63	<0.001	0.95	<0.001	1.75	<0.001
	EA – Boreal	0.48	<0.001	0.66	<0.001	0.96	0.01
	NA	0.36	<0.001	0.30	0.06	0.51	0.46
	NA – Tundra	0.41	<0.001	0.46	0.01	0.36	0.27
	NA – Boreal	0.35	<0.001	0.10	0.35	0.46	0.75
NF (Days)	Full	-	-	1.15	<0.001	0.77	0.11
	EA	-	-	1.56	<0.001	1.15	0.03
	EA – Tundra	-	-	0.70	0.02	0.28	0.79
	EA – Boreal	-	-	2.08	<0.001	1.42	0.02
	NA	-	-	0.28	0.19	-0.02	0.71
	NA – Tundra	-	-	0.49	0.08	0.73	0.22
	NA – Boreal	-	-	0.56	0.13	-0.38	0.56
PPT (m)	Full	0.04	<0.001	0.05	0.02	0.16	0.67
	EA	0.06	0.01	0.08	0.03	0.19	0.27

Indicator	Region	1959–2020	1959–2020	1980–2020[2]	1980–2020[2]	1997–2020[2]	1997–2020[2]
	EA – Tundra	0.08	0.01	0.11	0.10	0.29	0.08
	EA – Boreal	0.064	0.03	0.07	0.09	0.15	0.32
	NA	0.02	0.10	0.01	0.97	0.19	0.15
	NA – Tundra	0.02	0.27	-0.03	0.10	0.20	0.32
	NA – Boreal	0.02	0.23	0.01	0.93	0.18	0.40
SC (km^2)	Full	-27.83	<0.001	-29.64	<0.001	-19.8	0.04
	EA	-21.59	<0.001	-28.47	<0.001	-2.56	0.02
	EA – Tundra	-1.45	<0.001	-2.29	<0.001	-2.73	0.17
	EA – Boreal	-20.47	<0.001	-26.49	<0.001	-23.77	0.03
	NA	-7.16	<0.001	-0.35	0.77	3.17	0.53
	NA – Tundra	-1.99	0.01	-1.52	0.22	-3.89	0.15
	NA – Boreal	-5.55	<0.001	-1.17	0.90	3.71	0.25
[1]FW(%)	Full	-	-	-	-	0.002	0.12
	EA	-	-	-	-	0.002	0.02
	EA – Tundra	-	-	-	-	0.003	0.10
	EA – Boreal	-	-	-	-	0.002	0.03
	NA	-	-	-	-	0.002	0.39
	NA – Tundra	-	-	-	-	0.005	0.04
	NA – Boreal	-	-	-	-	0.002	0.44
SM (cm^3 cm^{-3})	Full	0.001	0.01	0	0.28	0	0.53
	EA	0	0.33	0.001	0.26	-0.001	0.46
	EA – Tundra	0.001	<0.001	0.003	<0.001	0.004	0.01
	EA – Boreal	0	0.15	0	0.90	0.001	0.92
	NA	0.001	0.02	0	0.36	-0.001	0.92
	NA – Tundra	0.002	<0.001	0	0.72	0.	1.00
	NA – Boreal	0	0.58	-0.001	<0.001	-0.001	0.09
VPD (kPa)	Full	0.005	<0.001	0.007	<0.001	0.007	<0.001
	EA	0.006	<0.001	0.009	<0.001	0.008	<0.001
	EA – Tundra	0.002	<0.001	0.003	<0.001	0.002	0.01
	EA – Boreal	0.008	<0.001	0.011	<0.001	0.012	<0.001

Indicator	Region	1959–2020	1959–2020	1980–2020[2]	1980–2020[2]	1997–2020[2]	1997–2020[2]
	NA	0.003	<0.001	0.002	0.08	0.004	0.40
	NA – Tundra	0.002	<0.001	0.002	<0.001	0.003	0.11
	NA – Boreal	0.005	<0.001	0.003	0.17	0.005	0.53
NDVI (Unitless)	Full	-	-	0.008	<0.001	0.004	0.24
	EA	-	-	0.013	<0.001	0.008	0.20
	EA – Tundra	-	-	0.010	<0.001	0.012	0.14
	EA – Boreal	-	-	0.014	<0.001	0.007	0.14
	NA	-	-	0.00	0.65	-0.004	0.60
	NA – Tundra	-	-	0.003	0.21	0.006	0.13
	NA – Boreal	-	-	-0.006	0.03	-0.012	0.03
[2]VOD (Unitless)	Full	-	-	0.007	0.08	0.020	0.01
	EA	-	-	0.008	0.04	0.023	0.01
	EA – Tundra	-	-	0.011	0.01	0.025	0.01
	EA – Boreal	-	-	0.010	0.04	0.020	0.04
	NA	-	-	0.007	0.14	0.018	0.02
	NA – Tundra	-	-	0.004	0.36	0.021	0.02
	NA – Boreal	-	-	0.008	0.03	0.018	0.01

SI Table 6. Summer (June–August) season Theil-Sen (median) slope and associated p-values. Grey shading indicates trend significance (α = 0.051). Trends are shown as decadal medians for the Arctic-boreal (Full region); Eurasian (EA) tundra and/or boreal sub-regions; North America (NA) tundra and/or boreal sub-regions. [1]FW records are 2003–2020. [2]NDVI is 1998 through 2020; VOD is 1988 through 2017.

Indicator	Region	1959–2020	1959–2020	1980–2020[2]	1980–2020[2]	1997–2020[2]	1997–2020[2]
		Slope	**P-value**	**Slope**	**P-value**	**Slope**	**P-value**
AT (°C)	Full	0.28	<0.001	0.35	<0.001	0.42	<0.001
	EA	0.28	<0.001	0.40	<0.001	0.42	<0.001
	EA – Tundra	0.34	<0.001	0.51	<0.001	0.77	<0.001
	EA – Boreal	0.26	<0.001	0.35	<0.001	0.28	0.02
	NA	0.31	<0.001	0.31	<0.001	0.46	<0.001
	NA – Tundra	0.35	<0.001	0.36	<0.001	0.61	<0.001

Indicator	**Region**	1959–2020	1959–2020	1980–2020[2]	1980–2020[2]	1997–2020[2]	1997–2020[2]
	NA – Boreal	0.26	<0.001	0.22	0.01	0.30	0.07
PPT (m)	Full	0.04	0.02	0.01	0.92	0.01	0.60
	EA	-0.01	0.39	-0.07	0.04	-0.07	0.63
	EA – Tundra	0.04	0.29	0.01	0.93	0.03	0.75
	EA – Boreal	-0.03	0.19	-0.12	0.01	-0.07	0.96
	NA	0.10	<0.001	0.07	0.03	0.09	0.22
	NA – Tundra	0.09	<0.001	0.03	0.48	0.07	0.25
	NA – Boreal	0.10	0.01	0.12	0.03	0.14	0.17
[1]FW(%)	Full	-	-	-	-	0.002	<0.001
	EA	-	-	-	-	0.002	<0.001
	EA – Tundra	-	-	-	-	0.002	<0.001
	EA – Boreal	-	-	-	-	0.002	<0.001
	NA	-	-	-	-	0.002	0.05
	NA – Tundra	-	-	-	-	0.005	0.06
	NA – Boreal	-	-	-	-	0.001	<0.001
SM (cm^3 cm^{-3})	Full	-0.001	<0.001	-0.002	0.01	-0.004	0.03
	EA	-0.002	<0.001	-0.004	<0.001	-0.007	0.04
	EA – Tundra	-0.001	0.03	-0.002	0.23	-0.001	1.00
	EA – Boreal	-0.002	<0.001	-0.005	<0.001	-0.007	0.04
	NA	0	0.77	0	0.81	-0.002	0.32
	NA – Tundra	0	0.48	-0.001	0.42	-0.002	0.40
	NA – Boreal	-0.001	0.65	0	0.93	0	0.49
VPD (kPa)	Full	0.010	<0.001	0.015	<0.001	0.019	<0.001
	EA	0.013	<0.001	0.020	<0.001	0.027	<0.001
	EA – Tundra	0.011	<0.001	0.015	<0.001	0.025	0.01
	EA – Boreal	0.014	<0.001	0.023	<0.001	0.027	0.01
	NA	0.007	<0.001	0.007	0.04	0.009	0.22
	NA – Tundra	0.008	<0.001	0.010	<0.001	0.015	<0.001
	NA – Boreal	0.007	<0.001	0.005	0.31	0.005	0.96
[2]NDVI (Unitless)	Full	-	-	0.008	<0.001	-0.001	0.96

Indicator	Region	1959–2020	1959–2020	1980–2020[2]	1980–2020[2]	1997–2020[2]	1997–2020[2]
	EA	-	-	0.011	<0.001	0.003	0.27
	EA – Tundra	-	-	0.011	<0.001	-0.001	0.87
	EA – Boreal	-	-	0.012	<0.001	0.005	0.06
	NA	-	-	0.006	0.07	0.00	0.92
	NA – Tundra	-	-	0.008	<0.001	0.001	0.92
	NA – Boreal	-	-	0.008	<0.001	-0.001	0.96
[2]VOD (Unitless)	Full	-	-	-0.007	0.01	-0.001	1.00
	EA	-	-	-0.003	0.22	0.002	0.63
	EA – Tundra	-	-	-0.002	0.38	-0.001	1.00
	EA – Boreal	-	-	-0.001	0.78	0.007	0.10
	NA	-	-	-0.006	0.04	-0.003	0.67
	NA – Tundra	-	-	-0.010	0.12	-0.003	0.63
	NA – Boreal	-	-	-0.003	<0.001	-0.001	0.58

SI Table 7. Autumn (September–November) Theil-Sen (median) slope and associated p-values. Grey shading indicates trend significance (α = 0.051). Trends are shown as decadal medians for the Arctic-boreal (Full region); Eurasian (EA) tundra and/or boreal sub-regions; North America (NA) tundra and/or boreal sub-regions. [1]FW records are 2003–2020. [2]NDVI is 1998 through 2020; VOD is 1988 through 2017. Snow cover is scaled by 1e4 for the slopes.

Indicator	Region	1959–2020	1959–2020	1980–2020[2]	1980–2020[2]	1997–2020[2]	1997–2020[2]
		Slope	**P-value**	**Slope**	**P-value**	**Slope**	**P-value**
AT (°C)	Full	0.41	<0.001	0.57	<0.001	0.61	0.03
	EA	0.40	<0.001	0.54	<0.001	0.79	0.10
	EA – Tundra	0.59	<0.001	0.81	<0.001	1.27	0.01
	EA – Boreal	0.33	<0.001	0.38	<0.001	0.53	0.34
	NA	0.37	<0.001	0.65	<0.001	0.20	0.60
	NA – Tundra	0.45	<0.001	0.63	<0.001	0.46	0.40
	NA – Boreal	0.27	<0.001	0.50	<0.001	0.10	1.0
NF (Days)	Full	-	-	0.19	0.63	1.97	0.02
	EA	-	-	0.16	0.51	1.56	0.08
	EA – Tundra	-	-	0.52	0.17	2.61	0.06

Indicator	Region	1959–2020	1959–2020	1980–2020[2]	1980–2020[2]	1997–2020[2]	1997–2020[2]
	EA – Boreal	-	-	0.08	0.75	1.90	0.11
	NA	-	-	0.41	0.35	1.43	0.20
	NA – Tundra	-	-	0.42	0.44	2.25	0.14
	NA – Boreal	-	-	0.45	0.44	3.44	<0.001
PPT (m)	Full	0.04	0.06	0.07	0.10	0.16	0.04
	EA	0.01	0.85	0.05	0.49	0.19	0.15
	EA – Tundra	0.06	0.20	0.14	0.03	0.29	0.04
	EA – Boreal	0.004	0.87	0.07	0.90	0.15	0.19
	NA	0.09	<0.001	0.10	0.02	0.19	0.04
	NA – Tundra	0.06	<0.001	0.08	0.05	0.20	0.02
	NA – Boreal	0.10	<0.001	0.10	0.09	0.18	0.20
SC (km^2);	Full	-23.1	<0.001	-36.1	<0.001	-50.53	0.04
	EA	-17.85	<0.001	-25.5	<0.002	-40.82	0.03
	EA – Tundra	-5.42	<0.001	-7.7	0.01	-17.99	0.01
	EA – Boreal	-12.41	<0.001	-17.65	<0.002	-23.21	0.08
	NA	-6.25	0.05	-11.36	0.03	-2.95	0.96
	NA – Tundra	-4.09	<0.001	-6.29	<0.001	-2.87	0.56
	NA – Boreal	-2.68	0.35	-5.75	0.25	0.53	0.75
FW(%)	Full	-	-	-	-	0.002	0.02
	EA	-	-	-	-	0.003	<0.001
	EA – Tundra	-	-	-	-	0.004	<0.001
	EA – Boreal	-	-	-	-	0.002	<0.001
	NA	-	-	-	-	0.002	0.27
	NA – Tundra	-	-	-	-	0.003	0.39
	NA – Boreal	-	-	-	-	0.002	0.11
SM (cm^3 cm^{-3})	Full	0	0.18	-0.001	0.99	0	0.75
	EA	0	0.17	0.001	0.29	-0.001	0.63
	EA – Tundra	0.001	0.26	0.002	0.15	0.003	0.49
	EA – Boreal	-0.001	0.01	-0.001	0.05	-0.002	0.22
	NA	0.001	0.01	0	0.81	0.001	0.34

Indicator	**Region**	1959–2020	1959–2020	1980–2020[2]	1980–2020[2]	1997–2020[2]	1997–2020[2]
	NA – Tundra	0.002	0.01	0	0.88	0	0.87
	NA – Boreal	0.001	0.11	0	0.57	0	0.96
VPD (kPa)	Full	0.003	<0.001	0.007	<0.001	0.001	0.29
	EA	0.003	<0.001	0.007	<0.001	0.001	0.46
	EA – Tundra	0.002	<0.001	0.004	0.01	0.001	0.59
	EA – Boreal	0.004	<0.001	0.008	0.01	0.001	0.55
	NA	0.002	<0.001	0.008	<0.001	0.002	0.05
	NA – Tundra	0.002	<0.001	0.005	0.01	0	0.87
	NA – Boreal	0.002	0.04	0.01	<0.001	0.003	0.04
NDVI (Unitless)	Full	-	-	-0.016	<0.001	-0.037	<0.001
	EA	-	-	-0.011	<0.001	-0.038	<0.001
	EA – Tundra	-	-	-0.014	<0.001	-0.054	0.01
	EA – Boreal	-	-	-0.013	<0.001	-0.035	<0.001
	NA	-	-	-0.023	0.01	-0.037	<0.001
	NA – Tundra	-	-	-0.016	0.01	-0.029	<0.001
	NA – Boreal	-	-	-0.014	0.01	-0.046	<0.001
VOD (Unitless)	Full	-	-	-0.002	0.10	0.002	0.73
	EA	-	-	0.003	0.40	0.005	0.18
	EA – Tundra	-	-	0.005	0.09	0.006	0.03
	EA – Boreal	-	-	0.003	0.26	0.006	0.78
	NA	-	-	-0.005	0.06	-0.001	0.78
	NA – Tundra	-	-	-0.011	0.02	-0.011	0.78
	NA – Boreal	-	-	0.000	0.62	0.000	0.67

SI Table 8 Arctic-boreal ecoregion vulnerability scores, identified according to per-pixel multivariate Indicator Hotspot results (Figure 3). Scores were obtained by assigning a point (1) for each Thermal (T), Moisture (M), and Vegetation (V) Indicator hotspot.

Ecoregions with total scores of four and above are included here. The complete rankings are provided in the data package at the ORNL DAAC.

Rank	Name	Area (km²)	T	M	V	Total Score	Rank	Name
Rank	Name	Area (km²)	T	M	V	Total Score	Rank	Name
1	East Siberian Taiga	3.9E06	3	3	2	**8**	4	Northwest Siberian co
2	Cherskii-Kolyma tundra	5.6E05	3	2	2	**7**	4	Northern Pacific coast
2	Northern Cordillera forests	2.6E05	3	3	1	**7**	4	Northern transitional
2	Taimyr-Central Siberian tundra	9.6E05	3	3	1	**7**	4	Novosibirsk Islands arc
2	Trans-Baikal Bald Mt tundra	2.2E05	2	3	2	**7**	4	Pacific Coastal Mount
2	Trans-Baikal conifer forests	2.2E05	2	3	2	**7**	4	Tian Shan foothill aric
2	Mid-Continental Canadian forests	3.7E05	2	3	2	**7**	4	Northern Canadian Sh
2	Muskwa-Slave Lake forests	2.6E05	2	3	2	**7**	4	Sayan Intermontane st
2	Northwest Territories taiga	3.5E05	2	3	2	**7**	4	Selenge-Orkhon forest
3	Middle Arctic tundra	1E06	2	2	2	**6**	5	Alaska-St. Elias Range
3	Da Hinggan-Dzhagdy Mt forests	2.5E05	2	3	1	**6**	5	Alberta Mountain fore
3	Daurian forest steppe	2.1E05	2	3	1	**6**	5	Altai alpine meadow a
3	Eastern Gobi desert steppe	1.1E04	2	3	1	**6**	5	Altai steppe and semi-
3	Mongolian-Manchurian grassland	2.8E05	2	3	1	**6**	5	Arctic desert
3	Northeast Siberian taiga	1.1E06	2	3	1	**6**	5	Arctic foothills tundra
3	Okhotsk-Manchurian taiga	4E05	2	3	1	**6**	5	Beringia lowland tund
3	Sayan Alpine meadow & tundra	8.1E04	2	3	1	**6**	5	Beringia upland tundr
3	Sayan montane conifer forests	2.9E05	2	3	1	**6**	5	Brooks-British Range
3	South Siberian forest steppe	2.7E04	2	3	1	**6**	5	Cascade Mountains lee
3	West Siberian taiga	1.7E06	2	3	1	**6**	5	Chukchi Peninsula tun
4	Bering tundra	4.7E05	3	1	1	**5**	5	Cook Inset Taiga
4	Kamchatka-Kurile meadow	1.8E05	3	1	1	**5**	5	Eastern Canadian Shie
4	Kamchatka-Kurile taiga	1.5E04	3	1	1	**5**	5	Iceland boreal birch fo
4	Kamchatka Mt tundra	1.2E05	3	1	1	**5**	5	Interior Alaska-Yukon
4	Kola Peninsula tundra	5.9E04	3	1	1	**5**	5	Interior Yukon-Alaska
4	Scandinavian & Russia taiga	2.2E06	3	1	1	**5**	5	Junggar Basin Semi-de
4	Alaska Peninsula montane taiga	4.7E04	2	1	2	**5**	5	Kalaallit Nunaat high
4	Altai montane forest & steppe	1.2E05	2	2	1	**5**	5	Manchurian mixed for
4	Arctic coastal tundra	9.8E04	2	1	2	**5**	5	North Central Rockies
4	BC mainland coastal forest	4.8E04	2	2	1	**5**	5	Northern tall grasslanc
4	Central BC mountain forest	6.6E04	2	2	1	**5**	5	Northwest Russia-Nov
4	Davis Highlands tundra	8.7E04	2	2	1	**5**	5	Ogilvie-MacKenzie alp
4	Fraser Plateau and Basin	2.5E04	2	2	1	**5**	5	Okanagan dry forests
4	Gobi Lakes Valley desert steppe	5.9E04	2	2	1	**5**	5	Scandinavian Montane
4	Great Lakes Basin desert steppe	1.6E05	2	2	1	**5**	5	Southern Hudson Bay
4	High Arctic tundra	4.6E05	2	2	1	**5**	5	Tian Shan montane st
4	Kalaallit Nunaat low arctic tundra	1.7E05	2	2	1	**5**	5	Ural Montane forests a
4	Kazakh forest steppe	1.5E04	2	2	1	**5**	5	Ussuri broadleaf and n
4	Low Arctic tundra	8E05	2	1	2	**5**	5	Western Great Lakes f
4	Midwestern Canadian Shield	5.5E05	2	2	1	**5**	5	Yamal-Gydan tundra

References

Bartsch, A., Westermann, S., Strozzi, T., Wiesmann, A., Kroisleitner, C. (2020). CCI+ Permafrost D1.2. Permafrost specifications document, issue 3.0. https://climate.esa.int/media/documents/CCI_PERMA_-PSD_v3.0.pdf

Bronaugh, D., Werner, A., (2023) zyp: Zhang + Yue-Pilon Trends Package. For the Pacific Climate Impacts Consortium. R package version 0.11-1. https://CRAN.R-project.org/package=zyp.

Brown, J, O Ferrians, J A Heginbottom, E Melnikov (2002) Circum-Arctic Map of Permafrost and Ground-Ice Conditions, Version 2. Boulder, Colorado USA. NSIDC: National Snow and Ice Data Center. doi: https://doi.org.

Boschetti, L., Roy, D. P., Giglio, L., Huang, H., Zubkova, M., Humber, M. L. (2019) Global validation of the collection 6 MODIS burned area product. *Remote Sens. Environ.* , 235, 111490. https://doi.org/10.1016/j.rse.2019.111490.

Duursma, R. A. (2015) Plantecophys – An R package for analyzing and modelling leaf gas exchange data. *PLoS ONE* , 10, e0143346. https://doi.org.10.1371/journal.pone.0143346.

Du, J., Kimball, J. S. (2021). Daily Global Land Surface Parameters Derived from AMSR-E and AMSR2, Version 3. Boulder, Colorado USA. NASA National Snow and Ice Data Center Distributed Active Archive Center. doi: http://dx.doi.org/10.5067/JIKQZ6WO5C5M. [12/15/2020].

Du, J., Watts, J. D., Jiang, L., Lu, H., Cheng, X., Duguay, C., Farina, M., Qiu, Y., Kim, Y., Kimball, J.S., Tarolli, P. (2019) .Remote sensing of environmental changes in cold regions: methods, achievements, and challenges. *Remote Sens* ., 11, 1952. https://doi.org/10.3390/rs11161952.

Du, J., Kimball, J. S., Jones, L. A., Kim, Y., Glassy, J., Watts, J. D. (2017). A global satellite environmental data record derived from AMSR-E and AMSR2 microwave earth observations. Earth Sys. Sci. Data, 9, 791-808. https://doi.org/10.5194/essd-9-791-2017.

Duncan, B. N., Ott, L. E., Abshire, J. B., Brucker, L., Carroll, M. L., et al. (2019). Space-based observations for understanding changes in the Arctic-boreal zone. *Rev. Geophys* ., 58, 1-94. https://doi.org/10.1029/2019RG000652.

ECMWF (2021). IFS Documentation. Doi: 10.21957/ycow5yjr1. https://www.ecmwf.int/node/20195.

ESA. Land Cover CCI Product User Guide Version 2. Tech. Rep. (2017). Available at: maps.elie.ucl.ac.be/CCI/viewer/download/ESACCI-LC-Ph2-PUGv2_2.0.pdf

Giglio, L., Randerson, J. T., van der Werf G. R. (2013) Analysis of daily, monthly, and annual burned area using the fourth-generation global fire emissions database (GFED4). *J. Geophys. Res.* , 118, 317-328. https://doi.org/10.1002/jgrg.20042.

Hall, D., K., Riggs, G. A., Salomonson, V. V. (2001). Algorithm Theoretical Basis Document (ATBD) for the MODIS Snow and Sea Ice-Mapping Algorithms. https://modis-snow-ice.gsfc.nasa.gov/?c=atbd

Hall, D. K., Riggs, G. A., Salomonson, V. V., DiGirolamo, N. E., Bayr, K. J. (2002). MODIS snow-cover products. *Remote Sens. Environ* ., 83, 181-194. https://doi.org/10.1016/S0034-4257.

Hansen, M., Song, X. (2018). Vegetation Continuous Fields (VCF) Yearly Global 0.05 Deg [VCF5KYR.001]. NASA EOSDIS Land Processes DAAC. Accessed 2022-01-03 from https://doi.org/10.5067/MEaSUREs/VCF/VCF5KYR.001

Hansen, M., DiMiceli, C., Sohlberg, R. (2017). User Guide for the MEaSURES Vegetation Continuous Fields product, version 1. https://lpdaac.usgs.gov/documents/143/VCF5KYR_User_Guide_v1.pdf

Hersbach, H., Bell, B., Berrisford, P., Hirahara, S., Horanyi, A., et al. (2020) The ERA5 global reanalysis. *Q. J. R. Meteorol. Soc.* , 146, 1999-2049. Doi:10.1002/qj.3803. https://confluence.ecmwf.int/display/CKB/ERA5%3A+data+documentation#ERA5:datadocumentation-Introduction

Jones, L. A., Ferguson, C. R., Kimball, J. R., Zhang, K., Chan, S. K., McDonald, K. C., Njoku, E. G., Wood, E. R. (2010) Satellite microwave remote sensing of daily land surface air temperature minima and maxima from AMSR-E (2010). *IEEE JSTARS* , 3, 111-123.

Kim, Y., Kimball, J. S., Zhang, K., McDonald, K. C. (2012) Satellite detection of increasing Northern Hemisphere non-frozen seasons from 1979 to 2008: implications for regional vegetation growth. *Remote Sens. Environ* ., 121, 472-487. https://doi.org/10.1016/j.rse.2012.02.014.

Kim, Y., Kimball, J. S., Glassy, J., Du, J. (2017) An extended global Earth system data record on daily landscape freeze-thaw status determined from satellite passive microwave remote sensing. *Earth Syst. Sci. Data* , 9, 133-147. https://doi.org/10.5194/essd-9-133-2017.

Kim, Y., Kimball, J. S., Du, J., Kundig, T. (2021) A Global Data Record of Daily Landscape Freeze/Thaw Status Version 5.0. MEaSUREs Global Record of Daily Freeze/Thaw [1975 to 2020]. Boulder, Colorado, USA: National Snow and Ice Data Center. Digital media (http://dx.doi.org/10.5067/MEASURES/CRYOSPHERE/nsidc-0477.004)

Kirches G, Brockmann, M Boettcher, M Peters, S Bontemps, C Lamarche, M Schlerf, M

Santoro, P Defourny (2014) CCI-LC Product User Guide. ESA. 87 pp.

Mann, H.B. 1945. Non-parametric tests against trend, Econometrica 13:163-171.

Moesinger, L., Dorigo, W., de Jeu, R., van der Schalie, R., Scanlon, T., Teubner, I., Forkel, M. (2020). The global long-term microwave vegetation optical depth climate archive (VODCA). *Earth Syst. Sci. Data* , 12, 177-196. https://doi.org/10.5194/essd-12-177-2020.

Muñoz-Sabater, J., Dutra, E., et al. (2021). ERA5-Land: A state-of-the-art global reanalysis dataset for land applications.*Earth Syst. Sci. Data* , 13, 4349-4383.

Obu, J.,Westermann, S., Barboux, C., Bartsch, A., Delaloye, R., Grosse, G., Heim, B., Hugelius, G., Irrgang, A., Kääb, A. M., Kroisleitner, C., Matthes, H., Nitze, I., Pellet, C., Seifert, F. M., Strozzi, T., Wegmüller, U., Wieczorek, M., Wiesmann, A. (2021). ESA Permafrost Climate Change Initiative (Permafrost_cci): Permafrost active layer thickness for the Northern Hemisphere, v3.0. NERC EDS Centre for Environmental Data Analysis, 28 June 2021.

http://dx.doi.org/10.5285/67a3f8c8dc914ef99f7f08eb0d997e23

Olson, D.M., Dinerstein, E., Wikramanayake, E.D., Burgess, N.D., Powell, G.V.N., Underwood, E.C., et al. (2001) Terrestrial ecoregion of the world: a new map of life on Earth: a new global map of terrestrial ecoregions provides an innovative tool for conserving biodiversity.*BioScience* , 51: 933-938.

Pinzon, J.E., Tucker, C.J. (2014) A non-stationary 1981-2012 AVHRR NDVI3g time series. *Remote Sensing* , 6: 6929-6960.

Sexton, J. O., Feng, M., Channan, S., Song, X.-P., Kim, D.-H., et al. (2016). Earth Science Data Records of Global Forest Cover and Change. Algorithm Theoretical Basis Document. The Global Land Cover Facility, University of Maryland, MD. https://lpdaac.usgs.gov/documents/146/GFCC_ATBD.pdf

Song, X.-P., Hansen, M. C., Stehman, S. V., Potapov, P. V., Tyukavina, A., Vermote, E. F., Townshend, J. R. (2018) Global land change from 1982 to 2016. *Nature* , 560, 639-643. https://doi.org/10.1038/s41586-018-0411-9.

van Wees, D., van der Werf, G. R., Randerson, J. T., Rogers, B. M., Chen, Y., Veraverbeke, S., Giglio, L., & Morton, D. C. (2022). Global biomass burning fuel consumption and emissions at 500 m spatial resolution based on the Global Fire Emissions Database (GFED).*Geoscientific Model Development* , 15(22), 8411–8437. https://doi.org/10.5194/gmd-15-8411-2022

Walker D A, M K Raynolds, F J A Daniels, E Einarsson, et al. (2005) The Circumpolar

Arctic vegetation map. J. Veg. Sci., 16: 267-282.

Wan., Z. (2013). MODIS Land Surface Temperature Products User's Guide. NASA MODIS product. https://icess.eri.ucsb.edu/modis/LstUsrGuide/usrguide.html

Watts, J. D., Kimball, J. S., Jones, L. A., Schroeder, R., McDonald, K. C. (2012) Satellite microwave remote sensing of contrasting surface water inundation changes within the Arctic-Boreal Region. *Remote Sens. Environ.* , 127, 223-236. https://doi.org/10.1016/j.rse.2012.09.003.

Watts, J.D., Farina, M., Kimball, J.S., Schiferl, L.D., Liu, Z., Arndt, K.A., Zona, D., Ballantyne, A., et al. (2022) Carbon uptake phenology in Eurasian boreal forests dominates the high latitude carbon budget. *Global Change Biol* ., doi: 10.1111/gcb.16553

Yue, S., Pilon, P., Phinney, B., Cavadias, G. (2002) The influence of autocorrelation on the ability to detect trend in hydrological series. *Hydrol. Process* ., 16: 1807-1829.